Spectral Multiplexing on the HSX Thomson Scattering Diagnostic

By

Wayne Goodman

A dissertation submitted in partial fulfillment of

the requirements for the degree of

Doctor of Philosophy

(Electrical and Computer Engineering)

at the

University of Wisconsin-Madison

2024

Date of final oral examination: 05/03/2024

The dissertation is approved by the following members of the Final Oral Committee:
Benedikt Geiger, Assistant Professor, Nuclear Engineering and Engineering Physics
David T. Anderson, Professor Emeritus, Electrical and Computer Engineering
Mikhail A. Kats, Associate Professor, Electrical and Computer Engineering
Jennifer T. Choy, Assistant Professor, Electrical and Computer Engineering

For
Amanda,
the earth to my sky.

Abstract

Thomson scattering is a fundamental diagnostic tool in high-temperature plasma experiments, providing crucial measurements of electron temperature and density profiles. The operation of Thomson scattering diagnostics involves the propagation of an intense radiation beam through an ionized plasma, with the scattered light from free electrons within the plasma being analyzed. The spectral content of this scattered light contains information on the temperature and density of the plasma under observation. In this work, sources of error are derived and deconstructed for a Thomson scattering system, focusing on three key factors that influence measurement uncertainty: the number of primary photoelectrons generated per pulse, the uncertainty arising from the non-ideal nature of the physical detection apparatus, and the analysis routine's ability to converge on a correct solution.

Meticulous examination of these error terms has led to a significant redesign of the Thomson Scattering system at the Helically Symmetric eXperiment (HSX). This redesign, aimed at reducing noise susceptibility while increasing system bandwidth and gain, has involved electronic upgrades and the development of a new signal analysis routine. Results from testing are promising, showing that the redesigned detection electronics and analysis routine have significantly decreased measurement errors compared to the previous diagnostic setup.

This work goes beyond systematic improvements, focusing on enhancing the quality and content of measured data without increasing the required number of spectral channels, leading to the development of a novel spectral analysis technique, Thomson Scattering Spectral Multiplexing (TSSM). In a standard Thomson scattering diagnostic, scattered light is divided into wide spectral bands by a filter polychromator equipped with three to eight single bandpass filters. TSSM leverages advanced filters with multiple spectral bands to efficiently utilize Thomson scattered spectra. The results of implementing two TSSM filter sets on the HSX Thomson scattering diagnostic show a reduction in measurement uncertainty and an increased range of electron temperature measurements compared to a filter set with an equivalent number of spectral channels. As a result of this work, the Thomson scattering diagnostic on HSX is now performing at a previously thought unachievable level.

Acknowledgments

I want to express my profound appreciation to my advisor and committee chair, Professor Benedikt Geiger, for his constant support and unyielding motivation. I only had the opportunity to undertake this endeavor because my initial advisor, Professor David T. Anderson, took a chance on a nontraditional student with a checkered academic record. I'm incredibly grateful to Professor Mikhail Kats for serving on my defense committee and his discussions, which will guide my future research. Additionally, I am thankful to Professor Jennifer Choy for agreeing to serve on my defense committee at the last minute and providing invaluable suggestions for further improving my work. I also want to acknowledge the crucial role of the United States Department of Energy, whose financial support under the US DOE award DE-FG02-93ER54222 made this work possible.

Special thanks go to the entire HSX team, both past and present, for their inspiration and camaraderie. I am deeply grateful to Evan Scott for his mentorship and the hours of invaluable discussions of all things Thomson scattering. I would not have maintained my sanity during this journey if not for Juan Fernando "Fernie" Castillo, who couldn't help but bring a smile to your face and was always available for commiseration. Finally, I am deeply indebted to Alex Thornton for being a genuinely loyal friend who is always willing to share his vast knowledge and expertise.

Contents

1 Introduction **1**
1.1 Fusion Energy . . . 1
1.2 Fusion Plasma Diagnostics . . . 3
1.3 Thomson Scattering Theory . . . 3
1.4 Motivation and Outline . . . 7

2 Scattering Theory **10**
2.1 Electron Acceleration due to an Incident Electromagnetic Wave . . . 10
2.2 Radiation from an Accelerated Electron . . . 14
2.3 Single Particle Scattering . . . 20
2.4 Ensemble Scattered Power Spectra . . . 25
2.5 Analytic Formulation of Scattered Spectra . . . 26

3 Thomson Scattering Diagnostic Review **31**
3.1 Thomson Scattering Systems . . . 32
3.1.1 Radiation Source . . . 33
3.1.2 Beam Path . . . 35
3.1.3 Collection Optics . . . 36
3.2 Spectral Analysis . . . 37
3.3 Thomson Scattering on HSX . . . 40
3.3.1 The Helically Symmetric eXperiment . . . 41
3.3.2 The HSX Thomson Scattering Diagnostic . . . 42

4 Error Analysis **49**
4.1 Error Analysis . . . 49
4.2 Systematic Error Reduction . . . 53
4.2.1 Increasing $N_{S_{pe},j}$ . . . 53
4.2.2 Decreasing σ_j . . . 55
4.2.3 Increasing $\sum_j \frac{\partial N_{S_{pe},j}}{\partial T_e}$ . . . 57

5 Upgrade of the HSX Thomson Scattering Diagnostic **60**
5.1 High Speed Digitization . . . 61
5.2 Polychromator Electronics . . . 64
5.3 Signal Analysis . . . 69
5.4 Laser Power and Optical Setup Optimization . . . 71
5.5 Simplified System Model . . . 78
5.6 Improved Spectral Calibration . . . 81
5.7 Summary of System Improvements . . . 84

6 Filter Optimization and Spectral Multiplexing **89**
6.1 Optical Filter Technology . . . 89
6.2 Polychromator Filter Set Design . . . 90
6.3 Filter Optimization . . . 94
6.4 Typical Thomson Scattering Filter Sets . . . 97
6.5 Spectral Multiplexing . . . 100
6.6 HSX Spectrally Multiplexed Filter Sets . . . 105

7 Results **110**
7.1 Results of HSX Thomson Scattering Diagnostic Systematic Improvements . . . 110
7.2 TSSM Filter Set Results . . . 120

8 Conclusion **123**
8.1 Summary of Key Results . . . 124
8.2 Future Work . . . 127

A Custom TSSM Filter Data **129**

B Upgraded HSX Filter Set Data **133**

C Pre-Upgrade Error vs. Post-Upgrade Error **143**

Chapter 1

Introduction

1.1 Fusion Energy

Fusion energy has the potential to revolutionize the world's energy landscape and is a beacon of hope for a sustainable and clean future. It is the process by which atomic nuclei combine to form a heavier nucleus, releasing a vast amount of energy. This mechanism powers the sun, the source of life on Earth, demonstrating the immense potential of fusion energy.

One of the most significant advantages of fusion energy is that it is a clean and sustainable energy source. Unlike fossil fuels, which emit large amounts of greenhouse gases and contribute to global climate change, fusion energy produces no carbon emissions or other airborne pollutants. Deuterium and tritium, both isotopes of hydrogen, are the most promising fuel for operating a fusion power plant. For example, deuterium is naturally abundant and can be acquired with minimal effort or investment. Additionally, fusion reactions have a much higher released energy density than

traditional fossil fuels.

Another advantage of fusion energy is that it produces very little long-lived radioactive waste compared to nuclear fission. Nuclear fission generates radioactive waste that can take hundreds or thousands of years[1] to decay, posing a significant risk to public health and the environment. In contrast, fusion radioactive waste is short-lived and primarily consists of the materials used in the reactor, which will be mitigated through engineering controls.

Investing in fusion energy research can be a strategic move for countries, potentially driving significant economic growth. While the initial investment in research and infrastructure is substantial, the long-term benefits are equally impressive. Once operational, fusion energy can provide a reliable and cost-effective energy source for decades, giving nations at the forefront of fusion research a competitive edge in technological innovation and economic prosperity.

Finally, the development of fusion energy can also help address the issue of energy security. Countries dependent on fossil fuels for their energy needs are vulnerable to fluctuations in oil and gas prices, geopolitical tensions, and supply chain disruptions. Fusion energy can provide a stable and reliable source of energy that is not subject to these risks, enhancing energy security and reducing dependence on foreign energy sources. Now that investors recognize the need for fusion reactors for energy production, fusion start-ups are beginning to receive large sums of investment capital[2]. Although the growth in fusion-related companies will be a socio-economic boon, it is essential to focus on the fact that these reactor concepts will need high-performance, reliable diagnostics to ensure optimal operation and the general public's safety. Although many technical challenges remain associated with making fusion energy a

reality, the benefits of access to a limitless, clean energy source make a large-scale investment in fusion research and development a practical necessity.

1.2 Fusion Plasma Diagnostics

Diagnostics, as essential tools in fusion energy research, play a pivotal role in measuring and analyzing the properties of high-temperature plasmas. Advanced fusion diagnostics make the precision control and measurement systems required for sustained fusion reactions possible. Having reliable and accurate plasma diagnostics will be critical to the control and operation of a successful fusion power generation facility[3]. Measuring plasma parameters, such as temperature, density, and magnetic field strength, is critical in diagnosing the behavior of the plasma. Specifically, knowledge of the T_e and n_e profiles of a plasma discharge allows for the characterization of the quality of a given plasma discharge. These measurements provide information on the stability and confinement of the plasma, which is essential for maintaining the high temperature and pressure required for fusion reactions. Moreover, diagnostics are instrumental in designing and optimizing fusion devices, aiding researchers in enhancing the performance and efficiency of these intricate systems.

1.3 Thomson Scattering Theory

Thomson scattering has been successfully used as a primary diagnostic on many fusion plasma research experiments[4–6] for the measurement of T_e and n_e profiles. The Thomson scattering process can be described as an elastic scattering of electromagnetic radiation that occurs when a freely moving charged particle, such as an electron,

experiences accelerating from an incident photon wave. Fig. 1.1 presents a depiction of the scattering process. At timestamp (1), an electromagnetic travels through space in the direction of a free charged particle. Interaction with the electromagnetic wave at timestamp (2) excites the charged particle, leading to the re-radiation of the incident wave as a scattered wave, shown in timestamp (3). When the incident wave no longer interacts with the particle, see timestamp (4), the particle is no longer excited and ceases radiating.

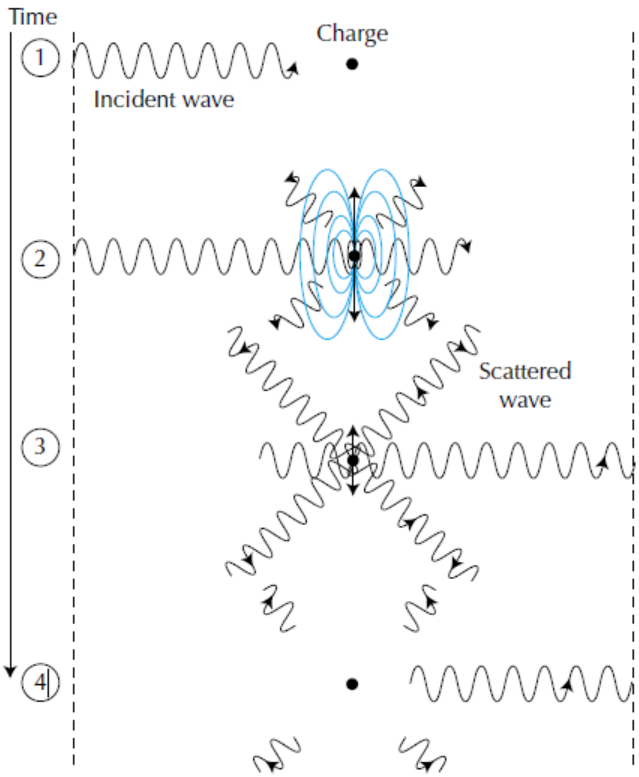

Figure 1.1: Scattering of radiation by a free charge. From *Plasma Scattering of Electromagnetic Radiation*, (2nd ed., p8), by J. Sheffield, 2010, Academic Press.

Thomson scattering is the low-energy limit of Compton scattering[7] that occurs when the incident radiation wavelength is much greater than that of the charged

particle's Compton wavelength, λ_i.

$$\lambda_i \gg \frac{h}{m_e c} \tag{1.1}$$

In Eq. (1.1), h is the Planck constant, m_e is the electron rest mass, and c is the speed of light in a vacuum. The particle's kinetic energy and the incident photon's wavelength remain unchanged in the low-energy limit of Compton scattering. Thomson scattering in a high-temperature plasma has two regimes of interest, coherent (collective) and incoherent (noncollective) scattering, determined by the incident wave wavelength and the Debye length. The Debye length, or λ_{De}, is defined as

$$\lambda_{De} = \sqrt{\frac{\epsilon_0 \kappa T_e}{e^2 n_e}}, \tag{1.2}$$

and defines the length scale at which plasma electrons interact with external electromagnetic forces. In Eq. (1.2), ϵ_0 is the permittivity of free space, κ is Boltzmann's constant, T_e is the electron temperature, e is the elementary charge, and n_e is the plasma density. In the case of noncollective scattering, the incident radiation has a wavelength much less than that of the Debye length, $\lambda_i \ll \lambda_{De}$, and can interact with individual electrons in a plasma. Since the incident radiation can only interact with individual electrons, the scattered radiation only contains information on the bulk plasma electrons. Conversely, collective scattering occurs when $\lambda_i > \lambda_{De}$ and instead of interacting with individual electrons, the incident radiation interacts with electron clouds that shield ions with a radius of λ_{De}. In this case, scattered radiation contains information about electrons and ions within a plasma. The Thomson scattering system currently used on HSX operates in the non-collective scattering regime,

so further references to Thomson scattering will specifically refer to non-collective Thomson scattering.

Although, as previously stated, Thomson scattered radiation is emitted at the same wavelength as the incident radiation, measurements of the scattered spectra demonstrate both spectral broadening and blue shifting. These two phenomena are the direct result of the energy content of the plasma electrons. First, when "warm" electrons with $T_e > 1\ eV$, equivalent to 11,600 K, interact with an incident photon wave, the resulting scattered radiation exhibits spectral broadening. Due to the electron's velocity relative to the incident radiation, the incident radiation experiences a Doppler shift in frequency in the electron frame of reference, which presents as the aforementioned spectral broadening. As electrons gain even more thermal energy and become increasingly relativistic, there is a significant amount of blue-shifting in the scattered radiation spectra. The relativistic headlight effect causes blue-shifting of the scattered radiation. In the relativistic headlight effect, in the rest frame of an outside observer, a relativistic object preferentially emits radiation in its direction of travel, see Fig. 2.2 and Fig. 2.3 in Section 2.2. Therefore, the broadening and blue-shifting of the scattered spectra are directly proportional to the electron's velocity and the electron's thermal energy, T_e. While analysis of the scattered light spectrum allows the determination of T_e, n_e is directly proportional to the absolute magnitude of scattered radiation, which can be directly measured and allows for the determination of n_e.

1.4 Motivation and Outline

This work aims to improve the existing Thomson scattering diagnostic on HSX through engineering-level system modifications and applying a novel filter design and analysis technique. In pursuit of this goal, Chapter 2 gives a thorough description of Thomson scattering theory and uses this background to derive the reaction of a single charged particle to an incident electromagnetic wave. After this initial derivation, the same treatment is extended to an ensemble of charged particles to derive the scattered power spectrum emitted from a collection of plasma electrons when probed by an electromagnetic wave. Finally, Chapter 2 closes by introducing a simplified and accurate analytical model for quick calculations of scattered spectral information.

Chapter 3 begins with a discussion of components commonly in place on a Thomson scattering diagnostic, including the introduction and motivation for using polychromators. Chapter 3 ends with a discussion of the Helically Symmetric eXperiment (HSX) and its Thomson scattering diagnostic. After introducing the spectral analysis methodology used in Thomson scattering, an error analysis is performed in Chapter 4 to understand how error propagates within Thomson measurements, followed by a discussion of strategies to reduce overall system error. In Chapter 5, systematic improvements to the existing HSX Thomson scattering diagnostic are introduced and their resulting improvements are discussed.

Motivated by the error analysis of the previous chapter, Chapter 6 begins with a discussion of modern filter technology and pivots to filter set design and optimization. Chapter 6 then culminates with an introduction to the newly developed Thomson scattering spectroscopic method, referred to as Thomson Scattering Spectral Multiplexing, or simply TSSM. In Chapter 7, results of the work described in Chapters 5

and 6 are presented and discussed. Finally, Chapter 8 summarizes the total impact of this work and suggests future work that will further enhance the HSX Thomson scattering diagnostic.

Bibliography

[1]E. Farfan, "Long-term dynamics of radionuclide vertical migration in soils of the chernobyl nuclear power plant exclusion zone", Environ. Sci. Technol., Institution: Savannah River Site (SRS), Aiken, SC (United States) Number: SRNL-STI-2009-00770 (2009).

[2]Fusion Energy Association, *Global fusion industry report*, Annual Survey 2022 (Jan. 12, 2022).

[3]W. Biel et al., "Diagnostics for plasma control – from ITER to DEMO", Fusion Engineering and Design, SI:SOFT-30 **146**, 465–472 (2019).

[4]H.-J. Hartfuß and T. Geist, *Fusion plasma diagnostics with mm-waves: an introduction*, Physics textbook (Wiley-VCH-Verl, Weinheim, 2013), 408 pp.

[5]J. Sheffield, ed., *Plasma scattering of electromagnetic radiation: experiment, theory and computation*, 1st ed (Elsevier, Amsterdam ; Boston, 2011), 497 pp.

[6]I. H. Hutchinson, *Principles of plasma diagnostics*, Repr (Cambridge University Press, Cambridge, 1994), 364 pp.

[7]D. J. Griffiths, *Introduction to electrodynamics*, Fourth edition (Cambridge University Press, Cambridge, United Kingdom ; New York, NY, 2018).

Chapter 2

Scattering Theory

2.1 Electron Acceleration due to an Incident Electromagnetic Wave

Before beginning the scattered radiation derivations, it will be beneficial to introduce the scattering geometry used during the rest of this document; see Fig. 2.1. Following convention, [6, 8, 9], the incident beam is assumed to be linearly polarized and perpendicular to the scattering plane formed by $\hat{i}$ and $\hat{s}$, the propagation and scattered direction, respectively. This constraint on the polarization of the incident wave is generally met experimentally so that the analysis will be accurate for the most significant configurations. Not pictured in Fig. 2.1, but another critical assumption used in the upcoming analysis, is that it is assumed that the scattered radiation is also linearly polarized such that the electric field component on the scattered wave, $\vec{\boldsymbol{E}}_{\boldsymbol{s}}$, is parallel to $\vec{\boldsymbol{E}}_i$. In practice, the scattered wave polarization constraint can be enforced either by the use a polarizer in the collection optics or by careful alignment

of the probing beam with the plasma vessel entrance and exit windows.

Since an accelerating charged particle will emit electromagnetic radiation[7, 10, 11], we must start by deriving the acceleration of an electron exposed to electromagnetic radiation. First, we start with Newton's second law of motion,

$$\vec{\boldsymbol{F}} = m\vec{\boldsymbol{a}} = \frac{d\vec{\boldsymbol{v}}}{dt} \tag{2.1}$$

and replace $\vec{\boldsymbol{F}}$, the force on the electron due to an incident beam of light, with the Lorentz force

$$\vec{\boldsymbol{F}} = q\left(\vec{\boldsymbol{E}}_i + \vec{\boldsymbol{v}} \times \vec{\boldsymbol{B}}_i\right) \tag{2.2}$$

where q is the charge of the particle, $\vec{\boldsymbol{v}}$ is the particle velocity, $\vec{\boldsymbol{E}}_i$ is the electric field

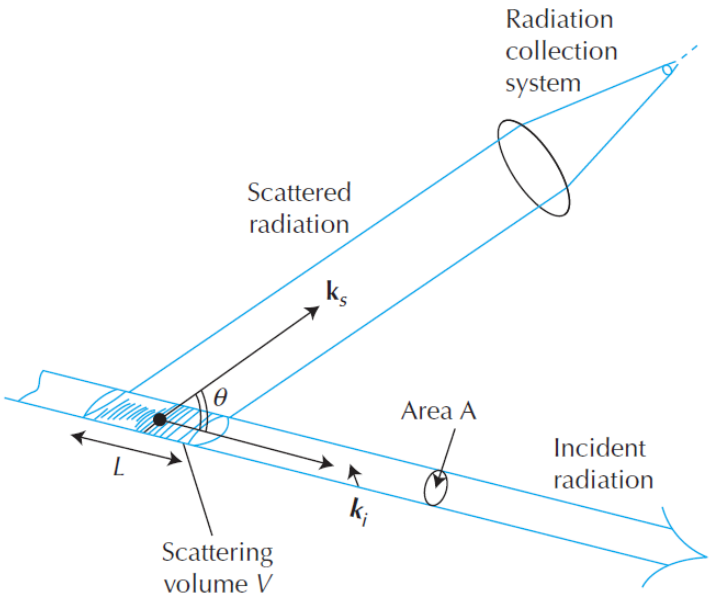

Figure 2.1: Scattering geometry used in this work. The incident wave electric field, $\vec{\boldsymbol{E}}_i$, is polarized perpendicular to the scattering plane formed by the propagation vector, $\boldsymbol{k_i}$, and the scattering vector, $\boldsymbol{k_s}$. From *Plasma Scattering of Electromagnetic Radiation*, (2nd ed., p34), by J. Sheffield, 2010, Academic Press.

component of the incident radiation, and $\vec{\boldsymbol{B}}_i$ is the magnetic field component of the incident radiation. For fusion-relevant plasmas[12, 13], electrons are expected to move at an appreciable fraction of the speed of light; therefore, electrons should receive relativistic treatment. To treat the electrons relativistically, the mass correction

$$m_{rel} = \frac{m}{\sqrt{1 - \dfrac{v^2}{c^2}}} \tag{2.3}$$

is substituted into Eq. (2.1) to get our desired equation of motion

$$\frac{d}{dt}\left\{\frac{m_e\vec{\boldsymbol{v}}}{\sqrt{1 - \dfrac{v^2}{c^2}}}\right\} = -e\left(\vec{\boldsymbol{E}}_i + \vec{\boldsymbol{v}} \times \vec{\boldsymbol{B}}_i\right) \tag{2.4}$$

where m_e is the electron rest mass and $-e$ is the charge of the electron.

In order to simplify Eq. (2.4), we introduce β as the ratio of v to c to rewrite Eq. (2.4) as

$$m_e\frac{d}{dt}\left\{\frac{\vec{\boldsymbol{\beta}}}{\sqrt{1 - \vec{\boldsymbol{\beta}}^2}}\right\} = -e\left(\frac{\vec{\boldsymbol{E}}_i}{c} + \vec{\boldsymbol{\beta}} \times \vec{\boldsymbol{B}}_i\right) \tag{2.5}$$

and perform the differentiation to get

$$m_e\gamma\dot{\vec{\boldsymbol{\beta}}} + m_e\gamma^3\vec{\boldsymbol{\beta}}\left(\vec{\boldsymbol{\beta}} \cdot \dot{\vec{\boldsymbol{\beta}}}\right) = -e\left(\frac{\vec{\boldsymbol{E}}_i}{c} + \vec{\boldsymbol{\beta}} \times \vec{\boldsymbol{B}}_i\right) \tag{2.6}$$

where $\dot{\vec{\boldsymbol{\beta}}} = \dfrac{d\vec{\boldsymbol{\beta}}}{dt}$ and γ is the Lorentz factor[14], defined in Eq. (2.7).

$$\gamma \equiv \frac{1}{\sqrt{1 - \dfrac{v^2}{c^2}}} = \frac{1}{\sqrt{1 - \beta^2}} \tag{2.7}$$

Next, we perform a dot product of Eq. (2.6), giving

$$m_e \gamma \dot{\vec{\boldsymbol{\beta}}} \cdot \vec{\boldsymbol{\beta}} + m_e \gamma^3 \vec{\boldsymbol{\beta}} \left(\vec{\boldsymbol{\beta}} \cdot \dot{\vec{\boldsymbol{\beta}}} \right) \cdot \vec{\boldsymbol{\beta}} = -e \left(\frac{\vec{\boldsymbol{E}}_i}{c} + \vec{\boldsymbol{\beta}} \times \vec{\boldsymbol{B}}_i \right) \cdot \vec{\boldsymbol{\beta}} \tag{2.8}$$

Simplifying and rearranging Eq. (2.8) gives us the form

$$\dot{\vec{\boldsymbol{\beta}}} \cdot \vec{\boldsymbol{\beta}} = -\frac{e}{m_e \gamma^3 c} \vec{\boldsymbol{\beta}} \cdot \vec{\boldsymbol{E}}_i \tag{2.9}$$

which can be substituted back into Eq. (2.6) to get

$$m_e \gamma \dot{\vec{\boldsymbol{\beta}}} + m_e \gamma^3 \vec{\boldsymbol{\beta}} \left(-\frac{e}{m_e \gamma^3 c} \vec{\boldsymbol{\beta}} \cdot \vec{\boldsymbol{E}}_i \right) = -e \left(\frac{\vec{\boldsymbol{E}}_i}{c} + \vec{\boldsymbol{\beta}} \times \vec{\boldsymbol{B}}_i \right) \tag{2.10}$$

which can be simplified to give the electron acceleration due to an incident electromagnetic field as

$$\dot{\vec{\boldsymbol{\beta}}} = -\frac{e}{m_e \gamma} \left\{ \frac{\vec{\boldsymbol{E}}_i}{c} - \left(\frac{\vec{\boldsymbol{\beta}} \cdot \vec{\boldsymbol{E}}_i}{c} \right) \vec{\boldsymbol{\beta}} + \vec{\boldsymbol{\beta}} \times \vec{\boldsymbol{B}}_i \right\}. \tag{2.11}$$

Now that we have the acceleration due to an incident electromagnetic field, it would be convenient to write the entire equation simply in terms of the incident wave electric field component, $\vec{\boldsymbol{E}}_i$. Assuming plane-wave propagation in the direction $\hat{i}$, we

can rewrite $\vec{\boldsymbol{B}}_i$ in terms of $\vec{\boldsymbol{E}}_i$ using the relation[11]

$$\vec{\boldsymbol{B}}_i = \frac{1}{c}\hat{i} \times \vec{\boldsymbol{E}}_i \tag{2.12}$$

and substituting Eq. (2.12) into Eq. (2.11) to get

$$\dot{\vec{\boldsymbol{\beta}}} = -\frac{e}{m_e c\gamma}\left\{\vec{\boldsymbol{E}}_i - \left(\vec{\boldsymbol{\beta}} \cdot \vec{\boldsymbol{E}}_i\right)\vec{\boldsymbol{\beta}} + \hat{i}\left(\vec{\boldsymbol{\beta}} \cdot \vec{\boldsymbol{E}}_i\right) - \vec{\boldsymbol{E}}_i\left(\vec{\boldsymbol{\beta}} \cdot \hat{i}\right)\right\}, \tag{2.13}$$

the final form of the electron acceleration equation, we need to derive the relativistic Thomson spectrum.

Before continuing, a few important features of Eq. (2.13) should be discussed. First, from investigating Eq. (2.13), it can be shown that if $\vec{\boldsymbol{E}}_i = 0$, the acceleration $\dot{\vec{\boldsymbol{\beta}}}$ must also be 0, showing that without the electric field component of the light wave, there would be no acceleration and, therefore, no radiation will be emitted by the free electron, which makes sense in the Thomson scattering framework. Another important feature of Eq. (2.13) is that the final three terms of $\dot{\vec{\boldsymbol{\beta}}}$ are all a factor of $\vec{\boldsymbol{\beta}}$. This means that in the non-relativistic limit, $v \ll c$, all three terms of $\vec{\boldsymbol{\beta}}$ go to zero and the acceleration is simply

$$\dot{\vec{\boldsymbol{\beta}}} = -\frac{e}{m_e c}\vec{\boldsymbol{E}}_i, \tag{2.14}$$

which is accurate for plasmas with electron temperatures on the order of a few keV.

2.2 Radiation from an Accelerated Electron

Now that we have derived the equation for $\vec{\boldsymbol{\beta}}$, the acceleration of an electron, we must derive the radiation field emitted from the accelerated electron. We start with

Maxwell's equations and combine them to obtain[10, 15]

$$\nabla \times \left(\nabla \times \vec{\boldsymbol{E}}\right) + \mu_0 \epsilon_0 \frac{\partial^2 \vec{\boldsymbol{E}}}{\partial t^2} = -\mu_0 \frac{\partial \vec{\boldsymbol{J}}}{\partial t} \tag{2.15}$$

Using the current density from a point charge

$$\vec{\boldsymbol{J}} = q\vec{\boldsymbol{v}}(t') \tag{2.16}$$

and taking into account that the electric field at the observer, distance R, is due to the field at a prior time

$$t' = t - (R'/c) \tag{2.17}$$

we get the solution to Eq. (2.15)

$$\vec{\boldsymbol{E}}(\vec{\boldsymbol{R}}', t') = \frac{q}{4\pi\epsilon_0}\left[\frac{\left(\hat{s} - \vec{\boldsymbol{\beta}}\right)\left(1 - \vec{\boldsymbol{\beta}}^2\right)}{\left(1 - \hat{s}\cdot\vec{\boldsymbol{\beta}}\right)^3 R'^2}\right]_{ret} + \frac{q}{4\pi\epsilon_0 c}\left[\frac{\hat{s}\times\left\{\left(\hat{s} - \vec{\boldsymbol{\beta}}\right)\times\dot{\vec{\boldsymbol{\beta}}}\right\}}{\left(1 - \hat{s}\cdot\vec{\boldsymbol{\beta}}\right)^3 R'}\right]_{ret} \tag{2.18}$$

where the fields are evaluated at the retarded time where

$$\dot{\vec{\boldsymbol{\beta}}} = \frac{1}{c}\frac{d\vec{\boldsymbol{v}}}{dt'}. \tag{2.19}$$

Under normal experimental conditions, the observer of the scattering event is much farther than the characteristic length of the scattering event, $R' \gg L$, therefore

the first term of Eq. (2.18) can be dropped so that we will write Eq. (2.18) as simply

$$\vec{\boldsymbol{E}}_s(\vec{\boldsymbol{R}}', t') = -\frac{e}{4\pi\epsilon_0 c}\left[\frac{\hat{s}\times\left\{\left(\hat{s}-\vec{\boldsymbol{\beta}}\right)\times\dot{\vec{\boldsymbol{\beta}}}\right\}}{\left(1-\hat{s}\cdot\vec{\boldsymbol{\beta}}\right)^3 R'}\right] \tag{2.20}$$

The scattered power per unit solid angle is[5]

$$\frac{dP_s}{d\Omega} = R^2\vec{\boldsymbol{S}}\cdot\hat{s} \tag{2.21}$$

where $\vec{\boldsymbol{S}}$ is the Poynting vector, defined as

$$\vec{\boldsymbol{S}} \equiv \vec{\boldsymbol{E}}_s \times \frac{\vec{\boldsymbol{B}}_{\boldsymbol{s}}}{\mu_0} = \vec{\boldsymbol{E}}_s \times \frac{1}{\mu_0 c}\hat{s}\times\vec{\boldsymbol{E}}_s = \epsilon_0 c E_s^2 \hat{s}. \tag{2.22}$$

Taking the definition of the Poynting vector from Eq. (2.22) and substituting it into Eq. (2.21), we obtain

$$\frac{dP_s}{d\Omega} = \epsilon_0 c R^2 E_s^2 \left(1-\beta\cos\theta_2\right) \tag{2.23}$$

where the additional factor of $(1-\beta\cos\theta_2)$ is added to account for the retarded time effects described by

$$dt = \left(1-\beta\cos\theta_2\right)dt' \tag{2.24}$$

which leads to

$$\frac{dP_s}{d\Omega} = \frac{e^2}{16\pi^2 c\epsilon_0}\frac{1}{\left(1-\beta\cos\theta_2\right)^5}\left|\hat{s}\times\left\{\left(\hat{s}-\vec{\boldsymbol{\beta}}\right)\times\dot{\vec{\boldsymbol{\beta}}}\right\}\right|^2. \tag{2.25}$$

Using the vector relation[16]

$$\vec{\boldsymbol{A}} \times \left(\vec{\boldsymbol{B}} \times \vec{\boldsymbol{C}}\right) = \vec{\boldsymbol{B}}\left(\vec{\boldsymbol{A}} \cdot \vec{\boldsymbol{C}}\right) - \vec{\boldsymbol{C}}\left(\vec{\boldsymbol{A}} \cdot \vec{\boldsymbol{B}}\right) \tag{2.26}$$

to expand the squared factor in Eq. (2.25), we can then rewrite the scattered power per unit solid angle as

$$\frac{dP_s}{d\Omega} = \frac{e^2}{16\pi^2 c\epsilon_0}\left\{\frac{\dot{\beta}^2}{\left(1-\beta\cos\theta_2\right)^3} + \frac{2\dot{\beta}_s\left(\vec{\dot{\boldsymbol{\beta}}}\cdot\vec{\boldsymbol{\beta}}\right)}{\left(1-\beta\cos\theta_2\right)^4} - \frac{\dot{\beta}_s^2\left(1-\beta^2\right)}{\left(1-\beta\cos\theta_2\right)^5}\right\}. \tag{2.27}$$

With the general equation for scattered power now derived, we can begin to predict the scattered radiation patterns for a couple of interesting configurations. First, let us consider the scattered power radiated if the electron acceleration, $\vec{\dot{\boldsymbol{\beta}}}$ is parallel to the velocity of the charged particle, $\vec{\boldsymbol{\beta}}$. For this analysis, assume the following scattering geometry described by

$$\vec{\boldsymbol{\beta}} = \beta\hat{z}$$

$$\vec{\dot{\boldsymbol{\beta}}} = \dot{\beta}\hat{z}$$

$$\hat{s} = \left(\sin\theta_2\cos\phi\right)\hat{x} + \left(\sin\theta_2\sin\phi\right)\hat{y} + \left(\cos\theta_2\right)\hat{z}$$

$$\dot{\beta}_s = \vec{\dot{\boldsymbol{\beta}}}\cdot\hat{s}.$$

Substituting the defined geometry values into Eq. (2.27), we can now write the scattered power per unit solid angle in this geometry as

$$\frac{dP_s}{d\Omega} = \frac{e^2\dot{\beta}^2}{16\pi^2 c\epsilon_0}\frac{\sin^2\theta_2}{\left(1-\beta\cos\theta_2\right)^5}. \tag{2.28}$$

In Fig. 2.2, the radiation pattern of the angular dependent term of Eq. (2.28) for

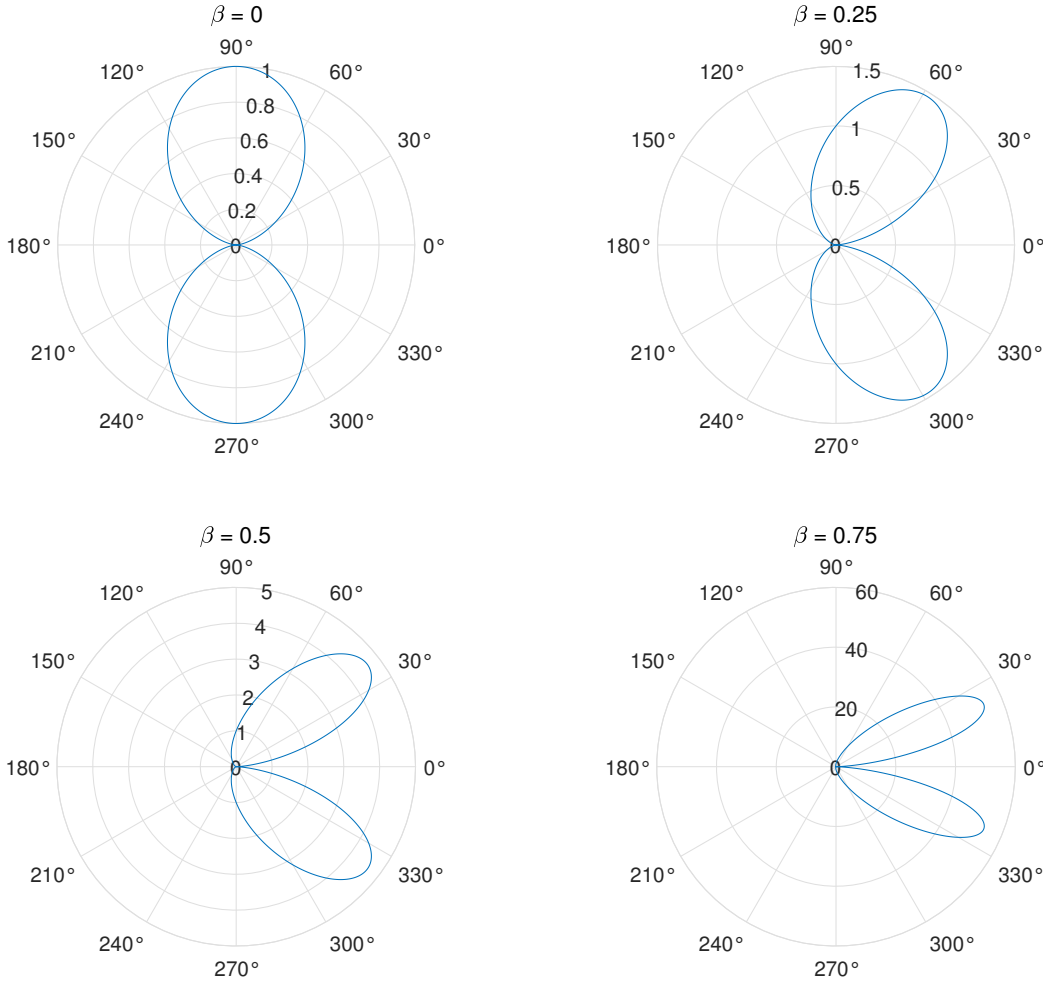

Figure 2.2: Polar plots of the scattered power radiation patterns for values of $\beta = 0$, 0.25, 0.5, and 0.75, when acceleration is parallel to the direction of particle velocity. As the scattering particle velocity becomes increasingly relativistic, the radiation pattern is clearly biased in the direction of movement.

various values of β, representing scattering from particles that are traveling at increasingly relativistic velocities, is plotted. It is important to note that as β approaches 1, the radiation patterns are increasingly biased in the direction of movement. This bias is due to the relativistic headlight effect, where particles tend to emit radiation more

strongly in the direction of travel as they approach the speed of light. The headlight effect can be understood by considering that the particle must radiate isotropically in its reference frame. For an observer, it appears to be biased in the direction of particle motion. The same procedure for calculating the emitted radiation pattern

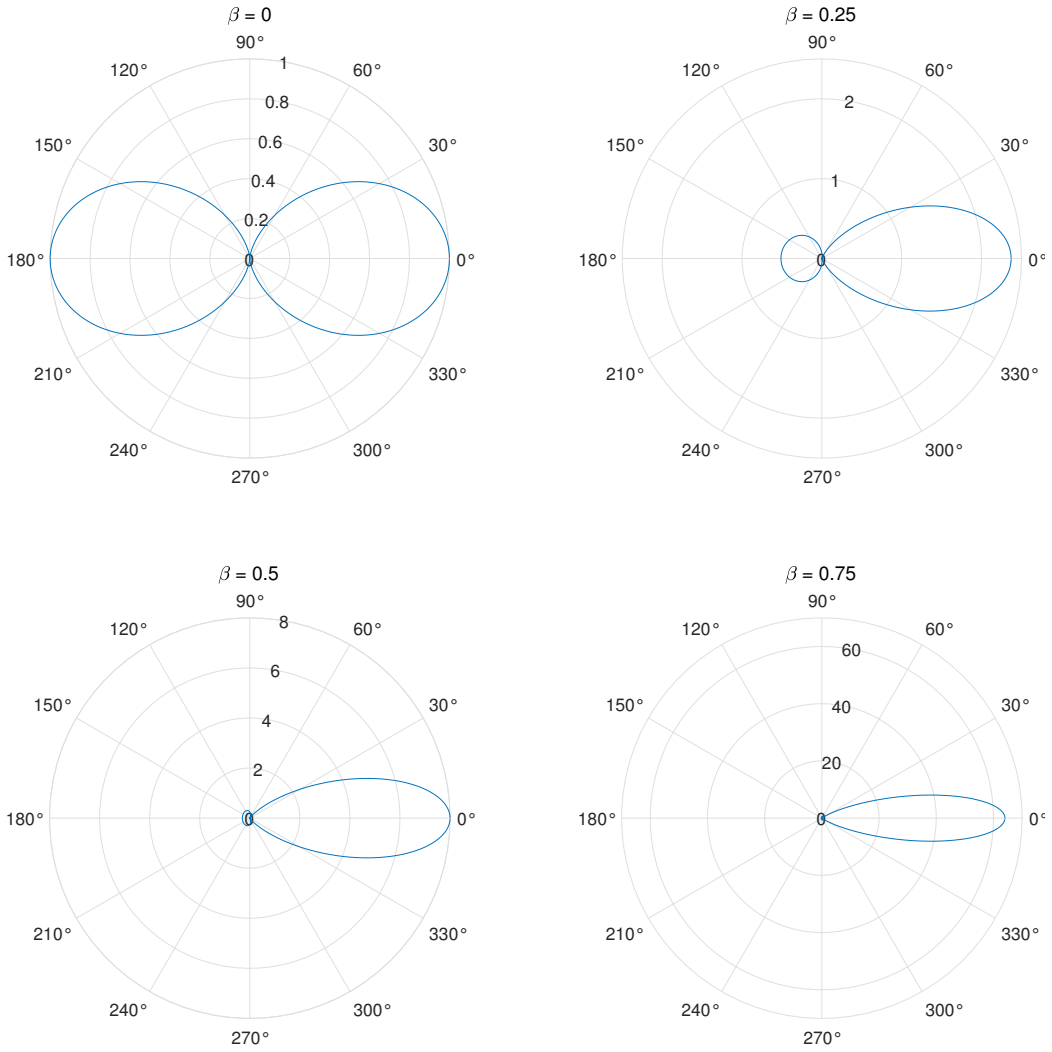

Figure 2.3: Polar plots of the scattered power radiation patterns for values of $\beta = 0$, 0.25, 0.5, and 0.75, for the case of acceleration perpendicular to the direction of particle velocity. As the scattering particle velocity becomes increasingly relativistic, the radiation pattern is clearly biased in the direction of movement.

is now carried out for a situation in which $\vec{\dot{\boldsymbol{\beta}}}$ is perpendicular to the velocity of the charged particle, $\vec{\boldsymbol{\beta}}$, and is plotted in Fig. 2.3. Similarly, the radiation pattern is still biased in the direction of particle motion, reinforcing the headlight effect explanation.

2.3 Single Particle Scattering

Now that we have derived the acceleration of an electron due to an incident light wave and the scattered power per unit solid angle of an accelerated electron, we can derive the scattered power per unit solid angle per unit wavelength shift from a single electron. However, before beginning, it is essential to recall the ideal scattering geometry defined by $\vec{\boldsymbol{E}}_i \parallel \hat{\imath} \times \hat{s}$ and $\vec{\boldsymbol{E}}_i \parallel \vec{\boldsymbol{E}}_s$.

To begin, we recall that the equation for the acceleration of an electron due to an incident light wave is

$$\vec{\dot{\boldsymbol{\beta}}} = -\frac{e}{m_e c \gamma}\left\{\vec{\boldsymbol{E}}_i - \left(\vec{\boldsymbol{\beta}} \cdot \vec{\boldsymbol{E}}_i\right)\vec{\boldsymbol{\beta}} + \hat{\imath}\left(\vec{\boldsymbol{\beta}} \cdot \vec{\boldsymbol{E}}_i\right) - \vec{\boldsymbol{E}}_i\left(\vec{\boldsymbol{\beta}} \cdot \hat{\imath}\right)\right\}, \tag{2.29}$$

and that the equation for the scattered electric field of an accelerated electron can be written as

$$\vec{\boldsymbol{E}}_s(\vec{\boldsymbol{R}}', t') = -\frac{e}{4\pi\epsilon_0 c}\left[\frac{\hat{s} \times \left\{\left(\hat{s} - \vec{\boldsymbol{\beta}}\right) \times \vec{\dot{\boldsymbol{\beta}}}\right\}}{\left(1 - \hat{s} \cdot \vec{\boldsymbol{\beta}}\right)^3 R'}\right]. \tag{2.30}$$

In order to derive the scattered power spectrum for a single particle, we will need to substitute Eq. (2.29) into Eq. (2.30). In order to simplify this process and garner a better understanding of the physical properties of Thomson Scattering, we will separate Eq. (2.29) into its three constituent terms and simplify $\hat{s} \times \left\{\left(\hat{s} - \vec{\boldsymbol{\beta}}\right) \times \vec{\dot{\boldsymbol{\beta}}}\right\}$ individually.

The Classical Term: $\vec{\dot{\boldsymbol{\beta}}} = -\frac{e}{m_e c\gamma}\vec{\boldsymbol{E}}_i$

If the velocity of the particle described by Eq. (2.29) is much less than the speed of light, then all terms that depend on β can be ignored; therefore, we can simplify the following

$$\begin{aligned}
&\hat{s} \times \left\{ \left(\hat{s} - \vec{\boldsymbol{\beta}} \right) \times \vec{\dot{\boldsymbol{\beta}}} \right\} \\
&= \hat{s} \times \left\{ \left(\hat{s} - \vec{\boldsymbol{\beta}} \right) \times (-\frac{e}{m_e c\gamma})\vec{\boldsymbol{E}}_i \right\} \\
&= \hat{s} \times \left(\vec{\boldsymbol{\beta}} \times (\frac{e}{m_e c\gamma})\vec{\boldsymbol{E}}_i \right) - \hat{s} \times \left(\hat{s} \times (\frac{e}{m_e c\gamma})\vec{\boldsymbol{E}}_i \right).
\end{aligned}$$

Again, using the vector identity from Eq. (2.26), we can rewrite the classical term as

$$(\frac{e}{m_e c\gamma})\vec{\boldsymbol{E}}_i\,(\hat{s}\cdot\hat{s}) + \vec{\boldsymbol{\beta}}\left(\hat{s} \cdot (\frac{e}{m_e c\gamma})\vec{\boldsymbol{E}}_i \right) - (\frac{e}{m_e c\gamma})\vec{\boldsymbol{E}}_i \left(\hat{s} \cdot \vec{\boldsymbol{\beta}} \right) - \hat{s}\left(\hat{s} \cdot (\frac{e}{m_e c\gamma})\vec{\boldsymbol{E}}_i \right). \quad (2.31)$$

Applying the ideal scattering geometry criteria discussed previously, we see that $\vec{\boldsymbol{E}}_i \cdot \hat{s} = 0$, therefore the final form of the classical term is

$$\hat{e} \cdot \left[\hat{s} \times \left\{ \left(\hat{s} - \vec{\boldsymbol{\beta}} \right) \times \vec{\dot{\boldsymbol{\beta}}} \right\} \right] = (\frac{e}{m_e c\gamma}) E_i\,(1 - \beta_s) \quad (2.32)$$

where we have rewritten $\vec{\boldsymbol{E}}_i$ as $E_i\hat{e}$. Referring to Eq. (2.32), we can conclude that the classical contribution to the scattered electric field is polarized in the $\hat{e}$ direction.

The Relativistic Term: $\vec{\dot{\boldsymbol{\beta}}} = -\left(\vec{\boldsymbol{\beta}} \cdot \vec{\boldsymbol{E}}_i \right) \vec{\boldsymbol{\beta}}$

Here, the relativistic term is a second-order function of β; thereby, it is firmly dependent on the velocity of the accelerated electron. The relativistic term is simplified

similarly to the classical term.

$$
\begin{aligned}
&\hat{s} \times \left\{ \left(\hat{s} - \vec{\boldsymbol{\beta}} \right) \times \dot{\vec{\boldsymbol{\beta}}} \right\} \\
&= \hat{s} \times \left\{ \left(\hat{s} - \vec{\boldsymbol{\beta}} \right) \times \left(\vec{\boldsymbol{\beta}} \cdot (\frac{e}{m_e c \gamma}) \vec{\boldsymbol{E}}_i \right) \vec{\boldsymbol{\beta}} \right\} \\
&= \hat{s} \times \left\{ \left(\hat{s} - \vec{\boldsymbol{\beta}} \right) \times \beta_e (\frac{e}{m_e c \gamma}) E_i \vec{\boldsymbol{\beta}} \right\} \\
&= \beta_e (\frac{e}{m_e c \gamma}) E_i \left\{ \hat{s} \times \left(\hat{s} - \vec{\boldsymbol{\beta}} \right) \times \vec{\boldsymbol{\beta}} \right\} \\
&= \beta_e (\frac{e}{m_e c \gamma}) E_i \left\{ \hat{s} \times \hat{s} \times \vec{\boldsymbol{\beta}} - \hat{s} \times \vec{\boldsymbol{\beta}} \times \vec{\boldsymbol{\beta}} \right\} \\
&= \beta_e (\frac{e}{m_e c \gamma}) E_i \left\{ \hat{s} \left(\hat{s} \cdot \vec{\boldsymbol{\beta}} \right) - \vec{\boldsymbol{\beta}} \left(\hat{s} \cdot \hat{s} \right) - \vec{\boldsymbol{\beta}} \left(\hat{s} \cdot \vec{\boldsymbol{\beta}} \right) + \vec{\boldsymbol{\beta}} \left(\hat{s} \cdot \vec{\boldsymbol{\beta}} \right) \right\} \\
&= \beta_e (\frac{e}{m_e c \gamma}) E_i \left\{ \beta_s \hat{s} - \vec{\boldsymbol{\beta}} \right\}
\end{aligned}
$$

Once again, we apply the criteria for an ideal scattering geometry, $\vec{\boldsymbol{E_i}} \cdot \hat{s} = 0$, then the relativistic term can be written as

$$
\hat{e} \cdot \left(\beta_e (\frac{e}{m_e c \gamma}) E_i \left\{ \beta_s \hat{s} - \vec{\boldsymbol{\beta}} \right\} \right) = -\beta_e^2 (\frac{e}{m_e c \gamma}) E_i \tag{2.33}
$$

The Magnetic Field Term: $\vec{\dot{\boldsymbol{\beta}}} = (\frac{e}{m_e c\gamma})\vec{\boldsymbol{E}}_i \left(\vec{\boldsymbol{\beta}} \cdot \hat{i}\right) - \hat{i}\left(\vec{\boldsymbol{\beta}} \cdot (\frac{e}{m_e c\gamma})\vec{\boldsymbol{E}}_i\right)$

Finally, we find the scattered electric field term due to the incident magnetic field contributions; see Eq. (2.11). As in the prior section, we can write the field term as

$$
\begin{aligned}
&\hat{s} \times \left\{\left(\hat{s} - \vec{\boldsymbol{\beta}}\right) \times \vec{\dot{\boldsymbol{\beta}}}\right\} \\
&= \hat{s} \times \left[\left(\hat{s} - \vec{\boldsymbol{\beta}}\right) \times \left\{(\frac{e}{m_e c\gamma})\vec{\boldsymbol{E}}_i \left(\vec{\boldsymbol{\beta}} \cdot \hat{i}\right) - \hat{i}\left(\vec{\boldsymbol{\beta}} \cdot (\frac{e}{m_e c\gamma})\vec{\boldsymbol{E}}_i\right)\right\}\right] \\
&= \hat{s} \times \left[\left(\hat{s} - \vec{\boldsymbol{\beta}}\right) \times \left\{(\frac{e}{m_e c\gamma})E_i\beta_i\hat{e} - (\frac{e}{m_e c\gamma})E_i\beta_e\hat{i}\right\}\right] \\
&= (\frac{e}{m_e c\gamma})E_i\hat{s} \times \left[\beta_e\vec{\boldsymbol{\beta}} \times \hat{i} + \beta_i\hat{s} \times \hat{e} - \beta_i\vec{\boldsymbol{\beta}} \times \hat{e} - \beta_e\hat{s} \times \hat{i}\right] \\
&= (\frac{e}{m_e c\gamma})E_i\beta_e \left\{\vec{\boldsymbol{\beta}}\left(\hat{s} \cdot \hat{i}\right) - \hat{i}\left(\hat{s} \cdot \vec{\boldsymbol{\beta}}\right)\right\} + (\frac{e}{m_e c\gamma})E_i\beta_i \left\{\hat{s}\left(\hat{s} \cdot \hat{e}\right) - \hat{e}\left(\hat{s} \cdot \hat{s}\right)\right\} \\
&- (\frac{e}{m_e c\gamma})E_i\beta_i \left\{\vec{\boldsymbol{\beta}}\left(\hat{s} \cdot \hat{e}\right) - \hat{e}\left(\hat{s} \cdot \vec{\boldsymbol{\beta}}\right)\right\} - (\frac{e}{m_e c\gamma})E_i\beta_e \left\{\hat{s}\left(\hat{s} \cdot \hat{i}\right) - \hat{i}\left(\hat{s} \cdot \hat{s}\right)\right\}
\end{aligned}
$$

and applying the criteria for ideal scattering gives us

$$
\begin{aligned}
&\hat{e} \cdot (\frac{e}{m_e c\gamma})E_i\beta_e \left\{\hat{i}\left(\hat{s} \cdot \hat{s}\right) - \hat{s}\left(\hat{s} \cdot \hat{i}\right)\right\} \\
&+ \hat{e} \cdot (\frac{e}{m_e c\gamma})E_i\beta_e \left\{\vec{\boldsymbol{\beta}}\left(\hat{s} \cdot \hat{i}\right) - \hat{i}\left(\hat{s} \cdot \vec{\boldsymbol{\beta}}\right)\right\} \\
&+ \hat{e} \cdot (\frac{e}{m_e c\gamma})E_i\beta_i \left\{\hat{s}\left(\hat{s} \cdot \hat{e}\right) - \hat{e}\left(\hat{s} \cdot \hat{s}\right)\right\} \\
&- \hat{e} \cdot (\frac{e}{m_e c\gamma})E_i\beta_i \left\{\vec{\boldsymbol{\beta}}\left(\hat{s} \cdot \hat{e}\right) - \hat{e}\left(\hat{s} \cdot \vec{\boldsymbol{\beta}}\right)\right\} \\
&= (\frac{e}{m_e c\gamma})E_i\beta_e^2 \cos\theta - (\frac{e}{m_e c\gamma})E_i\beta_i\left(1 - \beta_s\right)
\end{aligned}
\tag{2.34}
$$

Now that we have simplified the scattered electric field term by term, we can

rewrite Eq. (2.30) as

$$\vec{\boldsymbol{E}}_s(\vec{\boldsymbol{R}}', t') = r_e \left[\frac{E_i}{\gamma \left(1 - \beta_s\right)^3 R'} \left\{ \left(1 - \beta_i\right) \left(1 - \beta_s\right) - \beta_e^2 \left(1 - \cos\theta\right) \right\} \right] \tag{2.35}$$

where $r_e = \dfrac{e^2}{4\pi\epsilon_0 m_0 c^2}$ is the classical electron radius.

The equations for scattered electric field up to this point have not been evaluated for the finite time difference for the signal to arrive at the observer, the retarded time difference, and have therefore been functions of R' and t'. To continue our analysis, we must solve for the scattered electric field measured at the observer's location. To do this, the treatment in Jackson, 1999[10] is followed to arrive at the corrected scattered field

$$\vec{\boldsymbol{E}}_s(\vec{\boldsymbol{R}}, t) = \vec{\boldsymbol{E}}_s(\vec{\boldsymbol{R}}', t') \cos\left[k_s R - \omega_s t - \vec{k} \cdot \vec{r}_{p0} \right] \tag{2.36}$$

where k_s is the Doppler shifted wave-number and ω_s is the Doppler shifted frequency. For this work, only noncollective scattering is considered; the term $\vec{k} \cdot \vec{r}_{p0}$ can be ignored.

Following the work of Sheffield, 2011[5], the time-averaged scattered power per unit solid angle emitted by an accelerated electron is

$$\frac{dP_0}{d\Omega_s} = \frac{c\epsilon_0 R^2}{2} \lim_{T \to \infty} \frac{1}{T} \int_{-\infty}^{\infty} dt |E_s|^2 \tag{2.37}$$

where the limits as $T \to \infty$ imply that T is the integration time of the measurement system. Using Parseval's theorem and performing a Fourier transform of $E_s\left(R, t\right)$,

we can then write Eq. (2.37) and Eq. (2.36) in terms of frequency

$$\frac{d^2P_0}{d\Omega_s d\omega_s} = \frac{c\epsilon_0 R^2}{4\pi} \lim_{T\to\infty} \frac{1}{T} |E_s(\omega_s)|^2 \tag{2.38}$$

and

$$E_s(\omega_s) = r_e \left[\frac{E_{i0} \exp^{jk_s R}}{\gamma (1-\beta_s)^3 R} \left\{ (1-\beta_i)(1-\beta_s) - \beta_e^2 \left(1 - \hat{s}\cdot\hat{i}\right) \right\} \right] 2\pi\delta(\omega_s - \omega_d). \tag{2.39}$$

Substituting Eq. (2.39) into Eq. (2.38), we can finally write the electron power radiated per unit solid area per unit frequency as

$$\frac{d^2P_0}{d\Omega_s d\omega_s} = r_e^2 \left[\langle S_i \rangle \frac{1-\beta^2}{(1-\beta_s)^6} \left\{ (1-\beta_i)(1-\beta_s) - \beta_e^2 \left(1 - \hat{s}\cdot\hat{i}\right)^2 \right\}^2 \right] \kappa\delta(\omega_s - \omega_d) \tag{2.40}$$

where $\langle S_i \rangle = \frac{c\epsilon_0 E_{i0}^2}{2}$.

2.4 Ensemble Scattered Power Spectra

Now that we have the power scattered by an electron, applying this treatment to a collection of electrons of density n_e and with a velocity distribution of $f\left(\vec{\boldsymbol{\beta}}\right)$, we can rewrite Eq. (2.40) as

$$\begin{aligned} \frac{d^2P_0}{d\Omega_s d\omega_s} &= r_e^2 \int_{vol} \langle S_i \rangle n_e d^3\vec{\boldsymbol{r}} \int_{vel} \frac{(1-\beta^2)}{(1-\beta_s)^6} \\ &\times \left\{ (1-\beta_i)(1-\beta_s) - \beta_e^2 \left(1 - \hat{s}\cdot\hat{i}\right) \right\}^2 \\ &\times \kappa f\left(\vec{\boldsymbol{\beta}}\right) \delta(\omega_s - \omega_d) \, d^3\vec{\boldsymbol{\beta}} \end{aligned} \tag{2.41}$$

After simplification [5], Eq. (2.41) is now in the final useful form

$$\begin{aligned}\frac{d^2P_0}{d\Omega_s d\omega_s} &= r_e^2 \int_{vol} \langle S_i \rangle \, n_e d^3\vec{\boldsymbol{r}} \int_{vel} \left(\frac{\omega_s}{\omega_i}\right)^2 \\ &\times \left\{1 - \frac{\beta_e^2\left(1 - \hat{s}\cdot\hat{i}\right)}{\left(1-\beta_i\right)\left(1-\beta_s\right)}\right\}^2 \left(1-\beta^2\right) \\ &\times f\left(\vec{\boldsymbol{\beta}}\right)\delta\left(\vec{k}\cdot\vec{v} - \omega\right) d^3\vec{\boldsymbol{\beta}}\end{aligned} \tag{2.42}$$

In Eq. (2.42), the term $\left(\frac{\omega_s}{\omega_i}\right)^2$ accounts for the measured blue-shift of the scattered light. The second of Eq. (2.42) term represents the depolarization term which accounts for the change in orientation of $\vec{\boldsymbol{E}}_i$ as experienced by a relativistic electron. If desired, the scattered power spectrum can be calculated by performing numerical integration of Eq. (2.42), but this approach is generally avoided[17]. Instead, the next section will develop an analytical expression for the scattered spectrum that a computer can quickly calculate.

2.5 Analytic Formulation of Scattered Spectra

Many authors have developed increasingly accurate expressions for the scattered spectrum from a plasma[5, 17–21], so that work will not be reproduced here. Instead, the analytical formula presented in Naito, 1993, which is accurate to a relative error $< 0.1\%$ up to 100 keV, is presented here. The spectral density function as a function of normalized wavelength shift can be written as

$$S\left(\epsilon,\theta,2\alpha\right) = S_Z\left(\epsilon,\theta,2\alpha\right) q\left(\epsilon,\theta,2\alpha\right) \tag{2.43}$$

where $\epsilon = \dfrac{\lambda_s - \lambda_i}{\lambda_i}$ is the normalized wavelength shift, $2\alpha = \dfrac{m_e c^2}{T_e}$, θ is the scattering angle,

$$S_Z(\epsilon, \theta, 2\alpha) = \frac{\exp^{-2\alpha\chi}}{2K_2(2\alpha)(1+\epsilon)^3\sqrt{2(1-\cos\theta)(1+\epsilon)+\epsilon^2}} \tag{2.44}$$

is the spectral density function developed in [18],

$$q(\epsilon, \theta, 2\alpha) = 1 + \frac{2\chi}{y^3}\exp(2\alpha\chi)\left[y^2\int_\chi^\infty \frac{\exp^{-2\alpha\xi}}{(\xi^2+u^2)\frac{3}{2}}d\xi - 3\int_\chi^\infty \frac{\exp^{-2\alpha\xi}}{(\xi^2+u^2)\frac{5}{2}}\right] \tag{2.45}$$

is the depolarization factor,

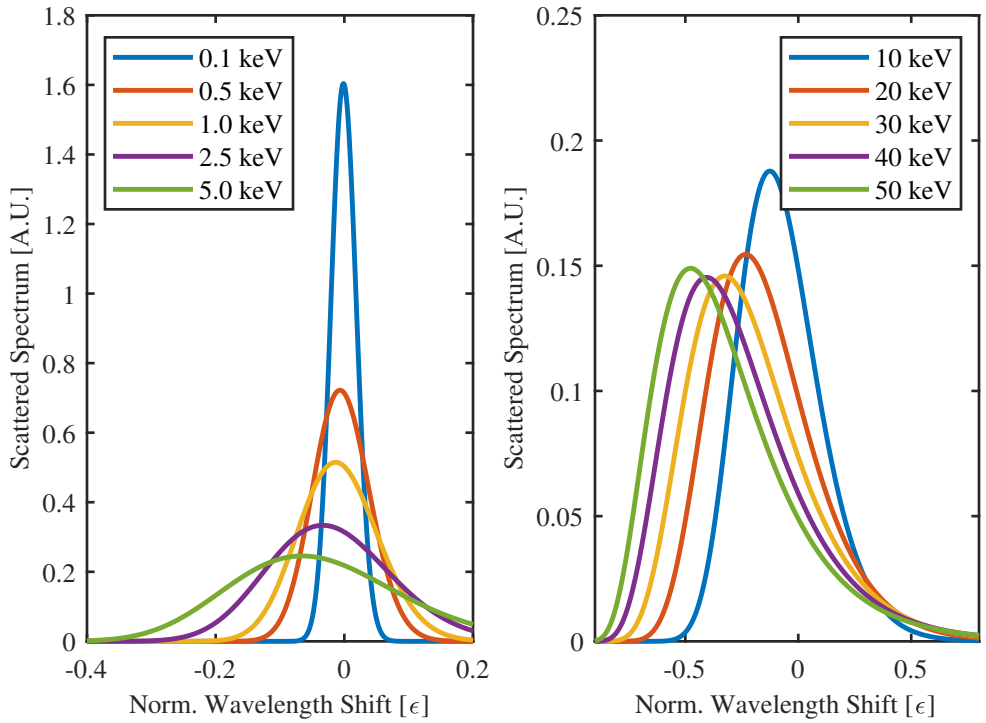

Figure 2.4: Plot of the scattered spectrum as calculated in Eq. (2.49) for (left) 0.1 keV to 5.0 keV and (right) 10 keV to 50 keV.

$$\chi = \sqrt{1 + \frac{\epsilon^2}{2\left(1 - \cos\theta\right)\left(1 + \epsilon\right)}}, \tag{2.46}$$

$$u = \frac{\sin\theta}{1 - \cos\theta}, \tag{2.47}$$

and

$$y = \frac{1}{\sqrt{\chi^2 + u^2}}. \tag{2.48}$$

Expressing the scattered spectrum in the form of the differential photon cross section per unit solid angle per unit wavelength shift leads to Eq. (2.49), which is used extensively in this work.

$$\frac{d^2\sigma_p}{d\Omega_s d\epsilon} = q\left(\epsilon, \theta, 2\alpha\right) r_e^2 S_Z\left(\epsilon, \theta, 2\alpha\right) \tag{2.49}$$

Scattered spectra calculated from Eq. (2.49) are plotted in Fig. 2.4. Scattered spectra for $0.1\ keV < T_e < 5.0\ keV$ are plotted on the left side of Fig. 2.4, showing the spectral broadening and blue-shifting of the spectrum that occurs at increasing T_e. On the right side of Fig. 2.4, spectra for $10\ keV < T_e < 50\ keV$ are plotted. For higher values of T_e, the blue-shift becomes less pronounced and the difference in peak scattered power magnitude begins to converge to a common value.

Bibliography

[5]J. Sheffield, ed., *Plasma scattering of electromagnetic radiation: experiment, theory and computation*, 1st ed (Elsevier, Amsterdam ; Boston, 2011), 497 pp.

[6]I. H. Hutchinson, *Principles of plasma diagnostics*, Repr (Cambridge University Press, Cambridge, 1994), 364 pp.

[7]D. J. Griffiths, *Introduction to electrodynamics*, Fourth edition (Cambridge University Press, Cambridge, United Kingdom ; New York, NY, 2018).

[8]S. L. Prunty, "A primer on the theory of thomson scattering for high-temperature fusion plasmas", Phys. Scr. **89**, Publisher: IOP Publishing, 128001 (2014).

[9]J. P. Freidberg, *Plasma physics and fusion energy*, OCLC: 184904146 (Cambridge University Press, Cambridge, 2007).

[10]J. D. Jackson, *Classical electrodynamics*, 3rd ed (Wiley, New York, 1999), 808 pp.

[11]C. A. Balanis, *Advanced engineering electromagnetics*, 2nd ed (John Wiley & Sons, Hoboken, N.J, 2012), 1018 pp.

[12]M. J. Walsh et al., "Design challenges and analysis of the ITER core LIDAR thomson scattering system", Review of Scientific Instruments **77**, Publisher: American Institute of Physics, 10E525 (2006).

[13]G. S. Kurskiev et al., "A study of core thomson scattering measurements in ITER using a multi-laser approach", Nucl. Fusion **55**, Publisher: IOP Publishing, 053024 (2015).

[14]J. R. Forshaw and A. G. Smith, *Dynamics and relativity*, The Manchester physics series, OCLC: ocn291193458 (John Wiley & Sons, Chichester, UK, 2009), 323 pp.

[15]D. A. Fleisch, *A student's guide to maxwell's equations*, OCLC: ocn173182616 (Cambridge University Press, Cambridge, UK ; New York, 2008), 134 pp.

[16]M. R. Spiegel, S. Lipschutz, and J. Liu, *Mathematical handbook of formulas and tables*, Fourth edition, Schaum's outline (McGraw-Hill, New York, 2013), 293 pp.

[17]T. Matoba et al., "Analytical approximations in the theory of relativistic thomson scattering for high temperature fusion plasma", Jpn. J. Appl. Phys. **18**, Publisher: IOP Publishing, 1127 (1979).

[18]V. A. Zhuravlev and G. D. Petrov, "Scattering of radiation by finite volumes of relativistic plasma streams", Sov. J. Plasma Phys. (Engl. Transl.); (United States) **5:1**, Institution: All-Union Scientific-Research Institute of Physicotechnical and Radiotechnical Measurements (1979).

[19]A. C. Selden, "Simple analytic form of the relativistic thomson scattering spectrum", Physics Letters A **79**, 405–406 (1980).

[20]O. Naito, H. Yoshida, and T. Matoba, "Analytic formula for fully relativistic thomson scattering spectrum", Physics of Fluids B: Plasma Physics **5**, Publisher: American Institute of Physics, 4256–4258 (1993).

[21]J. P. Palastro et al., "Fully relativistic form factor for thomson scattering", Phys. Rev. E **81**, Publisher: American Physical Society, 036411 (2010).

Chapter 3

Thomson Scattering Diagnostic Review

Thomson scattering is a mature plasma diagnostic technique that measures plasma electron temperature and density, T_e & n_e, respectively, with high temporal and spatial resolution. The layout of a typical Thomson scattering system is presented in Fig. 3.1. Since knowledge of the temperature and density of a plasma is of utmost importance when characterizing a plasma discharge, Thomson scattering diagnostics are ubiquitous in almost every major plasma experiment internationally. A brief list of Thomson scattering diagnostic parameters of notable plasma experiments, starting with those located on the UW-Madison campus and moving to other national and international experiments, is presented in Table 3.1.

In this chapter, Section 3.1 introduces the typical components of an experimental Thomson scattering system, followed by a discussion of how the scattered spectra are analyzed in Section 3.2. Closing out the chapter, Section 3.3 describes the HSX

Thomson scattering system before the modifications of Chapter 5 were performed.

Table 3.1: Comparison of standard Thomson scattering diagnostic parameters for a collection of relevant experimental programs.

Experiment	λ_i [nm]	$E_{i,max}$ [J]	δ_t [ns]	f_{max} [Hz]	Channels [#]	T_e [keV]	n_e [$10^{19}m^{-3}$]
HSX[22]	1064	1	8	10	10	5	1
MST[23, 24]	1064	2	10	10 k	21	5	1
Pegasus[25, 26]	532	2	7	10	CCD	0.25	1
W7-X[27]	1064	2.4	10	10 k	10	7	3
ITER[13, 28]	1064	2	10	50	TBD	40	30
Heliotron-J[29]	1064	0.5	10	10	25	10	0.5
LHD[30]	1064	2	10	50	144	10	1.3
KSTAR[31]	1064	2.5	8	20	27	10	UNK

3.1 Thomson Scattering Systems

A typical Thomson scattering diagnostic, like that in Fig. 3.1, directs a high-power radiation beam through the plasma to be measured. As described in Chapter 2, the interaction of the incident beam with the free electrons inside the plasma induces an acceleration of the electrons, resulting in the scattering of the incident light wave. Scattered photons are collected by a system of collection optics and optical fibers that transport the scattered photons to a remote spectrometer. Once the photons are transported to the spectrometer, they are spectrally divided into wavelength bands. Each discrete band of photons is then terminated onto a photodetector and digitized for further analysis. Once the scattered light signal has been digitized, it is processed by an analysis algorithm that statistically determines the shape and intensity of the scattered power spectrum. Assuming a Maxwellian temperature distribution,

measurement of the spectral distribution of the scattered power explicitly determines the bulk plasma electron temperature. Once the electron temperature is determined, the electron density can be inferred by calculating the most likely density at a given T_e to result in the measured scattered signal intensities.

Sections 3.1.1-3.2 provide a detailed discussion of components standard to Thomson scattering diagnostics.

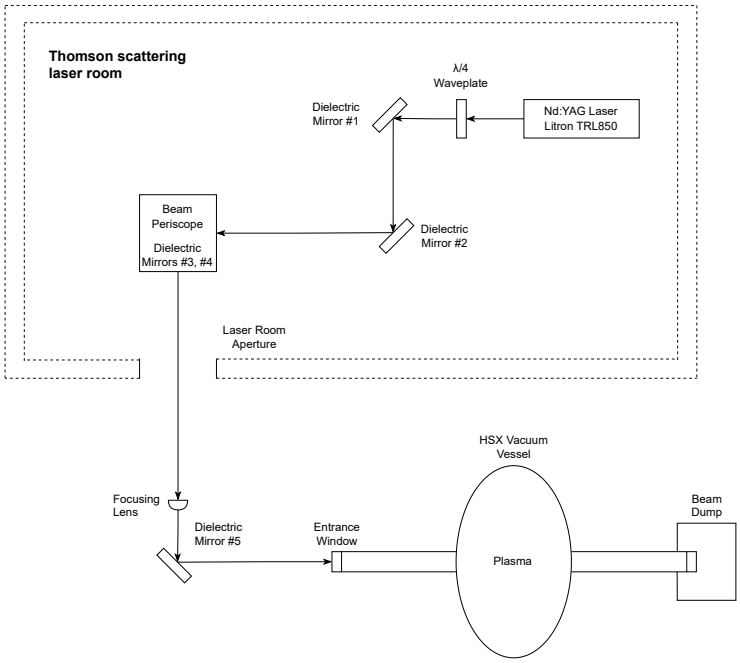

Figure 3.1: Diagram of the beam path for the HSX Thomson scattering diagnostic. This diagram is simplified from the implementation on HSX and is not to scale, but it is accurate enough for this work.

3.1.1 Radiation Source

Depending on the plasma parameters being investigated, Thomson scattering diagnostics can operate with various sources, from visible, IR, microwave, and even x-ray

range[5]. However, for most magnetic confinement experiments and reactor concepts relevant to fusion, incoherent Thomson scattering is generally performed with a high-energy, nanosecond scale, Q-switched Nd:YAG laser operating at a wavelength of 1064 nm. The more basic systems have a single pulse during a discharge, whereas some more sophisticated systems have lasers that can operate at high pulse rates[23, 32].

The motivation to use a laser operating at a longer wavelength, e.g., 1064 nm, in this work is that most scattered radiation will experience significant blue-shifting. Modern silicon photodiodes generally have low quantum efficiency in the UV range. So, keeping the scattered radiation in the visible and near-IR range, where photodiode quantum efficiency remains high, ensures good measured signal levels. Additionally, silicon photodiodes are a mature technology and an economical choice for Thomson scattering diagnostics.

High-power laser sources are required to overcome the fact that under most circumstances, the scattered power from a fusion-relevant plasma is many orders of magnitude less than the incident power. An estimation of the scattered power fraction can be found by considering Eq. (2.42) where the power measured is restricted to the power scattered in a solid angle Ω_s and evaluated along a finite scattering length, L. In this situation, we can show

$$P_s \propto r_e^2 \langle S_i \rangle n_e L d\Omega_s = P_i r_e^2 n_e L d\Omega_s \tag{3.1}$$

where P_i is the input power, n_e is the electron density, and r_e is the classical electron radius. In Eq. (3.1), the scattered power is proportional to the input power and a

factor of plasma and detection system parameters. To evaluate the scattered power, we can rewrite Eq. (3.1) as

$$\frac{P_s}{P_i} \propto r_e^2 n_e L d\Omega_s \tag{3.2}$$

Let us assume a plasma lab has a device with typical parameters $n_e = 1 \times 10^{19}\ m^{-3}$, $L = 0.01\ m$ and $d\Omega_s = 0.02$ Sr. Inserting these values into Eq. (3.2) gives us the scattered power fraction as 1.6×10^{-14}. This example shows that the scattered power collected by a measurement apparatus is minuscule compared to the magnitude of the applied beam power. To further elucidate the challenges associated with Thomson scattered radiation, assume the example plasma lab has a 1 J Nd:YAG laser with a 10 ns pulse width. The input power would be 100 MW, but the total scattered power would be 1.6 μW. While a light signal on the μW is detectable, uncertainties due to the inherent noise properties of photodetectors[33] and background plasma radiation complicate the analysis of Thomson scattered signals. The parameters used for the prior example are consistent with HSX and many plasma laboratories that implement Thomson scattering, thereby showing that the maximization of input power is a priority for experimental Thomson scattering systems.

3.1.2 Beam Path

For the health and safety of people and equipment, it is common practice, if not already mandated by local law, to house the source laser system in a remotely located room designed for laser safety. The beam is directed from the laser room towards the experiment via a system of high-reflectance, dielectric-coated laser line mirrors. See Fig. 3.1 for a simplified HSX Thomson scattering diagnostic beam path diagram.

Ideally, the number of optical elements in the beam path is minimal, as even the best mirrors cause some loss in signal[34]. Each interaction between the beam and a non-ideal optical element causes a small amount of power loss due to a fraction of the light becoming uncollimated, changing polarization, or diverging from the beam path as stray light. Due to the scattered power fraction inherent to Thomson scattering discussed in Section 3.1.1, energy loss in the beam path must be mitigated by minimizing the number of optical element interactions a beam must make.

The input and output laser beam tubes are another critical aspect of the beam path that can affect the amount of stray light. The most common method to reduce stray laser light is to use long beam tubes that encase the laser beam path in and out of the vacuum vessel, shown in Fig. 3.1. These specialized beam tubes are lined with baffles designed to absorb light at the input laser wavelength[22, 35, 36]. It is also common practice to have the beam enter and exit the vessel through an optic mounted at the Brewster angle to maximize transmission, simultaneously reducing stray light.

3.1.3 Collection Optics

Highlighted in Eq. (2.44), the spectral shape and magnitude of the scattered radiation are functions of the scattering angle θ_s. Ideally, optimizing signal and spatial resolution would drive the choice of θ_s, but, in practice, lack of access to plasma vessels due to large coils and support structures more often determines where the collection optics can be fitted, thereby determining the allowable range of θ_s. Collection optics, like those in Fig. 3.6, generally consist of a lens pair that defines the scattering volume as the overlap of the optical sight line and the beam volume. Collection optics also

focus the light on high-transmission fiber optics for transport away from the noisy and treacherous environment around the plasma vessel, which can be remotely detected and analyzed.

3.2 Spectral Analysis

In Thomson scattering, spectral analysis is performed by separating the scattered light with a spectrometer before digitization and using an analysis routine to find the statistically most likely temperature and density combination. Due to the Thomson scattered power fraction discussed in 3.1.1, signal-to-noise requirements make standard spectrometers unusable for analyzing the scattered power spectrum. In order to overcome systematic S/N constraints, polychromators with fewer and broader spectral channels were designed to collect more scattered power per channel[37, 38]. These polychromators were designed such that three to eight spectral channels would cover the entire wavelength range for an experiment, typically 700 - 1062 nm. Light is separated into discrete spectral channels by cascading between interference filters. See Fig. 3.2 for a General Atomics polychromator schematic. HSX is one of many experimental groups that employ the General Atomics polychromator system. Spectral channels from the two versions of the filter set installed on HSX are presented in Fig. 3.3. After photons are spectrally divided by the filter sets of the polychromator, they are then terminated into large gain photodetectors and converted into a current signal. A transimpedance amplifier converts the current signal from the photodetector into a voltage signal that can be digitized and analyzed by specially designed software.

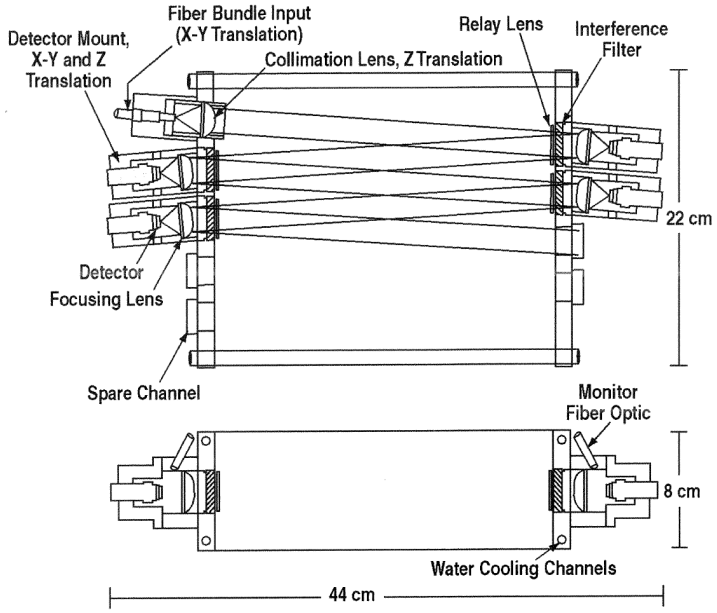

Figure 3.2: Schematic of a polychromator designed and distributed by General Atomics. Most fusion plasma experiments have purchased and adopted these polychromators as one of two major designs commercially available. From *Polychromator Manual: Model GAPB-1064-4-1K*, 1999, General Atomics.

Recalling the expression for the differential photon cross section per electron per unit solid angle per unit wavelength shift from Eq. (2.49), we can now write the equation for the total number of primary photoelectrons created on a spectral channel, j, as[39]

$$N_{S_{pe},j} = n_e \Omega_s L \frac{E_i \lambda_i}{hc} \int_{\epsilon_{j,1}}^{\epsilon_{j,2}} \frac{d^2\sigma_p}{d\Omega_s d\epsilon} T_{opt}(\epsilon)\eta(\epsilon)T_{filt,j}(\epsilon)d\epsilon. \tag{3.3}$$

where n_e is the electron density, Ω_s is the solid angle of the collection system, L is the scattering length in the plasma, E_i is the incident beam energy, λ_i is the incident beam wavelength, h is the Planck constant, c is the speed of light in a vacuum, $T_{opt}(\epsilon)$ is the total optical system transmission as a function of wavelength, $\eta(\epsilon)$ is the wavelength-dependent quantum efficiency of the photodetector, $T_{filt}(\epsilon)$ is the filter transmission

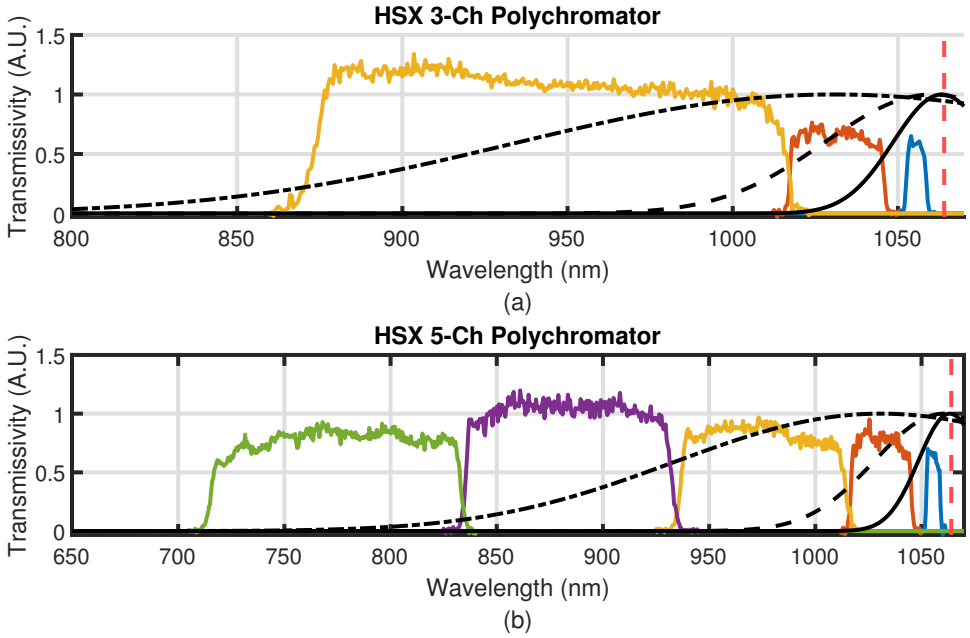

Figure 3.3: Transmission functions for the existing (a) three-channel and (b) five-channel HSX polychromators. The plots include the input laser line, a dashed red line, and the normalized 90° scattering spectra for 50, 250, and 2500 eV, depicted by the black solid, dashed, and dash-dotted lines, respectively.

function, and ϵ is the normalized wavelength shift. With Eq. (3.3) in hand and a calibrated collection system, it becomes a straightforward task to determine the electron temperature and density of the plasma. This discussion will continue in Section 4.1. For now, it will suffice to say that

$$\chi^2 = \sum_{j=1}^{M} \frac{(N_j - N_{S_{pe},j}(T_e, n_e))^2}{\sigma_j^2} \tag{3.4}$$

is minimized to find the most likely temperature and density. In Eq. (3.4), N_j is the measured photoelectrons on wavelength channel j, σ_j is the standard deviation of N_j on wavelength channel j, and $N_{S_{pe},j}(T_e, n_e)$ is the predicted number of photons

collected as a function of T_e and n_e from Eq. (3.3).

3.3 Thomson Scattering on HSX

The Helically Symmetric eXperiment, or HSX, is a uniquely optimized stellarator experiment at the University of Wisconsin-Madison[40]. Fig. 3.4 presents a computer rendering of the HSX device. Section 3.3.1 introduces the HSX experiment, and the

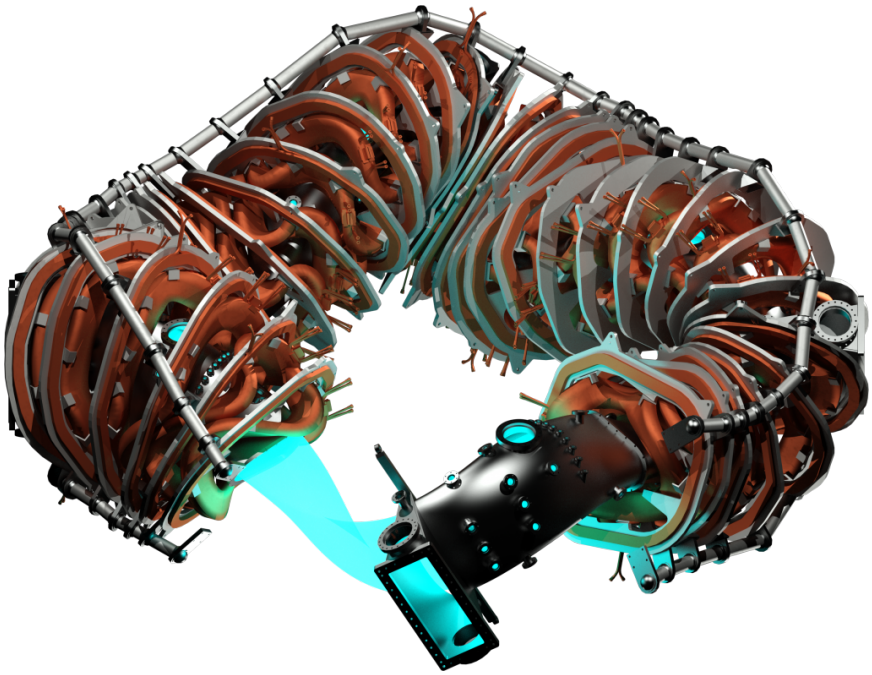

Figure 3.4: Rendering of the HSX experimental vessel without any diagnostic or support system connections. A quadrant of the coils and support structure is cut away in this rendering to show the underlying vacuum vessel and the plasma confined in blue.

need for using Thomson scattering diagnostics on HSX is motivated. In Section 3.3.2, a description of the HSX Thomson scattering diagnostic prior to the implementation of system improvements, introduced in Chapter 5, is presented. It is essential to

understand the initial state of this diagnostic to give the reader a complete picture of the magnitude of system changes performed in this work.

3.3.1 The Helically Symmetric eXperiment

Various approaches have been developed to confine high-temperature plasmas, including, but not limited to, magnetic mirrors, toroidal devices, and inertial confinement approaches. Toroidal devices are a broad category that includes symmetric devices, e.g., tokamaks, and asymmetric devices like stellarators, the latter of which includes HSX and the focus of this section. Initially invented in 1951 by Lyman Spitzer[41], a stellarator is a three-dimensional device that uses external coils to generate the magnetic field structure needed for plasma confinement. Unlike tokamaks, which require current within the plasma to generate poloidal components of their magnetic field, stellarators are inherently steady-state devices, a significant advantage for potential power generation. However, implementing physically realizable field coils can introduce finite field errors that lead to performance degradation[42], e.g., poor particle and energy confinement, which must be mitigated for a power generation concept based on magnetic confinement to be successful.

Advanced computation power has allowed for the targeted optimization of stellarator field coils, enabling the development of stellarators with significantly improved performance over the non-optimized stellarator. HSX was designed and optimized for a magnetic field with a symmetry in the helical direction. With this unique design, HSX is currently the world's only stellarator optimized for quasi-helical symmetry. Experimentally, HSX has shown improved particle confinement when compared to predictions by neoclassical theory[43]. With the success of HSX, optimized stellara-

tors are once again an attractive option for a fusion reactor power plant[44].

3.3.2 The HSX Thomson Scattering Diagnostic

HSX currently has a Thomson scattering system that measures ten spatial channels across the lower half-plane radius. A Q-switched Litron Nd:YAG laser provides the probe pulse of 850 mJ within a 6.25 ns full width at half maximum (FWHM) pulse at the fundamental 1064 nm wavelength. The laser is housed in a laser-safe room on the lower level of the HSX lab. A system of four 1064 nm laser-line, dielectric-coated mirrors direct the beam out of the laser safety room to a vessel entrance port. In order to maximize energy throughput, the beam enters the vessel via a vacuum Brewster window. Then, it traverses the entrance tube lined with stray light mitigation baffles. Scattered radiation from the plasma beam interaction at ten radial locations, defined by their scattering angles calculated in Fig. 3.5, is collected by BK7 and SF1 glass doublet optics that image the light onto ten radial fibers with a numerical aperture

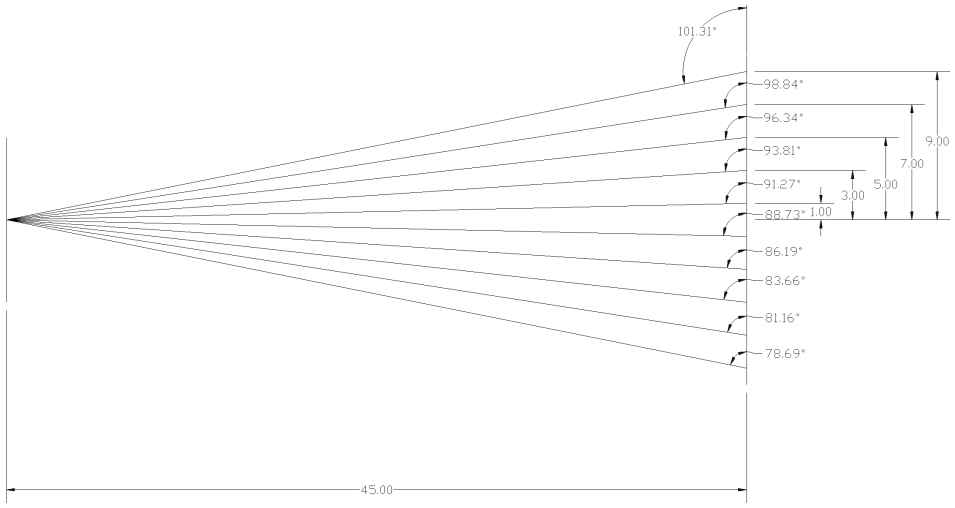

Figure 3.5: CAD drawing design of the collection optic scattering angles.

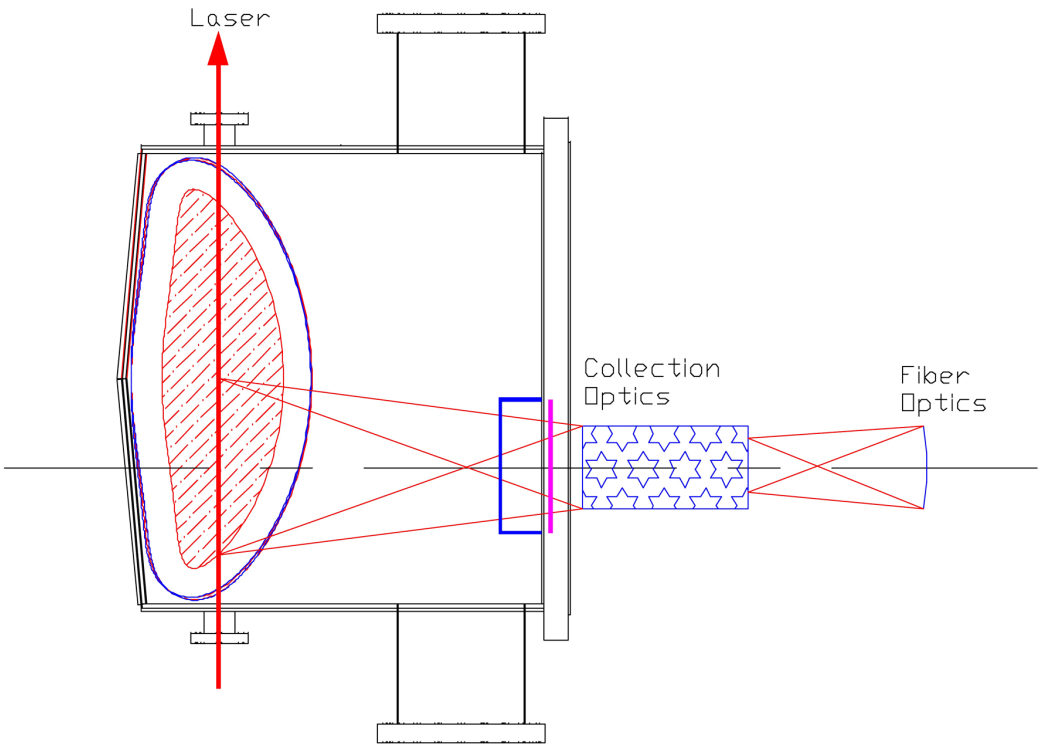

Figure 3.6: CAD drawing design of the collection optic system, including the HSX vessel and the plasma surfaces being measured.

(NA) of 0.23. Fig. 3.6 presents a CAD drawing of the HSX vessel, the beam path through the plasma, the plasma surfaces as calculated, and the collection optics used in the HSX Thomson scattering diagnostic.

Each collection fiber is a 7 m CeramOptec Ultra-low OH, linear-to-round fiber bundle that contains 126 individual fibers. CAD designs of the fiber bundles are presented in Fig. 3.7. The fiber bundles couple the collected light to ten General Atomics (GA) GAPD-1064-4-1K polychromators[37, 45]. Located internally to the GA polychromators, EG&G C30956E[33] Si avalanche photodiodes (APDs) convert the scattered light signal into an electrical current, which is then processed into an output voltage for digitization, previously performed by a LeCroy Model 2250 charge

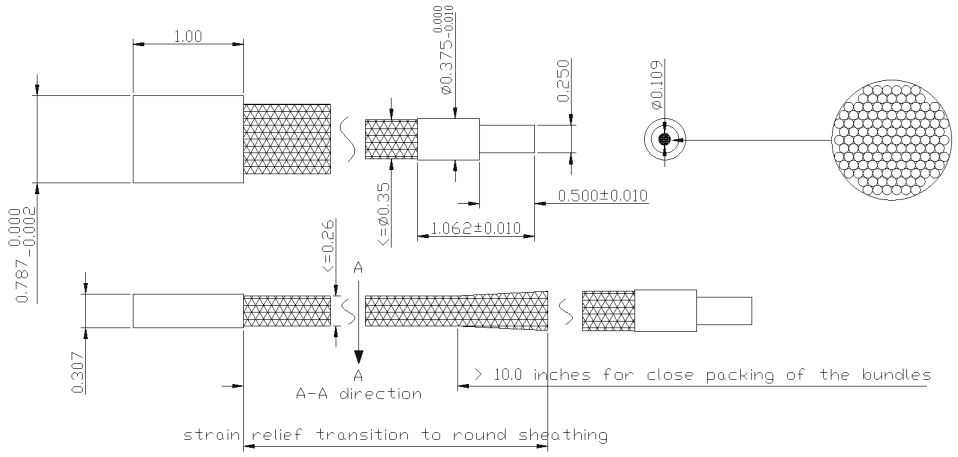

Figure 3.7: CAD drawing design of the round-end HSX fiber bundles.

integrator. Since the DC component of the plasma background radiation is undesirable when computing Thomson scattered profiles, an AC-coupled output that removes

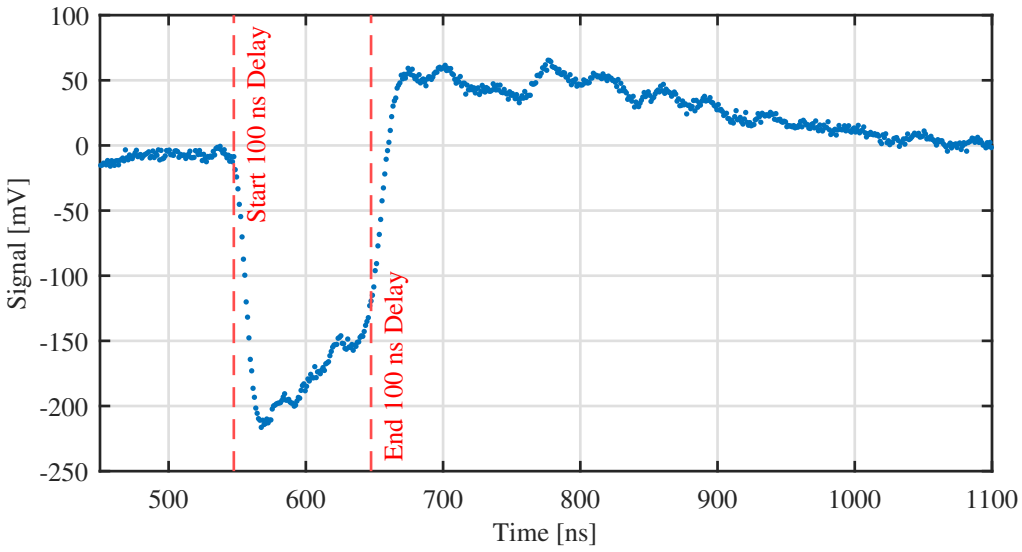

Figure 3.8: Raman scattered data on the polychromator AC output channel digitized by a 4 GSa/s oscilloscope. The steep transition from negative to positive at ~650 ns is caused by the polychromator electronics' internal 100 ns delay line circuit. To not be affected by the internal delay line, all scattered signals should be no longer than 100 ns.

the extraneous DC signal is often implemented. The GA polychromator electronics performed AC-coupling using a 100 ns delay line technique that subtracts the delayed background signal from the non-delayed signal, approximately removing contributions from the background plasma light, assuming the background light intensity does not change significantly on the order of the delay line period.

Initially designed as identical polychromators with four dedicated spectral channels each, the GA polychromators had been modified from their original specifications to allow the five core spatial channels to have five spectral channels each. In contrast, the five edge spatial channels only have three spectral channels each, as shown in Fig. 3.3. Due to issues with low signal intensity, passive component changes were previously made to polychromator electronics to increase the system gain. The system response of the existing HSX Thomson scattering diagnostic is plotted in Fig. 3.8.

Bibliography

[5]J. Sheffield, ed., *Plasma scattering of electromagnetic radiation: experiment, theory and computation*, 1st ed (Elsevier, Amsterdam ; Boston, 2011), 497 pp.

[13]G. S. Kurskiev et al., "A study of core thomson scattering measurements in ITER using a multi-laser approach", Nucl. Fusion **55**, Publisher: IOP Publishing, 053024 (2015).

[22]K. Zhai et al., "Performance of the thomson scattering diagnostic on helical symmetry experiment", Review of Scientific Instruments **75**, Publisher: American Institute of Physics, 3900–3902 (2004).

[23]W. C. Young et al., "High-repetition-rate pulse-burst laser for thomson scattering on the MST reversed-field pinch", J. Inst. **8**, C11013 (2013).

[24]L. Morton, "Turbulence and transport in magnetic islands in MST and DIII-d", PhD thesis (UW - Madison, Aug. 1, 2016), 171 pp.

[25]G. M. Bodner et al., "Control and automation of the pegasus multi-point thomson scattering system", Review of Scientific Instruments **87**, Publisher: American Institute of Physics, 11E523 (2016).

[26]D. J. Schlossberg et al., "A novel, cost-effective, multi-point thomson scattering system on the pegasus toroidal experiment (invited)", Review of Scientific Instruments **87**, Publisher: American Institute of Physics, 11E403 (2016).

[27]S. A. Bozhenkov et al., "The thomson scattering diagnostic at wendelstein 7-x and its performance in the first operation phase", J. Inst. **12**, P10004 (2017).

[28]M. Bassan et al., "Thomson scattering diagnostic systems in ITER", J. Inst. **11**, C01052 (2016).

[29]M. Takashi, "Present status of the nd:YAG thomson scattering system development for time evolution measurement of plasma profile on heliotron j", Plasma Sci. Technol. **15**, 240 (2013).

[30]I. Yamada et al., "Calibrations of the LHD thomson scattering system", Review of Scientific Instruments **87**, Publisher: American Institute of Physics, 11E531 (2016).

[31]J. H. Lee et al., "Research of fast DAQ system in KSTAR thomson scattering diagnostic", J. Inst. **12**, C12035 (2017).

[32]D. J. D. Hartog et al., "A pulse-burst laser system for thomson scattering on NSTX-u", J. Inst. **12**, C10002 (2017).

[33]Excelitas, *C30954eh, c30955eh and c30956eh series long wavelength enhanced silicon avalanche photodiodes datasheet*, Sept. 10, 2016.

[34]*1064nm, 45˚ 25.4mm dia. nd:YAG IBS low loss laser line mirror*, https://www.edmundoptics.ca/p/1064nm-45deg-254mm-dia-ndyag-ibs-low-loss-laser-line-mirror/31960/ (visited on 11/01/2023).

[35]C. M. Jacobson et al., "Identification and mitigation of stray laser light in the thomson scattering system on the madison symmetric torus (MST)", Review of Scientific Instruments **87**, Publisher: American Institute of Physics, 11E511 (2016).

[36]D. G. Nilson et al., "Thomson scattering stray light reduction techniques using a CCD camera", Review of Scientific Instruments **68**, 704–707 (1997).

[37]T. N. Carlstrom et al., "Design and operation of the multipulse thomson scattering diagnostic on DIII-d (invited)", Review of Scientific Instruments **63**, Publisher: American Institute of Physics, 4901–4906 (1992).

[38]R. Scannell et al., "Design of a new nd:YAG thomson scattering system for MAST", Review of Scientific Instruments **79**, Publisher: American Institute of Physics, 10E730 (2008).

[39]O. Naito et al., "How many wavelength channels do we need in thomson scattering diagnostics?", Review of Scientific Instruments **70**, Publisher: American Institute of Physics, 3780–3781 (1999).

[40]A. Almagri et al., "A helically symmetric stellarator (HSX)", IEEE Transactions on Plasma Science **27**, Conference Name: IEEE Transactions on Plasma Science, 114–115 (1999).

[41]L. Spitzer, "The stellarator concept", The Physics of Fluids **1**, Publisher: American Institute of Physics, 253–264 (1958).

[42]A. H. Boozer, "Non-axisymmetric magnetic fields and toroidal plasma confinement", Nucl. Fusion **55**, Publisher: IOP Publishing, 025001 (2015).

[43]J. M. Canik et al., "Experimental demonstration of improved neoclassical transport with quasihelical symmetry", Phys. Rev. Lett. **98**, Publisher: American Physical Society, 085002 (2007).

[44]Type One Energy Group, Inc., *Stellarator fusion company, type one energy group, raises $29 million in first financing, appointing Christofer Mowry as CEO*, Letter, Mar. 28, 2023.

[45]C. L. Hsieh et al., "Silicon avalanche photodiode detector circuit for nd:YAG laser scattering", Review of Scientific Instruments **61**, Publisher: American Institute of Physics, 2855–2857 (1990).

Chapter 4

Error Analysis

In order to assess the ability of spectroscopic systems based on polychromators to determine T_e and n_e from a Thomson scattered light signal, a figure-of-merit (FOM) that accounts for inherent system error must be derived. For the analysis of Thomson scattering diagnostics, Section 4.1 derives relative error functions $\delta T_e = \frac{\sigma_{T_e}(T_e)}{T_e}$ and $\delta n_e = \frac{\sigma_{n_e}(n_e)}{n_e}$. This work will use δT_e and δn_e as the primary FOMs. Section 4.2 will discuss the individual terms of $\delta T_e/\delta n_e$ and how they can be improved through design optimization.

4.1 Error Analysis

To begin deriving the Thomson scattering FOMs, start by recalling the photon differential cross section from Eq. (2.49), the scattered power from Eq. (3.1), and the equation of photon energy, $E_{photon} = \frac{hc}{\lambda}$. By combining these three equations, the number of Thomson scattered photons collected by a diagnostic with lossless optics,

N_S, can be written as

$$N_S = n_e \Omega_s L \frac{E_i \lambda_i}{hc} \int_\epsilon \frac{d^2\sigma_p}{d\Omega_s d\epsilon} d\epsilon. \tag{4.1}$$

In Eq. (4.1), n_e is the electron density, Ω_s is the solid angle of collection, L is the scattering volume length, E_i is the total incident radiation energy, λ_i is the wavelength of the incident radiation, ϵ is the normalized wavelength shift $\epsilon = \frac{\lambda_s - \lambda_i}{\lambda_i}$, λ_s is the wavelength of the scattered radiation, and $\frac{d^2\sigma_p}{d\Omega_s d\epsilon}$ is the differential photon cross section per unit solid angle per unit wavelength shift from Eq. (2.49). The lone factor of L in Eq. (4.1) comes from the definition of electron density, $n_e = \frac{N}{V}$, where N is the number of electrons and V is the scattering volume defined as $V = LA_{beam}$, where A_{beam} is the cross-sectional area of the input beam.

A filter with a finite bandwidth can be described by the function $T_{filter}(\epsilon)$, which is the filter's transmission as a function of wavelength shift, ϵ. Assuming an ideal filter set that contains M lossless spectral filters on the spectral domain defined by $\epsilon_0 \leq \epsilon \leq \epsilon_{max}$, a set unit functions can define the filter set

$$T_{filt,j}(\epsilon) = u_j(\epsilon - \epsilon_{j,1}) - u_j(\epsilon - \epsilon_{j,2}) \tag{4.2}$$

where $1 \leq j \leq M$.

The modeled number of photons collected per spectral channel can now be written as

$$N_{S,j} = n_e \Omega_s L \frac{E_i \lambda_i}{hc} \int_{\epsilon_{j,1}}^{\epsilon_{j,2}} \frac{d^2\sigma_p}{d\Omega_s d\epsilon} T_{filt,j}(\epsilon) d\epsilon \tag{4.3}$$

In order to get the total number of photoelectrons detected on a spectral channel, detector quantum efficiency, and total optical transmission must be accounted for,

leading to the total measured photoelectrons

$$N_{S_{pe},j} = n_e \Omega_s L \frac{E_i \lambda_i}{hc} \int_{\epsilon_{j,1}}^{\epsilon_{j,2}} \frac{d^2\sigma_p}{d\Omega_s d\epsilon} T_{opt}(\epsilon) \eta(\epsilon) T_{filt,j}(\epsilon) d\epsilon \tag{4.4}$$

where $T_{opt}(\epsilon)$ is the total system transmission, not including the filter functions, and $\eta(\epsilon)$ is the quantum efficiency of the detector.

T_e and n_e of a plasma are determined by minimizing a χ^2 relation

$$\chi^2 = \sum_{j=1}^{M} \left[\frac{N_j - N_{S_{pe},j}(T_e, n_e)}{\sigma_j} \right]^2 \tag{4.5}$$

where N_j is the measured photoelectrons on wavelength channel j and σ_j is the uncertainty of N_j on wavelength channel j.

In order to get an equation for δT_e or δn_e, parameter error terms σ_{T_e} and σ_{n_e} must first be derived. Following the work of Bevington and Robinson, 2003[46], Eq. (4.5) is a non-linear χ^2 fitting routine and can be rewritten in standard χ^2 form

$$\chi^2 = \sum_{j=1}^{M} \left[\frac{y_j - y(x_i)}{\sigma_j} \right]^2 \tag{4.6}$$

where $x_i = [T_e, n_e]$. The curvature matrix, α_{jk}, that describes equations in the form of Eq. (4.6)[46], can be constructed using Eq. (4.7).

$$\alpha_{jk} = \sum \left[\frac{1}{\sigma_j^2} \frac{\partial y(a_0)}{\partial a_j} \frac{\partial y(a_0)}{\partial a_k} \right] \tag{4.7}$$

For least-squares problems, the error matrix $\boldsymbol{\epsilon}$ is the inverse of the curvature matrix

$$\boldsymbol{\epsilon} = \boldsymbol{\alpha}^{-}1 \tag{4.8}$$

and the diagonal elements are the variances of parameters, $a_j = \epsilon_{jj}$. Analysis of Eq. (4.5) with Eq. (4.7) and Eq. (4.8) leads to the approximate formulas for the estimated variance of T_e and n_e.

$$\sigma^2_{T_e} = \frac{\sum(\frac{N_{S_{pe},j}}{\sigma_j})^2}{\sum(\frac{\partial N_{S_{pe},j}}{\partial T_e}\frac{1}{\sigma_j})^2 \sum(\frac{N_{S_{pe},j}}{\sigma_j})^2 - \left[\sum(\frac{\partial N_{S_{pe},j}}{\partial T_e}\frac{N_{S_{pe},j}}{\sigma_j^2})\right]^2} \tag{4.9}$$

$$\sigma^2_{n_e} = \frac{n_e \sum(\frac{\partial N_{S_{pe},j}}{\partial T_e}\frac{1}{\sigma_j})^2}{\sum(\frac{\partial N_{S_{pe},j}}{\partial T_e}\frac{1}{\sigma_j})^2 \sum(\frac{N_{S_{pe},j}}{\sigma_j})^2 - \left[\sum(\frac{\partial N_{S_{pe},j}}{\partial T_e}\frac{N_{S_{pe},j}}{\sigma_j^2})\right]^2} \tag{4.10}$$

Comparing Eq. (4.9) and Eq. (4.10), it is clear that in order to minimize the standard deviation, also referred to as the uncertainty, of a measurement, σ_{T_e}, the common denominator

$$\sum(\frac{\partial N_{S_{pe},j}}{\partial T_e}\frac{1}{\sigma_j})^2 \sum(\frac{N_{S_{pe},j}}{\sigma_j})^2 - \left[\sum(\frac{\partial N_{S_{pe},j}}{\partial T_e}\frac{N_{S_{pe},j}}{\sigma_j^2})\right]^2 \tag{4.11}$$

must be maximized. Following the rules of summation, for $j > 1$,

$$\sum(\frac{\partial N_{S_{pe},j}}{\partial T_e}\frac{1}{\sigma_j})^2 \sum(\frac{N_{S_{pe},j}}{\sigma_j})^2 > \left[\sum(\frac{\partial N_{S_{pe},j}}{\partial T_e}\frac{N_{S_{pe},j}}{\sigma_j^2})\right]^2 \tag{4.12}$$

therefore, to maximize the denominator of Eq. (4.9), it is convenient to focus on

maximizing

$$\sum\left(\frac{\partial N_{S_{pe},j}}{\partial T_e}\frac{1}{\sigma_j}\right)^2 \sum\left(\frac{N_{S_{pe},j}}{\sigma_j}\right)^2 \tag{4.13}$$

to reduce system errors. The physical meaning of the variables in Eq. (4.13) as well as methods to maximize Eq. (4.13) will be discussed in greater detail in Section 4.2.

4.2 Systematic Error Reduction

Referring to Eq. (4.13) derived in Section 4.1, it is convenient for the diagnostic engineer to separate the terms of interest from this equation and analyze how they can be optimized in order to decrease measurement uncertainty. From inspection, three unique terms can be manipulated to maximize Eq. (4.13). The three terms that the diagnostics engineer can manipulate are $N_{S_{pe},j}$, σ_j, and $\sum_j \frac{\partial N_{S_{pe},j}}{\partial T_e}$. The following subsections will discuss the physical meaning of each term and its effect on the combined measurement error.

4.2.1 Increasing $N_{S_{pe},j}$

When analyzing Thomson scattering system error, the simplest and most effective parameter to adjust is the total number of photoelectrons measured in spectral channel j, $N_{S_{pe},j}$. Recalling Eq. (4.4), multiple parameters can be adjusted to increase $N_{S_{pe},j}$, with varying degrees of efficacy. A brief discussion of the feasibility and effect of adjusting each variable of Eq. (4.4) follows.

Increase n_e

Since $N_{S_{pe},j}$ is directly proportional to n_e, it would seem like the apparent plasma parameter to adjust. Unfortunately, n_e is operationally challenging to increase due to density limitations set by heating configurations or device topology constraints. There are also situations, like studying edge plasmas or low-collisionality regimes, when low-density plasmas are the desired state. Increasing n_e is not a realistic possibility and may even be counterproductive. Another issue with increasing electron density is that in devices operating in high-density regimes, e.g., $n_e \geq 1 \times 10^{22}\ m^{-3}$, the scattered signal begins to pale compared to the plasma background radiation. High-density background radiation, proportional to n_e^2, is called Bremsstrahlung, and it presents engineering challenges for diagnostic development in high-density fusion devices.

Increase Ω_s or L

Another variable in Eq. (4.4) that seems promising as a way to increase $N_{S_{pe},j}$ is the solid angle of collection, Ω_s. This variable is generally challenging to adjust, as limited vessel access limits the size of collection optics that can be installed. Increasing the scattering length, L, can be readily dismissed as this would reduce spatial resolution.

Increase E_i

Increasing the incident laser energy is the most straightforward method of increasing $N_{S_{pe},j}$, but there are significant barriers to increasing the laser energy. The primary issue with a more powerful laser is the cost involved. Unfortunately, technology has yet to advance such that off-the-shelf Nd:YAG lasers remain prohibitively expensive. When using a more energetic source, a couple of issues must be evaluated. First,

the pulse lengths will increase, which lowers the temporal resolution. Additionally, increasing the input power will lead to a proportional increase in power lost to stray light. Additional stray light could be a problem because filters may not provide enough optical density to mitigate the stray light.

Increases to T or η

Increases to transmission functions are not realizable as most coefficients are almost as close to 100% as theoretically possible. In a similar argument, the quantum efficiency, η, is likely to increase with a significant advance in photodiode technology.

4.2.2 Decreasing σ_j

σ_j is the standard deviation of the total number of photoelectrons measured on an individual spectral channel, j. Once again, assuming the ideal scattering conditions described in Section 2.1, the total measured signal can be described as a combination of scattered light, plasma background light, line radiation, and electronic noise from the amplification circuit.

Since the scattering signal, $N_{S_{pe},j}$, is commonly obtained by subtracting a pulse-free background signal from the total measured signal[39, 45, 47], the noise contribution from background light, $N_{bg,j}$ is doubled. Therefore, the total standard deviation for spectral channel j, σ_j can be expressed as

$$\sigma_j = \sqrt{k(N_{S_{pe},j} + 2N_{bg,j}) + 2N_{amp}^2} \tag{4.14}$$

N_{amp} is the equivalent number of photoelectrons referenced to the detector from

amplifier noise contributions[13] and where k is the excess noise factor of the avalanche photodiode (APD). At low signal levels, uncertainty in $N_{S_{pe},j}$ is dominated by Poisson statistics, where uncertainty is directly proportional to the square root of the number of photons collected.

Before discussing which parameters can be adjusted, the reason for $N_{S_{pe},j}$ being in the equation for σ_j is because Poisson statistics determine the number statistics of small signal photodiodes, so reducing $N_{S_{pe},j}$ would only be beneficial in the limit of being entirely sure no photons were collected if there is no signal whatsoever.

Decreasing $2N_{bg,j}$

The easiest method to reduce the background noise term in σ_j would be to eliminate the need for subtracting the measured signal from a background signal by AC coupling the output of the polychromator electronics. AC coupling removes the DC offset in a signal by rejecting the DC component of a signal, often by using DC-blocking capacitors or pulse transformers. By AC coupling the signal output instead of using analog subtraction methods, the output signal would have the effect of halving the background noise term with minimal effort.

Since background light is proportional to the measurement's integration time, reducing the integration time can also decrease this term. However, there is a limit to how much the integration time can be reduced; low-bandwidth electronics can require integration times greater than 100 ns, even for incident pulses of only ten ns. This limitation can be relaxed by increasing the bandwidth of the amplification electronics such that the minimum integration time is effectively the pulse length.

Reducing $2N_{amp}^2$

As with the previous discussion, the amplification noise term can be halved by simply AC-coupling the amplifier output signal. Another method of reducing the amplifier noise contribution term is replacing the existing electronics with ultra-low noise components and adhering to PCB layout methods for reducing noise.

Reducing σ_j with Curve Fitting Routines

Another method of reducing uncertainty due to noise is to implement curve-fitting routines that will, assuming a sufficiently high $\frac{S}{N}$ and a very well-characterized signal to fit, remove many noise contributions from the signal. This approach requires high-speed digitization and does not apply to low-bandwidth electronics or systems that use charge integration techniques for digitization.

4.2.3 Increasing $\sum_j \frac{\partial N_{S_{pe},j}}{\partial T_e}$

Finally, the third term that can be manipulated is the rate of change of measured photoelectrons as a function of electron temperature, $\sum \frac{\partial N_{S_{pe},j}}{\partial T_e}$. Assuming a predefined Thomson scattering diagnostic that collects data on a plasma with a given T_e and n_e, the only variable that can be manipulated to increase the magnitude of $\sum_j \frac{\partial N_{S_{pe},j}}{\partial T_e}$ is the number of channels being summed over, j, while keeping the total wavelength bandwidth of $T_{filt,T}$ static. In practice, this would be accomplished by increasing the channel density so that the filter function would approach that of a standard spectrometer. As discussed in Section 3.1.1, S/N constraints require using a polychromator with wide spectral channels. When addressing optimum $T_{filt,j}$,

the literature does not discuss increasing $\sum_j \frac{\partial N_{S_{pe},j}}{\partial T_e}$. A novel method of increasing $\sum_j \frac{\partial N_{S_{pe},j}}{\partial T_e}$ is introduced in Chapter 6.

Bibliography

[13]G. S. Kurskiev et al., "A study of core thomson scattering measurements in ITER using a multi-laser approach", Nucl. Fusion **55**, Publisher: IOP Publishing, 053024 (2015).

[39]O. Naito et al., "How many wavelength channels do we need in thomson scattering diagnostics?", Review of Scientific Instruments **70**, Publisher: American Institute of Physics, 3780–3781 (1999).

[45]C. L. Hsieh et al., "Silicon avalanche photodiode detector circuit for nd:YAG laser scattering", Review of Scientific Instruments **61**, Publisher: American Institute of Physics, 2855–2857 (1990).

[46]P. R. Bevington and D. K. Robinson, *Data reduction and error analysis for the physical sciences*, 3rd ed (McGraw-Hill, Boston, 2003), 158 pp.

[47]T. Deterley et al., "Description and preliminary results of a new photo detector for the DIII-d thomson scattering diagnostic", in 2009 23rd IEEE/NPSS symposium on fusion engineering (June 2009), pp. 1–4.

Chapter 5

Upgrade of the HSX Thomson Scattering Diagnostic

As discussed in Section 3.1.1, Thomson scattering systems' restrictive scattered power magnitude requires that error due to primary and secondary system components be quantified and subsequently minimized. This constraint is even more prevalent for plasma experiments with relatively low electron densities, such as HSX, where photon statistics are the primary source of measurement uncertainty and unmitigated systematic errors can quickly nullify any statistical power the measurement may have. To decrease systematic measurement uncertainty, henceforth referred to as σ_{T_e} from Eq. (4.9), upgrades and improvements have been made to the existing HSX Thomson scattering diagnostic[48]. Changes to the HSX Thomson scattering system include implementation of high-speed ADCs, new high-bandwidth detection electronics, development of a Bayesian analysis routine to solve for T_e and n_e, beam path alterations, system model improvements, and improved calibration procedures. In the following

sections, system modifications are motivated, and test results are presented and discussed.

5.1 High Speed Digitization

Digitization on the previously existing HSX Thomson scattering system was performed by LeCroy Model 2250 charge integrating digitizers[22], also known as QDCs. These QDCs would receive an external trigger from the Thomson laser to initialize the gated digital charge integration. The resultant integrated value would be stored as a digital value proportional to the integrated signal. The primary drawback to using a QDC-based digitization scheme is the inability to inspect a time-domain signal to discriminate corrupted signals. In well-controlled experimental environments, there may be no need to conduct quality checks on the integrated signal, as one can be assured that the measured value is solely caused by the phenomena being measured.

Conversely, many radiation sources may interfere with the collected Thomson scattered spectrum in high-temperature plasma experiments. Stray laser light can interfere with any spectral channels with insufficient optical density at the laser wavelength. Even less predictable than stray light, sporadic impurities within the plasma being studied may intermittently emit line radiation with spectral components that overlap with the Thomson system spectral range[31]. In a Thomson scattering diagnostic based on QDC digitizers, the experimentalist cannot discern which signals may have been affected by spurious signals, limiting their ability to discard measurements that have been corrupted reliably.

In order to avoid the pitfalls associated with QDC-based systems, it has been

shown that using digitizers with high enough sampling rates to reproduce the pulsed signal accurately comes with great benefit[31]. Two significant benefits are realized with a time-resolved measurement of a pulsed signal. First, a time-resolved measurement of scattered radiation allows the experimentalist to validate the collected data and discriminate corrupted signals, e.g., acute external noise or stray light. A second significant benefit of switching from QDCs to ADCs allows for the use of pulse fitting techniques that can reduce or eliminate unwanted and spurious contributions to the measured signal as well as provide information on the uncertainty of the fitted curve[31, 49, 50].

For the HSX Thomson upgrade, existing LeCroy QDCs have been replaced by a CAEN crate that contains three VX1743 12-bit, 3.2 GSa/s, switched capacitor digitizers[51], for a total of 48 high-speed ADC channels. Switched capacitor digitizers function by continuously sampling a signal along an array of capacitor cells, 1,024 cells for the VX1743. When the digitizer receives an acquisition trigger, it freezes the buffered capacitors at their current value and samples each consecutive capacitor cell. The primary benefit of switched capacitor digitization is that extremely fast effective digitization rates are achievable for an order of magnitude reduction in cost compared to equivalent streaming ADCs commonly used in experimental settings.

While switched capacitors allow for high performance at a much lower cost than traditional digitization, the nature of the switched capacitor array leads to two major drawbacks that must be evaluated. Since the capacitor array used on the VX1743 is only 1,024 cells in length, this sets the maximum number of samples per acquisition at 1,024 for 332.5 ns of sampled data. In addition to the limited number of samples per acquisition, the sequential cell digitization performed by the VX1743 digitizer

causes a dead time of 115 μs between acquisitions. Since the current HSX Thomson scattering system can only perform one measurement per 50 ms plasma discharge, the dead time restriction of the VX1743 will not be a factor in the maximum measurement repetition rate. Recalling Fig. 3.8, only the first 100 ns of the pulse is digitized, but the actual pulse is roughly 550 ns. Although the initial 100 ns of the prior Thomson measurement could quickly be recorded by the VX1743, switching to high-speed digitization further motivated the necessity to increase the bandwidth of the existing detection electronics on the HSX Thomson scattering diagnostic.

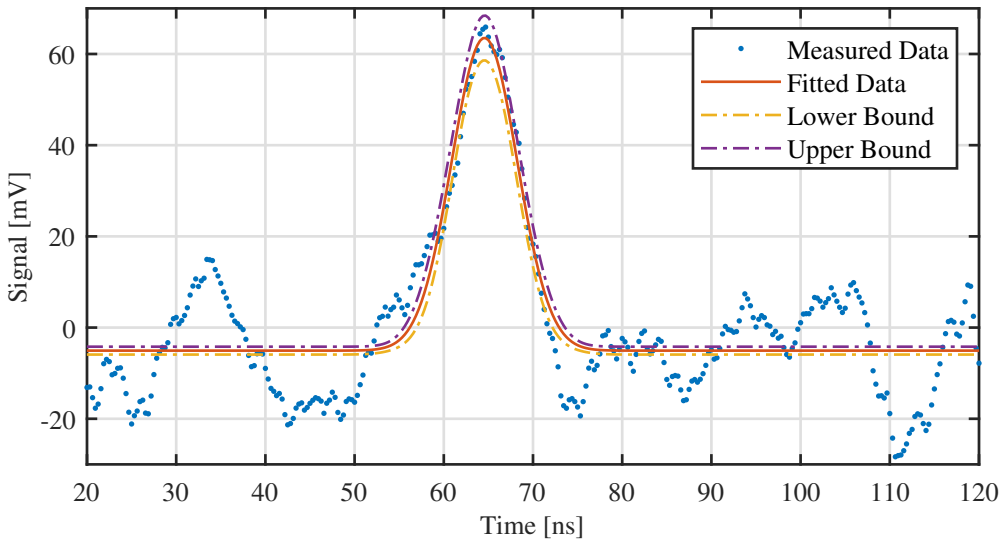

Figure 5.1: Raw data of a pulse digitized by the CAEN VX1743. The pulse is centered at 64 ns. Waveform is typical of a Thomson scattered signal. Results of the new pulse fitting routine used to analyze Thomson scattering signals are overlaid. The pulse fitting routine accepts the raw digitized data, plotted here as blue data points, as the input and returns a best fit, plotted here in orange. Also returned by the pulse fitting routine are the estimated one-sigma lower and upper error bounds of the fitted data, plotted as yellow and purple curves, respectively.

In Section 5.2, new polychromator electronics with a bandwidth of more than 60 MHz designed to be used with the CAEN VX1743 are presented. As shown in

Fig. 5.1, the combination of a high-speed digitizer and high-bandwidth polychromator electronics allows scattered pulses of only a few nanoseconds to be captured.

5.2 Polychromator Electronics

The primary goal of redesigning the HSX Thomson scattering polychromator electronics was to convert the pulsed avalanche photodiode (APD) current signal into a high-fidelity voltage signal that can be readily digitized. Discussed further in Section 5.3, a pulse fitting routine that fits data to a single Gaussian pulse has been implemented in the analysis routine for the HSX Thomson scattering system. Since the scattered signal has the temporal form of a Gaussian pulse, it is imperative to minimize temporal pulse shaping during the I-to-V conversion. In this context, pulse shaping refers to the increase in signal response times that occurs when a signal loses its high-frequency components, typically when processed by low-bandwidth electronics. According to Skolnik[52], capturing the primary high-frequency components of a simple Gaussian pulse requires that a detection system must have a frequency response with a minimum upper $-3dB$ point, or cutoff frequency, as defined by Eq. (5.1).

$$-3\ dB_{upper} \approx \frac{0.44}{T} \tag{5.1}$$

In Eq. (5.1), T is the full width at half maximum (FWHM) of the Gaussian pulse. For HSX, a typical beam pulse has an FWHM of 8 ns, so an effective detection system's minimum upper $-3dB$ point should be 55 MHz.

With the minimum system bandwidth constraint defined, secondary goals in designing new detection electronics were minimizing system noise and maximizing elec-

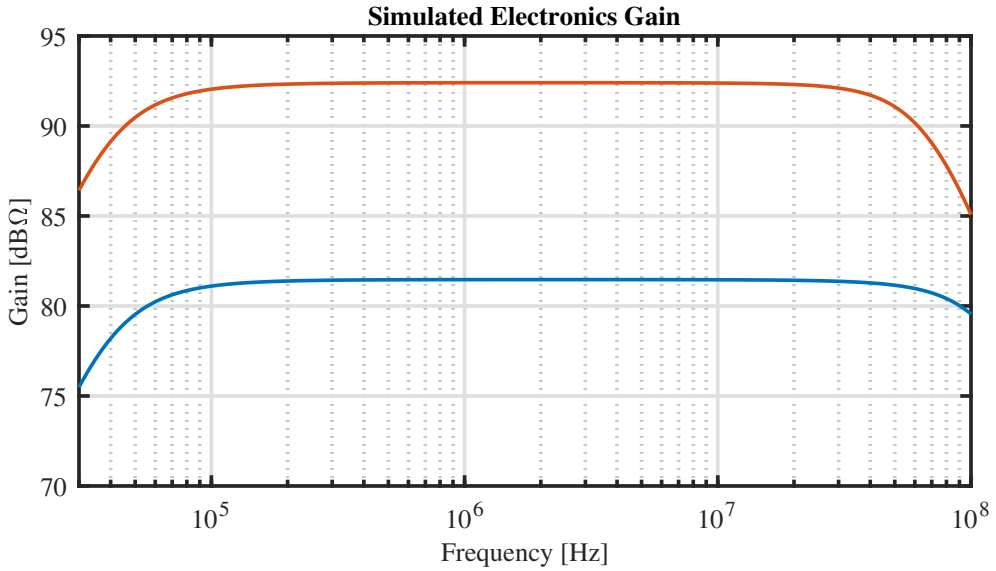

Figure 5.2: Frequency response analysis of the designed polychromator detection electronics performed in TINA-TI. The blue curve is the high gain configuration, and the orange curve shows the low gain configuration. Simulated upper $-3dB$ points are 67 and 118 MHz for the high and low gain configurations, respectively.

tronics gain. To accomplish the outlined design goals, a Texas Instruments (TI) OPA857 discrete transimpedance amplifier (TIA) was selected for the initial preamplifier stage in a signal chain similar to Fig. 39 in the OPA857 datasheet[53]. Device highlights of the OPA857 are ultra-low noise, 100 MHz operation, two user-selectable gain configurations, and an integrated voltage-to-current converter. The OPA857 voltage-to-current converter allows for frequency response characterization of the circuit without an APD, so the frequency response of the detection circuit can be analyzed with standard lab equipment. A TI THS4541 650 MHz GBW operational op-amp with a gain of 5 V/V was chosen as the output amplifier stage. In a typical Thomson scattering system, the signal removes the DC component of background light from Bremsstrahlung, and plasma noise is removed by using delay line

subtraction.

A consequence of using a delay line for subtracting the DC signal is doubling noise contributions, illustrated in Eq. (4.14) by the multiplier of two on the noise terms. Avoiding the pitfalls of delay line subtraction, AC coupling is performed on the newly designed electronics using a matched 50 Ω pulse transformer with a high-pass lower frequency cutoff of 300 kHz. Fig. 5.2. shows the frequency response characteristics

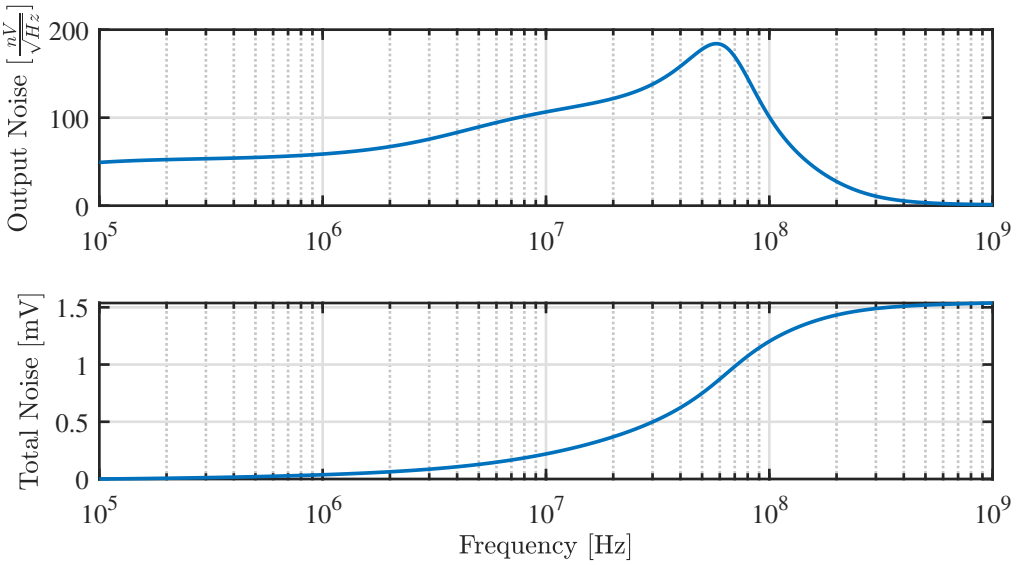

Figure 5.3: Noise analysis performed in TINA-TI for the high-gain mode of the newly designed polychromator electronics. (Top) Noise spectral content. (Bottom) Total noise as a function of frequency, converging at 1.5 mV_{RMS} of total simulated noise.

of the designed circuit, and Fig. 5.3 shows the results of a noise analysis as simulated in TINA-TI, a TI-supplied SPICE program[54]. The top plot of Fig. 5.3 presents the simulated output noise spectral density, and the bottom plot calculates the integrated, or total, noise for the system.

The upgraded Thomson polychromator PCB was designed, laid out, and populated in-house. Frequency response data for the new PCBs was measured and com-

pared to simulated results from TINA-TI and MATLAB to validate the design. The circuit's frequency response could be readily measured with an Agilent 8753ES S-Parameter Network Analyzer, owing to selecting a TIA with an integrated current-to-voltage converter. The measured frequency response data of the upgraded electronics is presented in Fig. 5.4. Noise level measurements were performed on the new CAEN

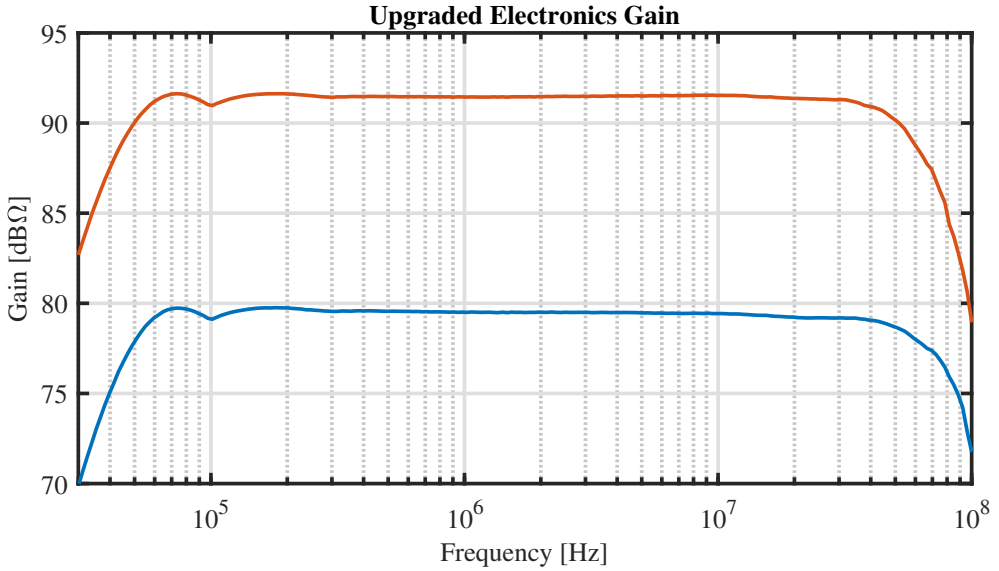

Figure 5.4: Measured gain frequency response of the newly designed polychromator electronics. The blue and orange curves are the high and low gain configurations, respectively. Measured upper $-3dB$ points are 61.5 and 78.4 MHz for the high and low gain configurations, respectively.

VX1743 digitizer running WaveCatcher[55] software. The WaveCatcher software includes a built-in noise measurement utility that measures the RMS value of noise, which can be directly compared to the total simulated noise from Fig. 5.3.

Measured and simulated results are compared in Table 5.1. Non-ideal discrete components and board layout can account for minor discrepancies between simulated and measured maximum gain values. The reduction in the measured system

Table 5.1: Comparison of simulated and measured HSX Thomson upgrade polychromator electronics results.

Gain	Gain_{sim}	Gain_{meas}	BW_{sim}	BW_{meas}	Noise_{sim}	Noise_{meas}
High	92.4 $dB\Omega$	91.5 $dB\Omega$	67 MHz	61.5 MHz	1.5 mV_{RMS}	5 mV_{RMS}
Low	81.5 $dB\Omega$	79.5 $dB\Omega$	118 MHz	78.4 MHz	0.6 mV_{RMS}	3.5 mV_{RMS}

BW relative to the simulated BW is likely due to excess input and parasitic capacitances on the PCB. Compared to simulated noise values, there is significantly more noise as measured in the realized system. Since the TI-TINA simulation does not include noise contributions from the physical implementation of the polychromator electronics, accounting for this difference between simulation and measurement is due to unsimulated noise sources. Unaccounted for in the simulation data is noise due to the polychromator enclosure, coaxial cable, and digitizer, so an increase in measured total noise from simulated values was expected. Fig. 5.5 shows the upgraded polychromator electronics output corresponding to a single Raman scattered pulse in an N_2 environment.

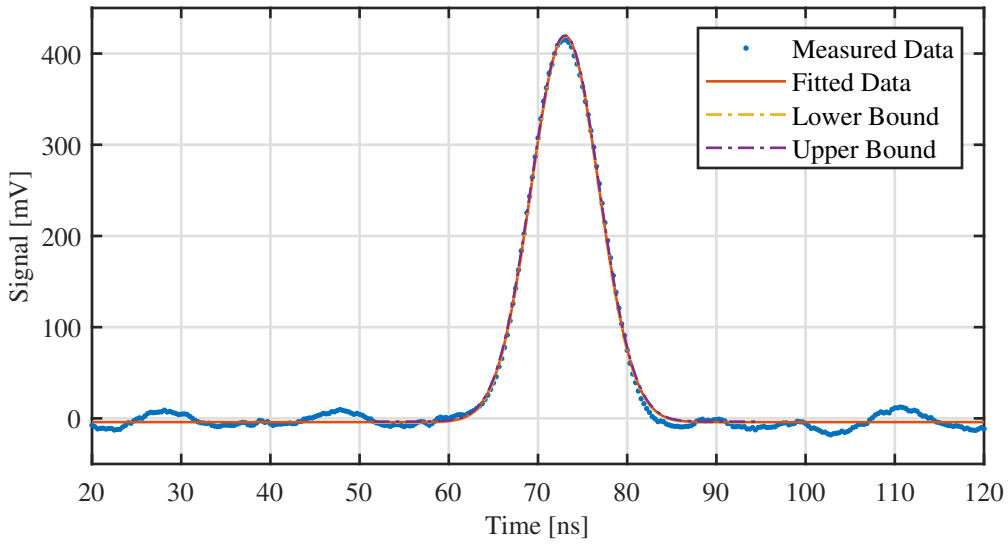

Figure 5.5: Measured response of the upgraded polychromator electronics, high-gain configuration, to a Raman scattered pulse (blue data points) and digitized by the CAEN VX1743 switched-capacitor digitizer. Overlaid is an example of a Gaussian fit to the scattered data (orange curve). Pulse was generated by spontaneous anti-Stokes Raman line emission stimulated by the interaction of the 0.75 J Thomson scattering laser with a 40 $Torr$ N_2 environment. System noise can be seen in the data outside of the pulse.

5.3 Signal Analysis

With the new CAEN VX1743 high-speed digitizer being used to capture Thomson scattering measurements, a new analysis routine for HSX was developed. In order to take advantage of the now time-resolved pulse measurements, a nonlinear least-squares algorithm was implemented to perform pulse fitting of the raw data and return the best fit with confidence intervals. For Thomson scattering signal analysis, it is desirable to integrate a fitted pulse instead of directly integrating the raw signal for two essential reasons. The primary reason to use a pulse fitted to the signal data is to mitigate background noise contributions[50] inherent in a plasma environment. The

HSX Thomson laser pulse timing can also drift up to 30 ns between discharges, so a digitizer that depends on temporal gating could potentially miss the entire signal pulse. The algorithm selected for analysis is a MATLAB[56] developed function $lsqcurvefit$[57]. The $lsqcurvefit$ function performs pulse fitting by solving for a set of coefficients, x, that minimize Eq. (5.2) and satisfy user-defined constraints.

$$\sum_i (F(x, xdata_i) - ydata_i)^2 \tag{5.2}$$

When applying pulse fitting techniques to Thomson scattered signals, it is common practice to fit a pulse that accounts for pulse shaping effects caused by detection electronics[50, 58]. When accounting for pulse shaping effects, the fitting function in Eq. (5.2) requires five or more fitting parameters in x. With the successful implementation of the detection electronics in Section 5.2, pulse shaping effects can be neglected, and the maximum number of fitting parameters needed for fitting a pulse signal on HSX is four, shown in Eq. (5.3).

$$F(x) = x_1 * exp\left[\frac{-(t - x_2)^2}{x_3^2}\right] + x_4 \tag{5.3}$$

In Eq. (5.3), x_1 is the pulse amplitude, x_2 is the temporal offset, x_3 is the pulse width, and x_4 is the DC offset. Even though the detection electronics are AC coupled, a slight DC offset is still possible at the digitizer, so it is essential to account for this parameter. When $lsqcurvefit$ has converged on the coefficient values that best fit the input data, it returns a Jacobian of the function using the values of x. The Jacobian can then be used to solve for the confidence intervals of the predicted values of x.

Fig. 5.5 shows a typical output from upgraded polychromator electronics overlaid

with a nonlinear least-squares curve fit. Prior to the arrival of the laser pulse, system noise of 10 mV_{RMS} is measured. The solid orange curve in Fig. 5.5 shows the results of a simple Gaussian pulse fitting routine applied to the measured signal. Since the pulse in Fig. 5.5 is a relatively easy pulse to fit with an S/N of 23.8 dB, the same pulse fitting routine can be applied to a pulsed signal with a much lower S/N of only 5.5 dB, see Fig. 5.1. Referring to the fitting results presented in Fig. 5.5 and Fig. 5.1, it is shown that high-bandwidth measurements coupled with pulse fitting techniques allow for the removal of noise and spurious signals from the signal.

5.4 Laser Power and Optical Setup Optimization

When the Thomson scattering system overhaul began, the Nd:YAG laser used as the Thomson scattering radiation source produced 320 mJ of pulse energy, 37.6% of the manufacturer-specified output power. As discussed in 3.1.1, the scattered power fraction of a Thomson scattering event is one the primary constraints on the diagnostic, so any loss in output energy is detrimental to the overall system performance. In 2021, a service technician repaired and refurbished the existing Litron TRL-850 Nd:YAG Thomson scattering laser. After being serviced, the laser output energy was increased to 725 mJ[59], a 127% increase in output energy, but still only 85.3% of the energy output when received from the manufacturer. Further focusing of the Nd:YAG laser was later performed to bring the total output laser energy to its current maximum level of 767 mJ, with a standard deviation of 1.67 mJ, another 8.9% increase in output energy.

After the laser output was restored, beam energy was measured at multiple points

along the beam path to evaluate energy loss along the beam path and identify possible improvement areas. Refer to Fig. 5.6 for a simplified layout diagram of the Thomson

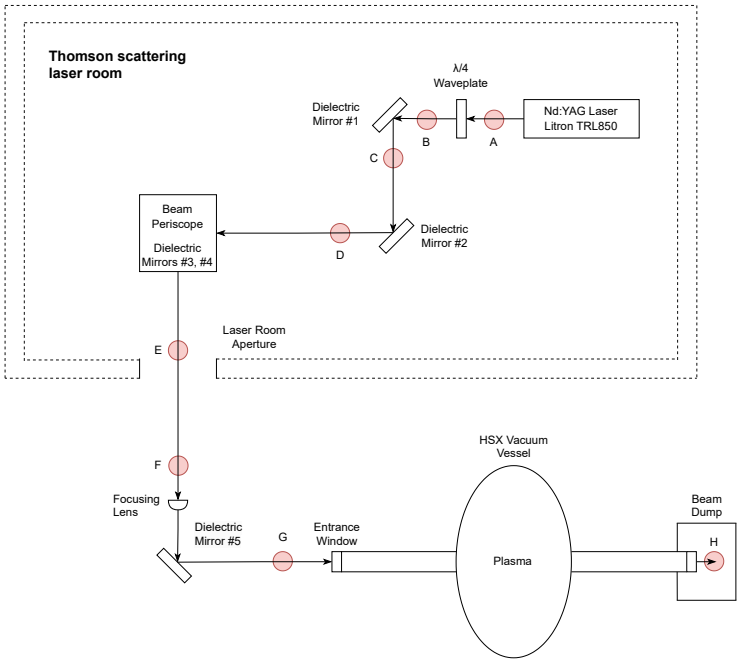

Figure 5.6: Diagram of the HSX Thomson scattering laser beam path before the beam path upgrades. Locations where beam energy measurements were collected are identified as red circles and are labeled A through H.

laser beam path. Energy measurements were made on a Coherent EnergyMax-USB J-50MB-YAG-1528 Energy Sensor with a calibrated measurement error of less than 1%. At each location in Fig. 5.6, labeled A through H, 20 full-power pulses were collected, and the measured data are presented in Table 5.2.

As shown in Table 5.2, the total loss along the beam path due to optical element interactions and diffraction losses is about 296 mJ, or nearly 42% of the initial output energy. According to the data in Table 5.2, two major contributing factors to energy lost along the beam path exist. The first source of loss is the number of optical

Table 5.2: Thomson scattering beam energy loss measured along the prior beam path, recorded on 2024-12-18. Accumulated losses from multiple optical element interactions, like those in locations B - D, are expected, but minimizing the number of optical elements in the beam path will help maximize total energy throughput. It is noteworthy that nearly 30% of beam energy is lost in the transit of the vacuum vessel, raising the possibility of poor beam alignment or obstructions in the vessel.

Location	Distance	Energy	Std. Dev.	Delta Loss	Cumulative Loss
A	10 cm	704 mJ	1.2 mJ	0 mJ / 0%	0 mJ / 0%
B	20 cm	687 mJ	1.4 mJ	17 mJ / 2.4%	17 mJ / 2.4%
C	35 cm	683 mJ	1.3 mJ	4 mJ / 0.6%	21 mJ / 3.0%
D	85 cm	661 mJ	1.3 mJ	22 mJ / 3.2%	43 mJ / 6.1%
E	345 cm	631 mJ	1.9 mJ	30 mJ / 4.5%	73 mJ / 10.4%
F	530 cm	601 mJ	2.0 mJ	30 mJ / 4.8%	103 mJ / 14.6%
G	680 cm	579 mJ	1.8 mJ	22 mJ / 3.7%	125 mJ / 17.8%
H	1050 cm	408 mJ	2.2 mJ	171 mJ / 29.5%	296 mJ / 42.0%

elements in the beam path. Parsing the loss data from Locations Table 5.2, almost 18% of beam energy is lost before even entering the vacuum vessel. While energy loss due to interactions with optical elements was measured as a relatively low 1-5%, the total loss quickly accumulates as the number of optical element interactions increases. In order to minimize beam energy loss prior to the vacuum vessel, the laser beam path was redesigned to be shorter and to reduce the total number of optical elements. This was accomplished by mounting the Thomson laser on a lifted platform that pointed directly out of the laser room, allowing for the removal of four dielectric mirrors from the beam path and an overall shortening of the beam path by 2 m. A diagram of the new beam path is presented in Fig. 5.7.

Energy measurements were again collected at the laser output and before the vacuum windows to test the efficacy of shortening the beam path. At this time, the laser had received a second round of maintenance, so the initial laser output energy was 767 mJ, and the energy at the vacuum window was 736 mJ, a loss of only 4%,

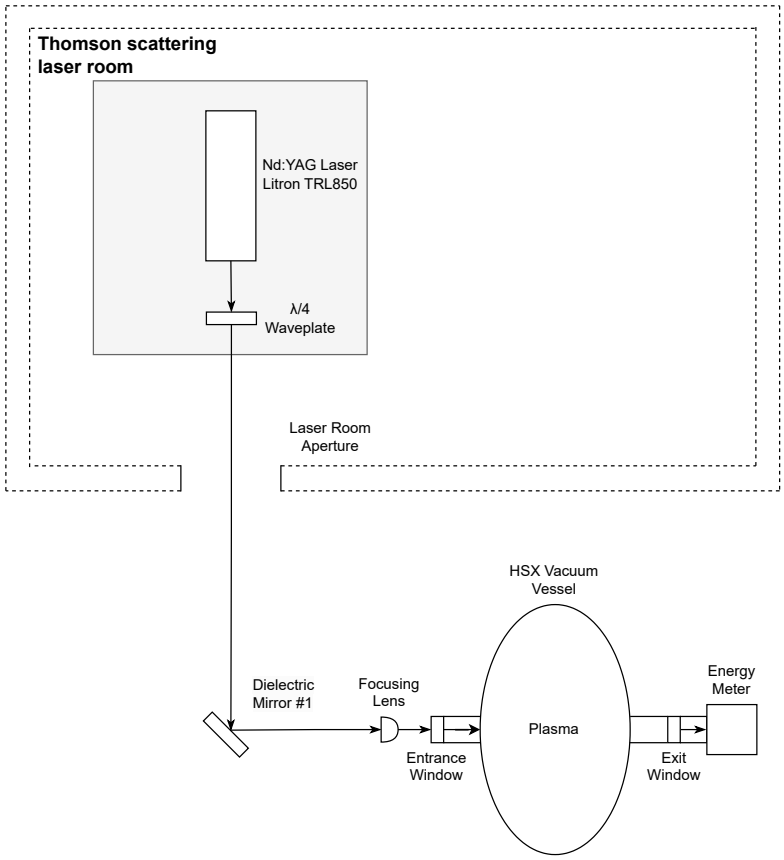

Figure 5.7: Diagram of the HSX Thomson scattering laser beam path after upgrades to the beam path. Four dielectric mirrors have been removed from the beam path, the focusing lens is 2 m closer to the vessel entrance window, and the beam path is 2.5 m shorter.

a significant reduction from the 17.8% loss from Table 5.2.

The second, much larger, beam energy loss occurred inside the vacuum vessel. Again, referring to Table 5.2, transiting the vacuum vessel resulted in a loss of 171 mJ, or 29.5% of the beam energy available at point G. Loss occurring inside the vessel is difficult to troubleshoot, but could be due to a handful of factors including poor beam tube alignment, structural vessel port misalignment, or losses due to the

poor transmission efficiencies of the entrance and exit windows.

Due to the large amount of beam power loss measured in the vacuum vessel, it was determined that the two 2 m long entrance and exit beam tubes should be removed. The original purpose of the beam tubes, as discussed in Section 3.1.2, was to reduce the amount of stray light that propagates into the vacuum vessel. However, all the filters used in the HSX polychromators have a blocking OD 6, so stray light should not be an issue in the current setup, so the beam tubes are extraneous.

It was also decided to replace the existing vacuum windows, BK7 elements set at the Brewster angle, with flat, standard one-inch vacuum windows. Historically, it has been difficult to properly align the HSX beam in the vessel, as the user must account for the oblong shape of the Brewster windows and the beam displacement caused by refractive effects. Theoretically, light incident on optical elements at Brewster's angle[10], defined as

$$\theta_B = atan(\frac{n_2}{n_1}), \tag{5.4}$$

where n_1 and n_2 are the refractive indexes of the initial and secondary medium, respectively, provide complete transmission of p-polarized light. In practice, surface imperfections can cause excess amounts of stray light for high-power lasers, even if complete transmission exists. In the case where the input beam is not perfectly p-polarized, Brewster windows available for 1064 nm beams can have coefficients of reflection greater than 20% for s-polarized light[60], which will cause any s-polarized light to be partially reflected into the vacuum vessel from the exit window. Newly developed Infrasil® textured windows available from Thorlabs, Inc[61] were used as the replacement entrance and exit windows. The Infrasil® windows have a nanostructured surface advertised as having superior spectral and mechanical properties.

Test data from Thorlabs shows that at 1064 nm, these windows have a damage threshold of 70 $\frac{J}{cm^2}$, a transmission of 99.6%, and reflectance of less than 0.06%. As these windows are new to the market, Thorlabs provided a set free of charge for evaluation[62].

Removing the beam tubes and replacing the vacuum windows significantly affected the beam energy lost along the laser beam bath. Energy measurements were again performed at the entrance and exit windows of the HSX vacuum vessel. The difference in output beam energy was measured by collecting 100 total energy pulses at the Thomson entrance and exit ports of the HSX vacuum vessel. Beam energy at the entrance window was measured to be 736 mJ, $\sigma = 1.59\ mJ$, and energy at the vessel exit window is now 714 mJ, $\sigma = 1.03\ mJ$, a loss of only 22 mJ, or just 3%.

In addition to collecting energy loss data, measurements of the beam waist within the vessel were desired. Quantifying the fraction of the probe beam being imaged onto the collection fiber is crucial, as it is determined by both the properties of the collection optics and the probe beam. Referring back to Eq. (3.1), the fraction of scattered power that is collected is directly proportional to $L * d\Omega_s$, which is the product of the probe beam cross-section, assuming $L_{beam} \geq d_{beam}$, within the collection optics solid angle, Ω_s. Eq. (3.1) assumes that the width of the probing beam is captured entirely within the spot size of the collection optics. If the input probe beam waist is large enough such that it is wider than the extent of Ω_s, then only a fraction of the Thomson scattered radiation will be able to be collected, reducing the number of total collected photons and increasing error as described in Section 4.1. Fortunately, historical alignment data provide enough information to determine the fraction of the beam that the collection optics can image. Beam alignment data from

2015 for Thomson spatial channel five is presented in Fig. 5.8. Measurements were

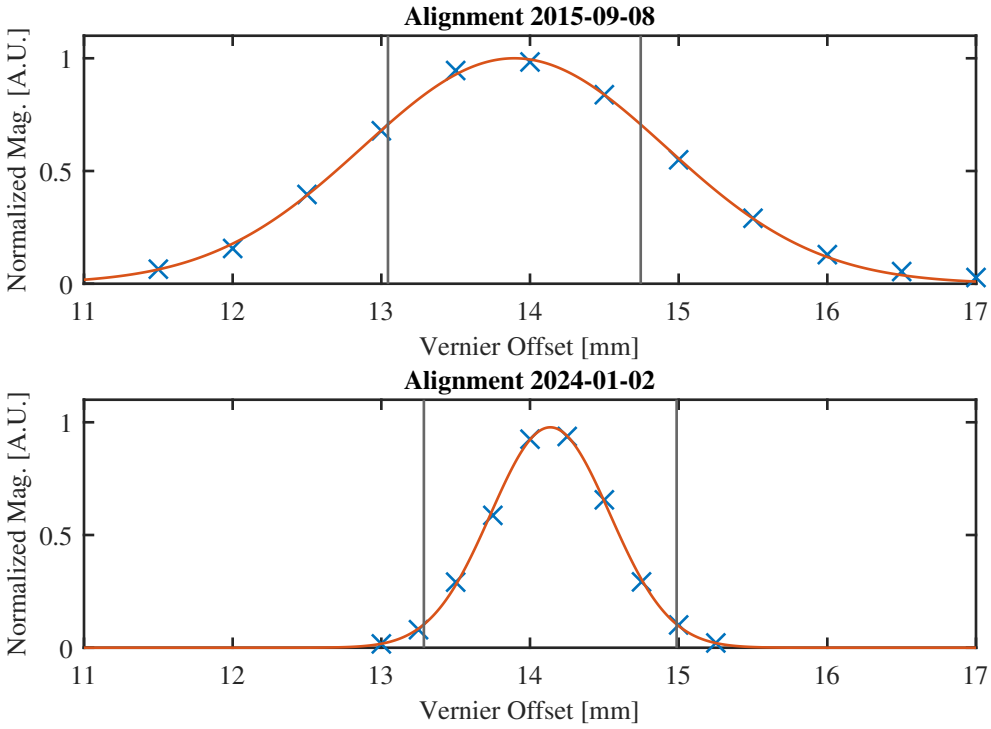

Figure 5.8: Beam alignment data from 2015-09-08 compared to data measured 2024-01-02. The measured data, blue markers, is normalized and fitted to a Gaussian orange line. The vertical black lines show the maximum imaged width of the beam onto the collection optics. Prior to any beam path adjustments, the maximum power collection limit was 59%. Improving the focus of the Thomson beam has increased the maximum power collection limit to 96%, an increase of 62.7% over the previous system.

performed by filling the HSX vessel with nitrogen gas, pulsing the Nd:YAG laser, and collecting the anti-Stokes Raman line emission[63, 64] at multiple lateral locations. Analysis shows that only 59% of the radiation in a Thomson scattering event could be collected, significantly reducing the scattered signal.

An additional benefit of removing the Thomson beam tubes and installing ultra-high energy damage threshold windows is that focusing elements with shorter focal

lengths can now be used. The use of the previous focusing lens, $f = 3\ m$, was necessitated by the existence of the 2 m beam tubes. The $f = 3\ m$ lens was replaced by a Thorlabs LA4716-1064, anti-reflective, $f = 0.75\ m$ lens, which will focus the Thomson beam waist to a smaller diameter and will minimize backscatter for light at 1064 nm. Following the installation of the new focusing lens, the beam waist was measured using the same method previously used, and the results are compared in Fig. 5.8. Using the same method to determine the maximum scattered energy that can be collected, the improved focus optics allow for 96% of scattered power, increasing the total signal by 53%.

As discussed in Section 4.2, Thomson scattering measurement uncertainty can be reduced by maximizing the number of photons collected by the diagnostic, effectively increasing the available signal to be measured. Aggregating the results from the upgrades mentioned above to the existing Thomson system, the total energy available for scattering events was increased upwards of 168%, more than doubling the expected S/N from an individual scattering event.

5.5 Simplified System Model

In Section 3.2, a χ^2 minimization algorithm, Eq. (3.4), that solves for the most likely electron temperature, T_e, and density, n_e, that correspond to a measured value, $N_{S_{pe,j}}$, was presented. $N_{S_{pe,j}}$ is the number of primary photoelectrons created in the detector by the collected scattered radiation and is defined as

$$N_{S_{pe,j}} = n_e \Omega_s L \frac{E_i \lambda_i}{hc} \int_{\epsilon_{j,1}}^{\epsilon_{j,2}} \frac{d^2\sigma_p}{d\Omega_s d\epsilon} T_{opt}(\epsilon) \eta(\epsilon) T_{filt,j}(\epsilon) d\epsilon. \tag{5.5}$$

Of course, we can not directly measure the number of photons in each scattering event, and the data obtained must be equated to an appropriate model for analysis. A new, simpler Thomson scattering diagnostic model focused on model parameters that can be directly quantified has been developed. Since $N_{S_{pe},j}$ can not be directly measured, it is useful to rewrite Eq. (5.5) in terms of the digitized signal, S, where $S_j = \int S_j(t)dt$ and is in the units of Volt-seconds.

Leveraging the fact that the number of primary photoelectrons collected, N_{pe}, is equivalent to the number of total scattered photons, N_p, convolved with the quantum efficiency of the detector[5], η, Eq. (5.5) can be rewritten as

$$N_{S_p,j} = n_e \Omega_s L \frac{E_i \lambda_i}{hc} \int_{\epsilon_{j,1}}^{\epsilon_{j,2}} \frac{d^2\sigma_p}{d\Omega_s d\epsilon} T_{opt}(\epsilon) T_{filt,j}(\epsilon) d\epsilon. \tag{5.6}$$

Converting the photons into their energy equivalent, $E_s = \dfrac{hc}{\lambda_s}$, where $\lambda_s = \lambda_i(1+\epsilon)$, we now have

$$E_{S_p,j} = n_e \Omega_s L E_i \int_{\epsilon_{j,1}}^{\epsilon_{j,2}} \frac{d^2\sigma_p}{d\Omega_s d\epsilon} T_{opt}(\epsilon) T_{filt,j}(\epsilon) \frac{d\epsilon}{1+\epsilon}. \tag{5.7}$$

Finally, multiplying the scattered energy by the system responsivity, $G_j[\Omega] * R_j(\lambda)[A/W]$, where G_j is the measured transimpedance gain of channel j, and R_j is the measured responsivity of channel j, we get the desired result for S_j in Eq. (5.8).

$$S_j = n_e \Omega_s L E_i G \int_{\epsilon_{j,1}}^{\epsilon_{j,2}} \frac{d^2\sigma_p}{d\Omega_s d\epsilon} T_{opt}(\epsilon) T_{filt,j}(\epsilon) R_j(\epsilon) \frac{d\epsilon}{1+\epsilon} \tag{5.8}$$

Now that we have the scattering model in a form easily related to the measured values, it will be useful to simplify Eq. (5.8) into a more compact form. The term $T_{opt}(\epsilon)$ refers to the transmission function of the fiber optics used in the Thomson scattering

diagnostic. Since the CeramOptec fibers in use on HSX, as described in Section 3.1.3, are ultra-low OH and have a flat transmission function for the wavelengths in use, the $T_{opt}(\epsilon)$ can be approximated as T_{opt} and pulled out of the integral in Eq. (5.8). Raman scattering, a calibration method described more in Section 5.6, can be used to simultaneously measure T_{opt}, Ω_s, and L, so all three terms can be combined into the geometry factor $C_{geo} = \Omega_s L T_{opt}$. Rewriting $\frac{d^2\sigma_p}{d\Omega_s d\epsilon}$ as $\nu(\epsilon)$ and combining $T_{filt,j}(\epsilon)$ and $R_j(\epsilon)$ into a total sensitivity term $RT(\epsilon)$, the measurement of which is discussed further in Section 5.6, Eq. (5.8) can be written as

$$S_j = n_e E_i C_{geo,j} G_j \int \nu(\epsilon) RT_j(\epsilon) \frac{d\epsilon}{1+\epsilon}, \tag{5.9}$$

where all terms are directly measured or calculated. E_i is the energy in the probe beam and is measured by a Coherent EnergyMax-USB J-50MB-YAG-1528 that samples every laser discharge. On HSX, C_{geo} is a geometry factor that is measured by Raman scattering[30, 63–66] and is a necessary calibration factor. G_j is simply the electronics transimpedance gain, which can easily be measured using common lab test equipment[48]. RT_j is the combination of a spectral channel's responsivity and the filter transmission function for that channel. RT_j can directly be measured by performing a spectral calibration. ϵ is wavelength shift from the probe beam wavelength, $\epsilon = \frac{\lambda_s - \lambda_i}{\lambda_i}$[8, 17, 27, 39]. The final two terms, n_e and $\nu(\epsilon)$, are the parameters being investigated. In summary, the system model in Eq. (5.9) solves for T_e and n_e and only requires three in situ calibrations and one additional measurement.

5.6 Improved Spectral Calibration

As discussed in Section 5.5, the $RT_j(\lambda)$ term in Eq. (5.9) requires measurement by way of spectral calibration. A diagram of a typical spectral calibration technique[67] is presented in Fig. 5.9. Using a monochromator with a broadband input light source, a

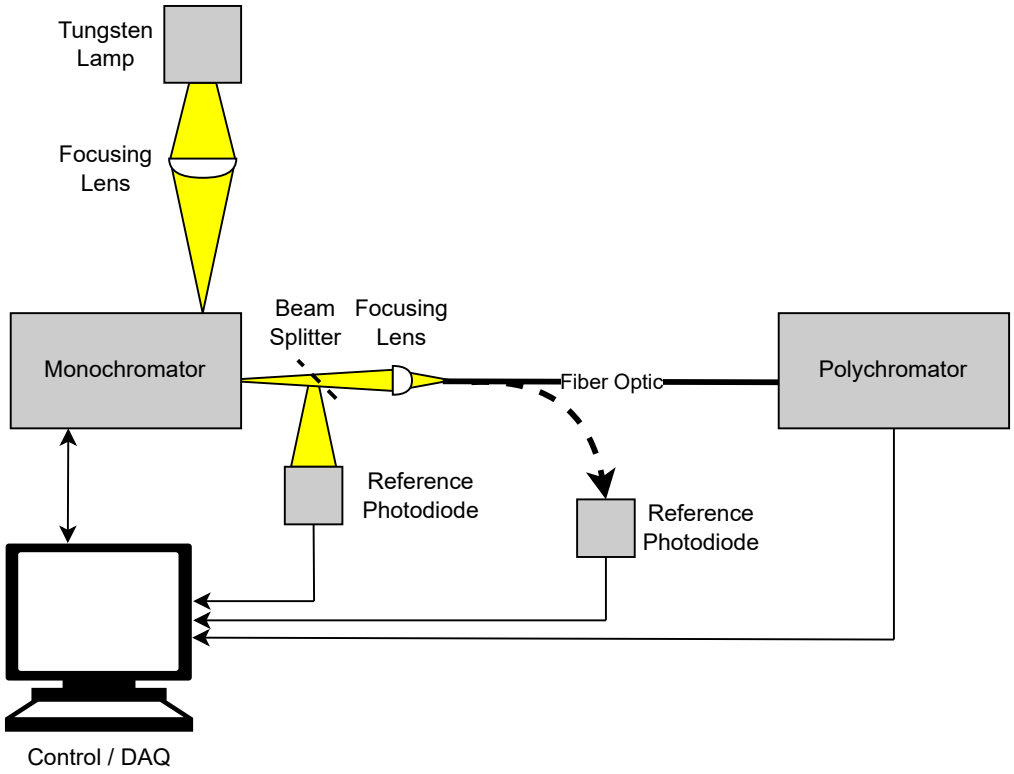

Figure 5.9: Diagram of HSX spectral calibration. The control PC advances the wavelength output and measures the photodiode and polychromator responses via the DAQ. The fiber optic used for calibration was a custom CeramOptec fiber with a 1 mm, single-fiber core.

control PC requests the output wavelength of the monochromator and scans through the designed wavelength range of the polychromator. Ideally, this spectral calibration technique allows for the measurement of $RT(\lambda)$ for each spectral channel. When per-

forming spectral calibration on polychromators, since the system fibers are generally inaccessible when installed on an experimental plasma vessel, it is common practice to use an auxiliary calibration fiber in place of the fibers that are used during operation[24, 67]. It was discovered that using a separate calibration fiber could lead to erroneous results that may overestimate the true system responsivity. For example, Fig. 5.10 presents responsivity results from performing a spectral calibration of Spatial Ch. 1 with a (a)calibration fiber and with the (b)system fiber optics. In (c), the difference in responsivity between the two methods for each spectral channel is calculated, showing that the results from the two different calibration methods disagree. While discrepancies between the two results are as high as 25%, the difference from channel to channel can not be conveniently quantified. If a common factor in channel responsivity existed, the losses could be offset with a few calibration coefficients, but that is not the case here.

Differences in fiber core size and the alignment of the polychromator optical path likely cause the discrepancy between these two calibration methods. Recalling Fig. 3.2 from Section 3.2, the polychromator is designed to collimate and relay the input light between each spectral channel. The effective diameter of the calibration fiber is 1 mm, and the collection optics fiber is 2.8 mm. Since the system fiber has a large diameter fiber core, it is much more sensitive to any misalignment in the polychromator relay path that will lead to light loss and a lower effective responsivity.

This effect can also be seen in the results of Raman calibrations that were carried out with the previous spectral calibration method and improved method, presented in Fig. 5.11. In Fig. 5.11, there is a discrepancy between Raman coefficients measured using old spectral calibration data, in blue, and those that used the improved spectral

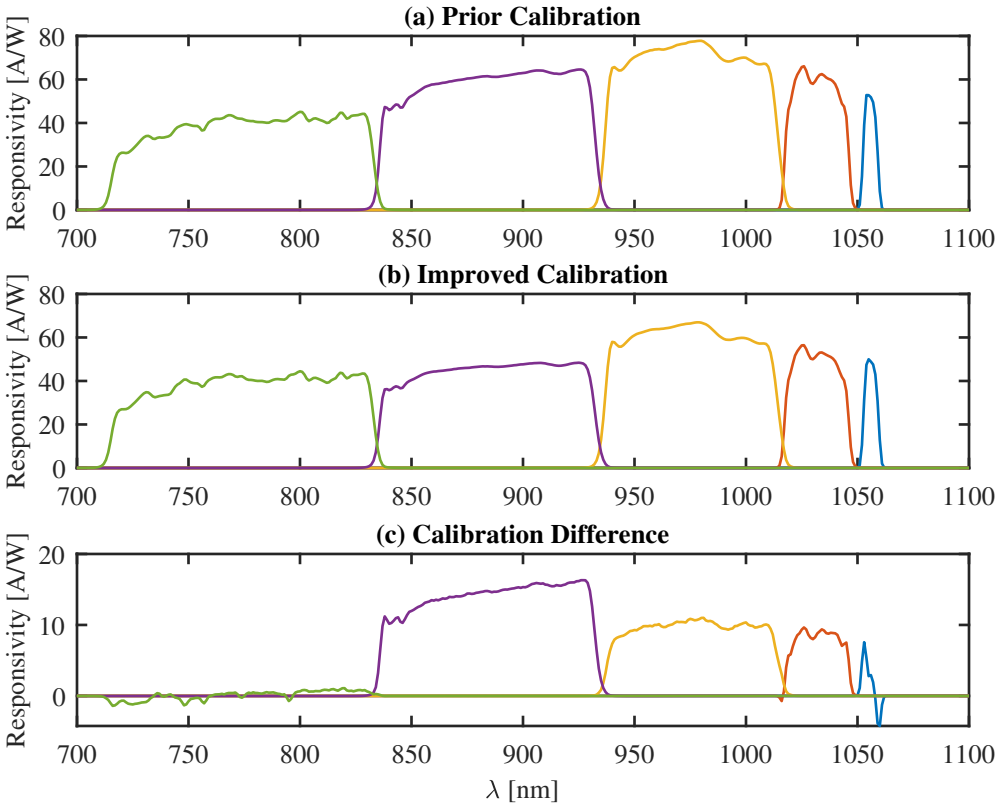

Figure 5.10: Difference in calibrated spectral responsivity on Spatial Ch. 1. (a) Spectral calibration results when using the prior calibration fiber. (b) Spectral calibration results when using the full in situ fiber. (c) The difference in responsivity between the two methods on each of the five spectral channels. The previous calibration method overestimated the responsivity of most spectral channels. This systematic overestimation is not linearly consistent between spectral channels, so a correction coefficient for the whole spatial channel is not feasible.

calibration technique, in orange. Using a qualitative argument, Raman coefficients can be described as a measure of the effective size of the scattering volume of each channel, so it is expected that the Raman coefficients would follow a smooth profile, much like that of the orange markers in Fig. 5.11.

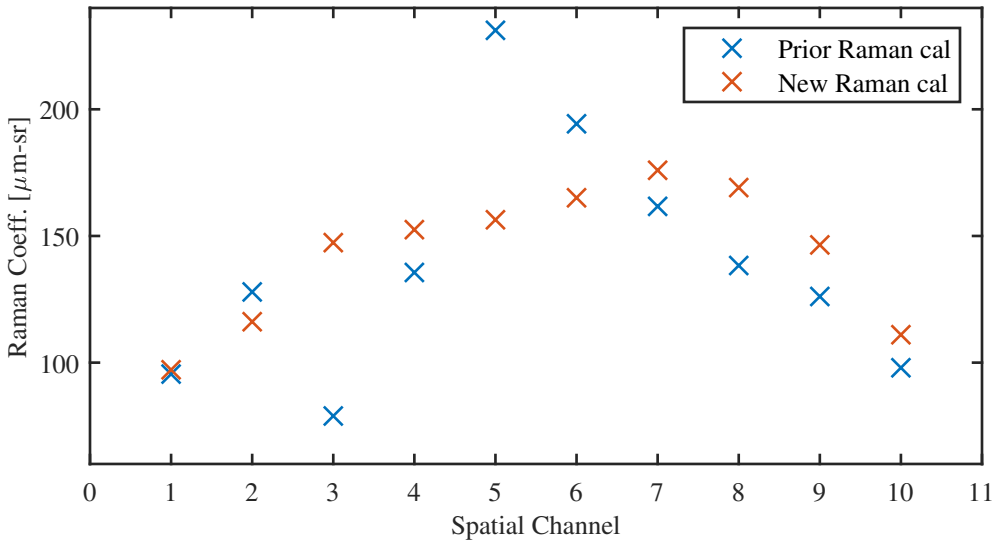

Figure 5.11: Comparison of Raman calibration coefficients measured with the old spectral calibration method (blue) to those measured after the implementation of the improved spectral calibration method (orange). Raman coefficients for a Thomson scattering system are a proxy for the scattering volume measured by each spatial channel.

5.7 Summary of System Improvements

Table 5.3 quantifies the improved system parameters on the HSX Thomson scattering diagnostic.

Table 5.3: Summary of notable results of systematic improvements to the HSX Thomson scattering diagnostic.

Category	Parameter	Prior Value	New Value
Detection Electronics	BW	6 MHz	78.4 MHz (Low Gain) 61.5 MHz (High Gain)
Detection Electronics	Noise	5 mV_{pk-pk}	<3.5 mV_{pk-pk} (Low) <10 mV_{pk-pk} (High)
Detection Electronics	DC Gain	74 $dB\Omega$	79.5 $dB\Omega$ (Low) 91.5 $dB\Omega$ (High)
Digitization	Sampling Rate	N/A	3.2 GSa/s
Laser	Output Beam Energy	725 mJ	767 mJ
Laser	Usable Beam Energy	408 mJ	714 mJ
Laser	Length of Beam Path	10.5 m	8.5 m
Collection Optics	Collected Power Fraction	59%	96%

Bibliography

[5]J. Sheffield, ed., *Plasma scattering of electromagnetic radiation: experiment, theory and computation*, 1st ed (Elsevier, Amsterdam ; Boston, 2011), 497 pp.

[8]S. L. Prunty, "A primer on the theory of thomson scattering for high-temperature fusion plasmas", Phys. Scr. **89**, Publisher: IOP Publishing, 128001 (2014).

[10]J. D. Jackson, *Classical electrodynamics*, 3rd ed (Wiley, New York, 1999), 808 pp.

[17]T. Matoba et al., "Analytical approximations in the theory of relativistic thomson scattering for high temperature fusion plasma", Jpn. J. Appl. Phys. **18**, Publisher: IOP Publishing, 1127 (1979).

[22]K. Zhai et al., "Performance of the thomson scattering diagnostic on helical symmetry experiment", Review of Scientific Instruments **75**, Publisher: American Institute of Physics, 3900–3902 (2004).

[24]L. Morton, "Turbulence and transport in magnetic islands in MST and DIII-d", PhD thesis (UW - Madison, Aug. 1, 2016), 171 pp.

[27]S. A. Bozhenkov et al., "The thomson scattering diagnostic at wendelstein 7-x and its performance in the first operation phase", J. Inst. **12**, P10004 (2017).

[30]I. Yamada et al., "Calibrations of the LHD thomson scattering system", Review of Scientific Instruments **87**, Publisher: American Institute of Physics, 11E531 (2016).

[31]J. H. Lee et al., "Research of fast DAQ system in KSTAR thomson scattering diagnostic", J. Inst. **12**, C12035 (2017).

[39]O. Naito et al., "How many wavelength channels do we need in thomson scattering diagnostics?", Review of Scientific Instruments **70**, Publisher: American Institute of Physics, 3780–3781 (1999).

[48]W. R. Goodman et al., "Upgrade of the helically symmetric experiment thomson scattering diagnostic suite", Review of Scientific Instruments **93**, Publisher: American Institute of Physics, 093518 (2022).

[49]R. O'Connell et al., "Optimizing a thomson scattering diagnostic for fast dynamics and high background", Review of Scientific Instruments **79**, Publisher: American Institute of Physics, 10E735 (2008).

[50]K. C. Hammond et al., "Initial operation and data processing on a system for real-time evaluation of thomson scattering signals on the large helical device", Review of Scientific Instruments **92**, Publisher: American Institute of Physics, 063523 (2021).

[51] *VX1743*, CAEN - Tools for Discovery, https://www.caen.it/products/vx1743/ (visited on 03/31/2024).

[52]M. I. Skolnik, ed., *Radar handbook*, McGraw-Hill handbook (McGraw-Hill, New York Düsseldorf, 1970), 1250 pp.

[53] *OPA857 data sheet, product information and support — TI.com*, https://www.ti.com/product/OPA857 (visited on 03/18/2023).

[54]DesignSoft, *TINA-TI*, version 9.3.200.277, Nov. 2022.

[55]CAEN S.p.A., *CAENWaveCatcher*, version V1.8.5, Dec. 14, 2022.

[56]The MathWorks Inc., *MATLAB version: 23.2.0.2409890 (r2023b) update 3*, Natick, Massachusetts, United States, 2023.

[57] *Solve nonlinear curve-fitting (data-fitting) problems in least-squares sense - MATLAB lsqcurvefit*, https://www.mathworks.com/help/optim/ug/lsqcurvefit.html#buun3a1-1 (visited on 04/01/2024).

[58]B. Kurzan et al., "Signal processing of thomson scattering data in a noisy environment in ASDEX upgrade", Plasma Phys. Control. Fusion **46**, 299 (2003).

[59]Tomaselli, Allen, *Laser service report - HSX*, Service Report (A.T. Laser Services, LLC, Aug. 25, 2021).

[60] *Brewster windows — EKSMA optics*, https://eksmaoptics.com/optical-components/polarizing-optics/brewster-windows/ (visited on 04/06/2024).

[61] *Infrasil® textured broadband antireflective windows*, https://www.thorlabs.com (visited on 04/06/2024).

[62]J. Williamson, *Thorlabs - contact me form for textured broadband antireflective windows. customer name: wayne goodman.* E-mail, Jan. 2, 2024.

[63]C. M. Penney, R. L. S. Peters, and M. Lapp, "Absolute rotational raman cross sections for n_2, o_2, and CO_2", J. Opt. Soc. Am., JOSA **64**, Publisher: Optica Publishing Group, 712–716 (1974).

[64]B. P. LeBlanc, "Thomson scattering density calibration by rayleigh and rotational raman scattering on NSTXa)", Review of Scientific Instruments **79**, 10E737 (2008).

[65]J. Howard, B. W. James, and W. I. B. Smith, "Rotational raman calibration of thomson scattering", J. Phys. D: Appl. Phys. **12**, 1435 (1979).

[66]I. Yamada et al., "Raman calibration of the LHD YAG thomson scattering for electron-density measurements", Review of Scientific Instruments **74**, 1675–1678 (2003).

[67]T. N. Carlstrom, *User manual: model GAPB-1064-4-1k*, Jan. 10, 1999.

Chapter 6

Filter Optimization and Spectral Multiplexing

6.1 Optical Filter Technology

Optical filters only allow a specified wavelength range of light to pass undisturbed while rejecting wavelengths of light outside the filter passband. Recent advances in manufacturing technologies have allowed for the economical production of optical filters with a high level of customization in transmission and rejection characteristics[68–70]. The most common types of optical filters on the market are the familiar high-pass, low-pass, and single-bandpass filters. In addition, more complex filters with multiple passbands or ultra-narrow passbands are becoming common and have a wide range of customization options.

Of interest to Thomson scattering applications that incorporate the filter polychromator configuration in Fig. 3.2 are interference filters. Interference filters contain

multiple layers of plasma-deposited dielectric materials with varying refractive indexes. Material composition and layering of the dielectric materials are strategically engineered to pass the desired spectral range while reflecting light outside the specified passband. Interference filters' ability to reflect a high percentage of light outside their designed passband is why they are commonly chosen for Thomson scattering applications.

6.2 Polychromator Filter Set Design

When designing a spectral filter set for incoherent scattering, the total number of spectral channels and their allocated passbands are determined by their ability to measure the scattered power spectra associated with the specified T_e range with minimal measurement error. Before an optimized filter set can be specified, the type and configuration of an optical system that will collect the scattered photons must be determined. The primary constraint on a scattering system is the limited scattered photon budget available during a measurement.

As described in Section 3.1.1, the number of collected photons during a TS event is so low that a filter polychromator performing a wavelength-integrated measurement must be used instead of a standard optical spectrometer. A polychromator mitigates the low signal issue by filtering the collected photons into wide wavelength bands from 5 to 150+ nm in width[37]. We use high throughput filters and convert the light to an electrical signal with avalanche photodiodes (APDs). The configuration of a filter polychromator, as designed by General Atomics, is shown in Fig. 3.2.

A standard error analysis can be utilized for a TS system with a filter polychro-

mator to determine the optimal passbands for a specified number of filters[39]. The number of collected photoelectrons in the j^{th} channel, $N_{S_{pe},j}$, from Eq. (4.4) is repeated here.

$$N_{S_{pe},j} = n_e \Omega_s L \frac{E_i \lambda_i}{hc} \int_{\epsilon_{j,1}}^{\epsilon_{j,2}} \frac{d^2\sigma_p}{d\Omega_s d\epsilon} T_{opt}(\epsilon)\eta(\epsilon)T_{filt,j}(\epsilon)d\epsilon$$

where n_e is the electron density, Ω_s is the collection solid angle, L is the scattering volume length, E_i is the total incident radiation energy, λ_i is the wavelength of the incident radiation, ϵ is the normalized wavelength shift, $\frac{d^2\sigma_p}{d\Omega_s d\epsilon}$ is the differential photon cross section per unit solid angle per unit wavelength shift from Eq. (2.49), $T_{opt}(\epsilon)$ is the total system transmission, and $\eta(\epsilon)$ is the quantum efficiency of the detector. $T_{filt,j}(\epsilon)$ is the filter transmission function on the j^{th} channel, the design variable used when designing a filter set.

Following the work of [46] and [13], the error in T_e and n_e for a standard filter polychromator is derived in Chapter 2. Eq. (4.9) and Eq. (4.10) are standard deviations in T_e and n_e, respectively, and are repeated below.

$$\sigma_{T_e}^2 = \frac{\sum(\frac{N_{S_{pe},j}}{\sigma_j})^2}{\sum(\frac{\partial N_{S_{pe},j}}{\partial T_e}\frac{1}{\sigma_j})^2 \sum(\frac{N_{S_{pe},j}}{\sigma_j})^2 - \left[\sum(\frac{\partial N_{S_{pe},j}}{\partial T_e}\frac{N_{S_{pe},j}}{\sigma_j^2})\right]^2}$$

$$\sigma_{n_e}^2 = \frac{ne\sum(\frac{\partial N_{S_{pe},j}}{\partial T_e}\frac{1}{\sigma_j})^2}{\sum(\frac{\partial N_{S_{pe},j}}{\partial T_e}\frac{1}{\sigma_j})^2 \sum(\frac{N_{S_{pe},j}}{\sigma_j})^2 - \left[\sum(\frac{\partial N_{S_{pe},j}}{\partial T_e}\frac{N_{S_{pe},j}}{\sigma_j^2})\right]^2}$$

where σ_j is the standard deviation of the collected photoelectrons in the j^{th} channel.

For a filter polychromator with M spectral channels, the optimal design is obtained by searching for a filter set, $T_{filt,j}(\epsilon)$, that minimizes

$$\delta_{err} \equiv (\frac{\sigma_{T_e}}{T_e}) \tag{6.1}$$

the relative error over the required range of T_e, 0.1 to 5 keV for HSX.

An optimized filter set will minimize the relative error by avoiding known noise sources in a plasma environment, specifically line radiation and Bremsstrahlung. Plasma line radiation directly contributes to the variance in the collected scattered photons, σ_j, thereby increasing the relative error δ_{err}.

Practical Constraints on Filter Design

Optimizing filter sets for a theoretical population of scattered photons may be the first-order step in TS filter design; however, more practical engineering constraints must be considered when designing a filter set. For example, budgetary constraints of government-funded research programs, fusion start-ups, and fusion demonstration facilities place strict limits on the overall cost of a TS diagnostic, which depends heavily on the per-channel cost of the system. Proper filter design must also consider manufacturer capabilities, which limit possible passbands, transmission/reflection efficiency, and the steepness of edge transitions.

Cost per digitized channel is a major limiting factor when designing a TS system. Budgetary restrictions can force the design engineer to make design concessions that reduce the number of spatial channels, decrease the measurable temperature range, or increase measurement error. A standard TS system can have well over 100 chan-

nels[49] requiring a spectral filter, optical lenses, a high-speed digitization channel, an APD, and processing electronics. Table 6.1 lists the required components for optical collection and analysis of a Thomson scattering system and their estimated cost. Due to economies of scale, the fewer unique filters in a filter set will lead to cost savings relative to a design with many unique filters; estimate ranges in Table 6.1 are meant to demonstrate the economies of scale effect. Referring to the data in Table 6.1, a TS diagnostic similar to that of HSX with 96 spectral channels has an estimated cost of $4k and $6k per spectral channel when not accounting for costs independent of channel quantity. An optimized TS filter set can quickly become prohibitively expensive, on the order of $500k or more, leading to engineering trade-offs that will generally reduce the measurement certainty of a given TS system.

Table 6.1: Cost estimation for the light collection components of a TS diagnostic with 96 total spectral channels. Estimated cost ranges are meant to reflect the quality of components available. The source of cost estimates is noted. Not included in this table are the costs associated with the input probe beam, initial collection optics, optical fibers, and required data infrastructure.

Component Name	Qty.	Est. Cost Ea.	Source
Custom Interference Filter	96	$250-1,000	Alluxa
Collimation and Focus Optics	120	$40-100	Edmund Optics
C30956EH APD	96	$800-1,000	Digi-Key
Preamp and Processing Electronics	96	$500-1,000	General Atomics
(A)8-bit, 32 Ch., 1 GS/s Digitizer	3	$96,000	Keysight[71]
(B)10-bit, 96 Ch., 1 GS/s Digitizer	1	$250,000	Teledyne[72]

Another critical design constraint stems from a significant drawback of the filter polychromator configuration, shown in Fig. 3.2. For example, suppose there are six spectral filters in the standard polychromator configuration that each has nearly

ideal reflection and transmission efficiencies of 95%. In that case, the signal power at the sixth spectral channel will be $P_{in} * 0.95^6$, just 73.5% of the original value. This reduction in signal strength will lead to increased measurement uncertainty and should be minimized whenever possible. It should also be noted that interference filters have a wide range of transmission efficiencies from 50-99%, so great care must be taken in designing, selecting, and calibrating them. This example shows that adding spectral channels will increase the overall T_e measurement range when designing filter sets for standard polychromators. However, the resulting per-channel signal reduction will increase errors in the downstream channels.

6.3 Filter Optimization

When optimizing Thomson scattering filter sets for low uncertainty, the best approach is to find a spectral filter function, $T_{filt,j}$ in Eq. (4.4), that minimizes Eq. (4.9). In addition to minimizing estimated error, ensuring that the solution for $T_{filt,j}$ can satisfy the required measurement range of T_e is vital. In this work, a controlled, elitist genetic algorithm[73] finds a Pareto front of $T_{filt,j}$ that both minimize the relative error in Eq. (4.9) and maximize the range of T_e that can be measured. A Pareto front is a set of solutions where no change in the parameters being optimized will improve one optimization goal without leaving another worse off. A controlled, elitist genetic algorithm is designed to reward diversity, allowing for a broad solution space of possible solutions treated with equal weight. This optimization approach ensures that elite solutions within a local minima of the solution space do not restrict the algorithm from exploring the rest. Optimization conditions and constraints used for

Table 6.2: Parameters for Eq. (4.4) used in the genetic algorithm optimization of $T_{filt,j}$.

Parameter	Symbol	Value	Units
Electron Density	n_e	3E18	m^{-3}
Scattering Length	L	1.5	cm
Solid Angle	Ω_s	0.01	Sr
Beam Energy	E_i	1	J
Beam Wavelength	λ_i	1064	nm
Fiber Transmission	T_{opt}	0.95	%
Norm. Wavelength	ϵ	-0.62:0.03	$unitless$
Temperature Range	T_e	0.01:40	keV
Scattering Angle	θ_s	$\frac{\pi}{2}$	$radians$
Laser Beam Waist	d_{laser}	1.7	mm
Laser Pulse FWHM	Δ_{laser}	6.25	ns
APD Noise Enh. Factor	F	2.4	$unitless$

Table 6.3: Constraints that were required to be satisfied during the optimization of $T_{filt,j}$.

Constraint	Symbol	Inequality	Lower Bound	Upper Bound
Relative Error	δT_e		0	10%
$T_{filt,j}$ Wavelength	$\lambda_{f,j}$		400 nm	1055 nm
No Filter Overlap	$\lambda_{f,j+1}$	$\lambda_{f,j+1} < \lambda_{f,j}$		

finding $T_{filt,j}$ in this work, unless otherwise noted, are listed in Tables 6.2 and 6.3.

Results from optimizing relative error, δT_e, and measurement bandwidth, ΔT_e, are presented in Fig. 6.1. As expected, when the number of total spectral channels, j, in $T_{filt,j}$ is increased, δT_e is reduced, and ΔT_e is increased. Fig. 6.2 presents examples of results from filter optimization and error analysis. Plotted at the top of Fig. 6.2 is an optimized five-channel filter set using optimization parameters from Table 6.2. The middle row plots the modeled photons collected as a function of temperature, and the relative error of this specific filter set is plotted in the bottom row. Optimization results like those presented in Fig. 6.2 aid in designing low-uncertainty filter sets for

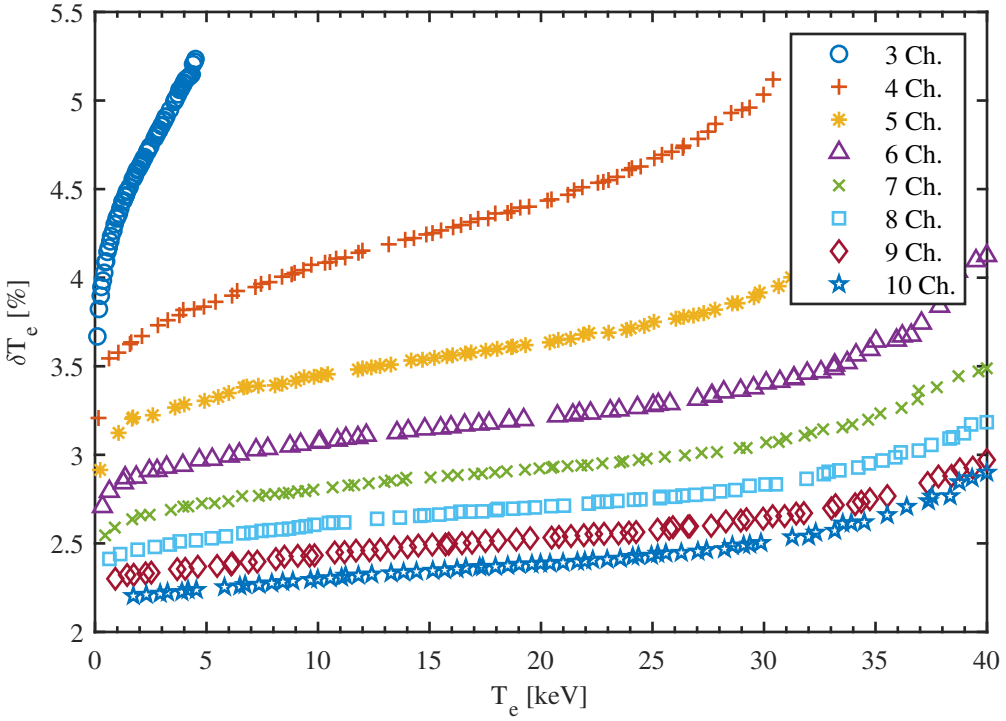

Figure 6.1: Pareto fronts for optimized standard Thomson scattering filter sets, $T_{filt,j}$. Results are plotted for filter sets of three to ten spectral channels.

use in Thomson scattering diagnostics.

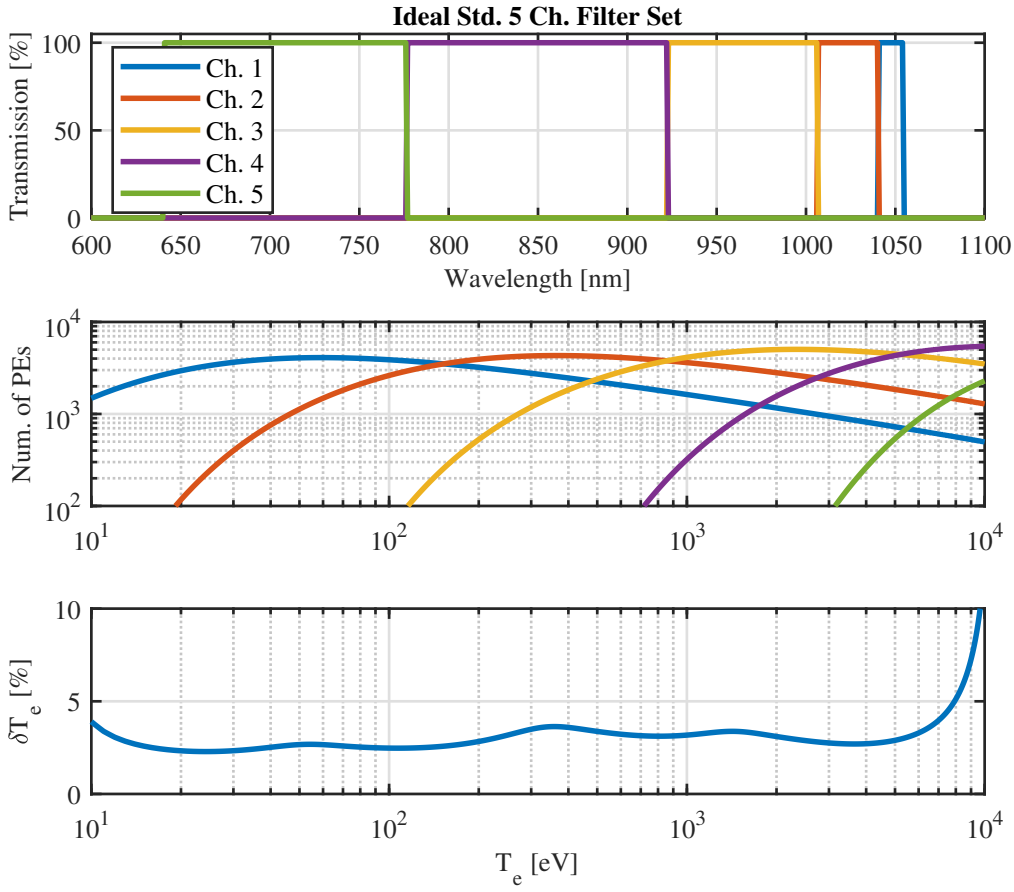

Figure 6.2: Filter optimization results for a standard five-channel filter set. (Top) The transmission function of the five spectral channels. (Middle) Number of photoelectrons per spectral channel as a function of T_e. (Bottom) Expected error for the ideal five-channel filter set.

6.4 Typical Thomson Scattering Filter Sets

Existing TS polychromator filter sets are designed so that each spectral channel has a single passband. See Fig. 6.3 for an example of a commercial bandpass filter transmission function. When considering optimization and implementation, it is easy to understand the benefits of a single-passband configuration. A computational routine

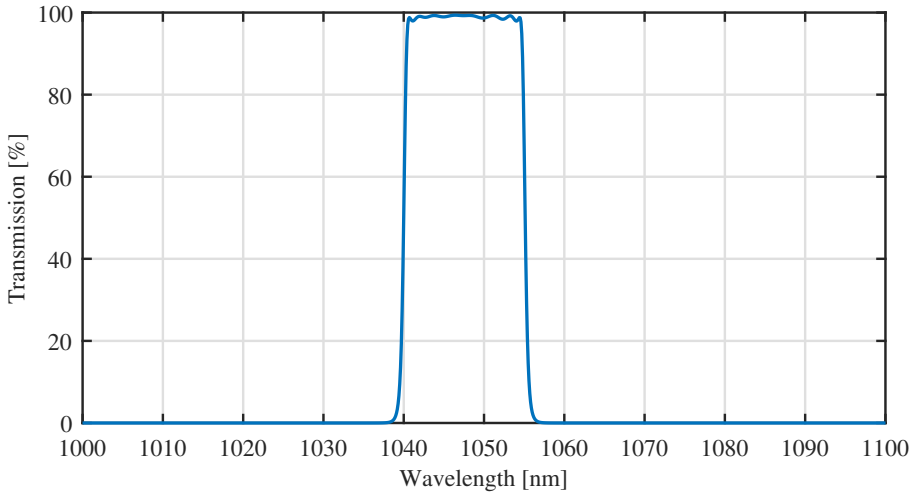

Figure 6.3: Transmission percentage as a function of wavelength for an example bandpass filter with a single passband. Filter data obtained from Alluxa for a 1047.5-15 OD4 Bandpass Filter[74].

written to optimize a single-band filter set will have minimal complexity, reducing required development and computation time. In addition, single-band filters have the inherent benefit of being relatively easy to manufacture; having a single passband requires minimal deposition engineering and fewer processing steps in manufacturing. Another common benefit of the single-band filter approach is that scattered spectral profile analysis looks straightforward as a first-order estimation. If one understands the scattered spectral profiles as a function of T_e, rough estimates of T_e can be made simply by comparing signal strengths between the spectral channels on a single polychromator by eye. A computer algorithm will typically be implemented to solve for T_e.

Although the single-band approach to analyzing scattered spectral profiles has the appeal of simplicity and ease of implementation, some major drawbacks should be considered. As discussed in Section 6.2, per channel cost and S/N characteristics

can adversely affect Thomson scattering filter set design. Another issue relating to the large number of spectral channels required comes in the form of channel underutilization. To describe channel underutilization, Fig. 6.4 presents an analysis of the

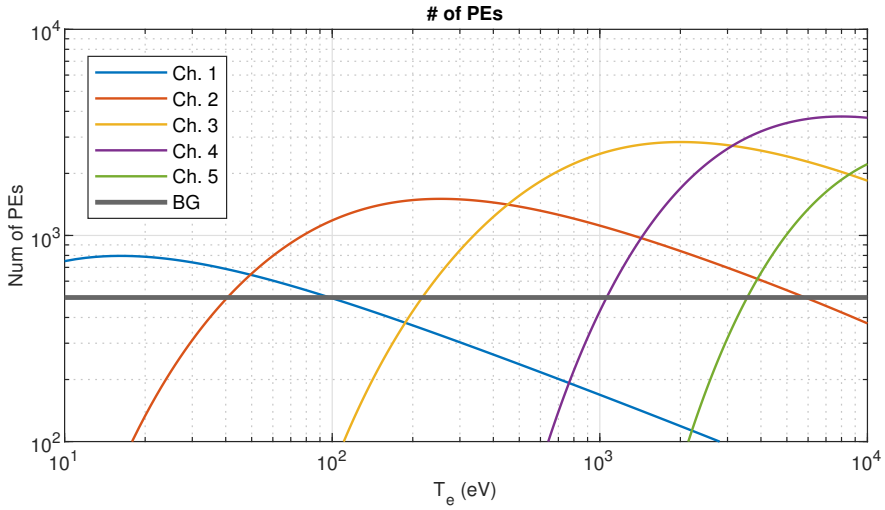

Figure 6.4: Number of photons collected as a function of T_e on the HSX 5-channel polychromator. The gray line labeled "BG" represents an example number of background photons from the plasma and can be considered the S/N = 1 limit for each channel. Analysis parameters are $n_e = 5 * 10^{18}\ m^{-3}$, $\theta = \frac{\pi}{2}$ radians.

number of collected photoelectrons as a function of T_e on the current HSX 5-channel polychromator. For this example, each spectral channel is assumed to collect 500 photoelectrons from background plasma radiation. This contribution is shown as the gray line labeled "BG" in Fig. 6.4. When the channel curves are below the gray line, this represents when the S/N of that channel is less than one and is therefore not contributing, at least beneficially, to the measurement of T_e. It can be seen in Fig. 6.4 that the useful measurement range of Channel 1 is only from $T_e \simeq$ 10 - 100 eV, whereas spectral channels 4 and 5 do not begin to contribute to the measurement until $T_e > 1\ keV$. Full control and characterization of the time evolution of a confined

plasma require the TS diagnostic to have the capability of measuring the full range of T_e that is achievable, which leads to the necessity of having underutilized spectral channels.

6.5 Spectral Multiplexing

In order to overcome the deficiencies associated with standard single-band polychromator filter sets, Thomson Scattering Spectral Multiplexing, or TSSM, is being developed as a novel technique to analyze spectral profiles of incoherently scattered radiation. TSSM takes advantage of advancements in optical filter technology to increase Thomson scattering measurement bandwidth, reduce δ_{err}, and reduce the required number of spectral channels. Instead of using a single bandpass filter for each spectral channel, TSSM requires filters that have multiple passbands, like that of Fig. 6.5.

Optimization of filters for a TSSM system proceeds much the same as that presented in Section 6.2; the filter designer must find a combination of filters that will minimize the error estimated in Eq. (4.9) and Eq. (4.10). A filter set optimization code was written in MATLAB for HSX-relevant plasmas, and results for a three-channel system, with and without TSSM, are presented below. Reducing the complexity of the optimization routine requires all filter sets to be assumed to have perfect transmission and reflection characteristics and brick-wall spectral cutoffs. Table 6.2 lists the parameters used in the optimization routine.

First, a three-channel polychromator without TSSM is optimized to minimize the average standard error from Eq. (6.1), where σ_{T_e} is defined in Eq. (4.9). Optimization

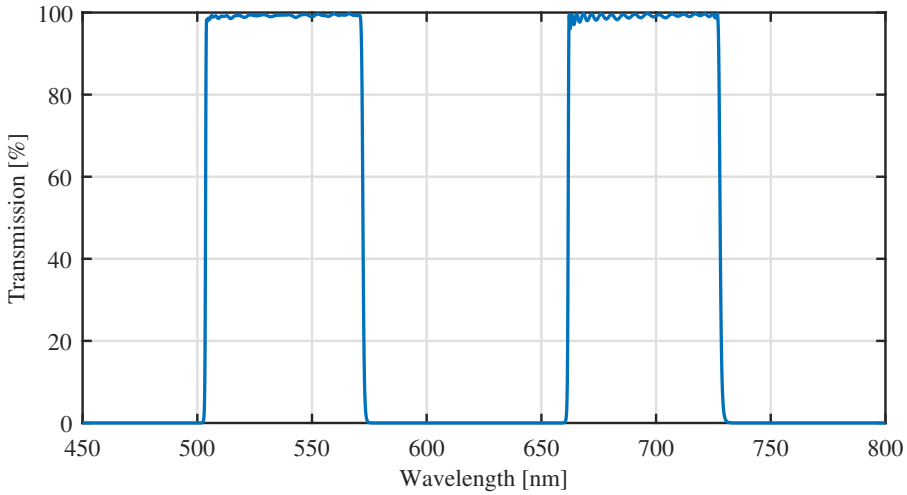

Figure 6.5: Transmission percentage as a function of wavelength for an example bandpass filter with a dual passband. Filter data obtained from Alluxa for a 538-69-695-67 OD6 ULTRA Dual-Bandpass Filter[75].

results for the three-channel, non-TSSM system are presented in Fig. 6.6, while the results for the TSSM-enabled system are shown in Fig. 6.7.

From inspection, it is clear that the filter set for the TSSM-enabled system in Fig. 6.7 has a significant advantage over the non-TSSM system in Fig. 6.6. The average error of the TSSM system is 48% lower than the non-TSSM system while having an acceptable T_e measurement bandwidth of 20 keV, 5.3x as large as the non-TSSM system. This drastic improvement can be attributed to the increased range in the error variable $\sum_j \frac{\partial N_{S_{pe},j}}{\partial T_e}$. From inspection of the "# of PEs" plots for both systems, it is clear that the increased activity and variation in the $N_{S_{pe},j}$ vs. T_e allow the system to resolve a broader range of T_e more accurately. This increase in measurement range can be explained by understanding that as $T_e \rightarrow 20$ keV, the scattered radiation peak will experience an increasing amount of blue-shift, never shifting back towards the longer wavelength end of the spectrum. Now, for the non-

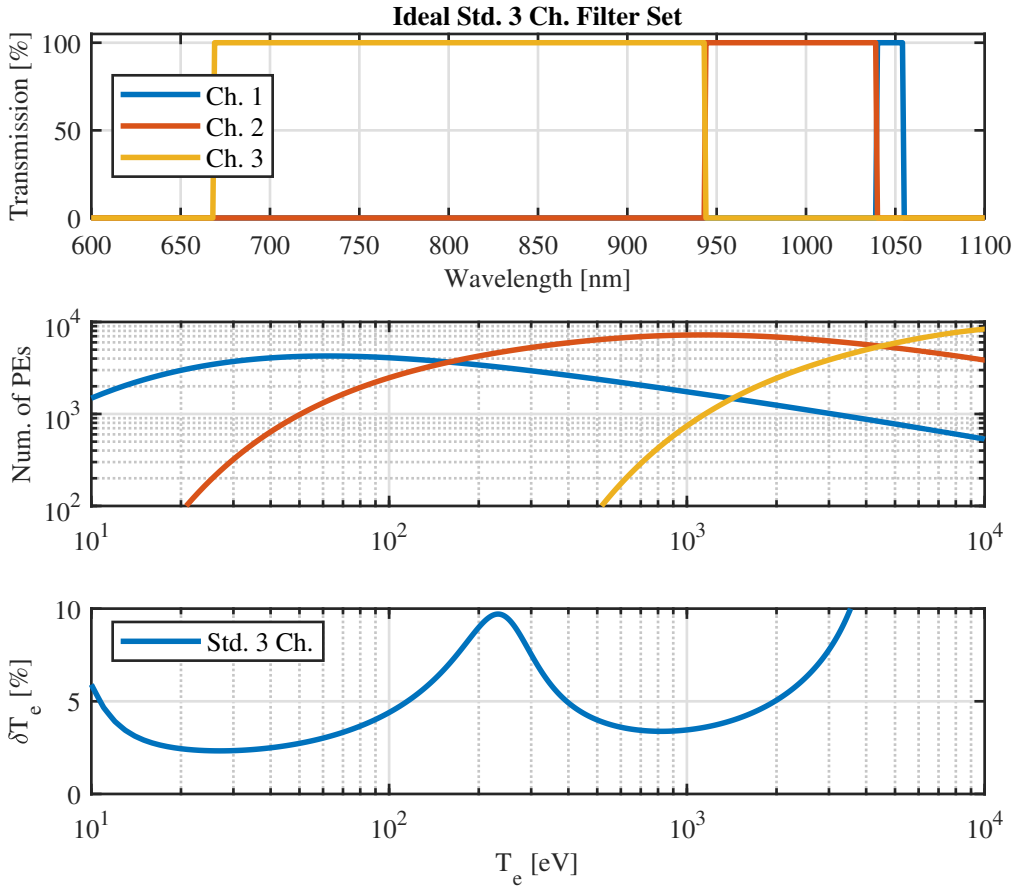

Figure 6.6: Filter optimization results for a three-channel polychromator without TSSM. Top: Optimized $T_{filt,j}(\epsilon)$, the filter transmission function for each spectral channel. Bottom-left: Number of photoelectrons measured as a function of T_e. Bottom-right: Standard error of each spectral channel as a function of T_e and the associated spectral bandwidth, defined as $\delta_{err} < 10\%$

TSSM system shown in Fig. 6.6, as $T_e \rightarrow 20\ keV$, each channel will only experience one peaking event; therefore there are only $n+1$ intensity ratios that can be accessed by the non-TSSM system, four in the case of the three-channel non-TSSM system. In contrast, since each spectral channel of the dual-band TSSM system experiences two intensity peaking events, there are now $n!$ intensity ratios available to resolve, or

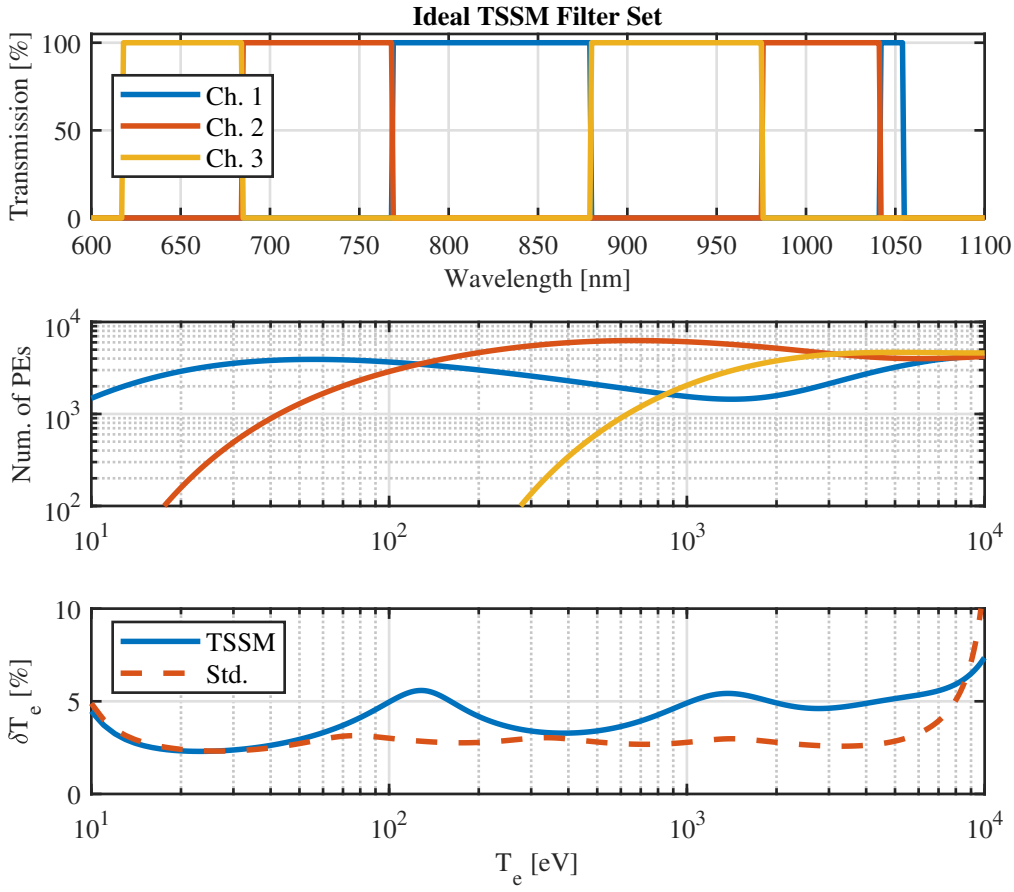

Figure 6.7: Filter optimization results for a three-channel polychromator with TSSM. This filter set was optimized for HSX and similar devices. (Top) The transmission function of the three TSSM spectral channels. (Middle) Number of photoelectrons per spectral channel as a function of T_e. (Bottom) Comparison of the expected error for the existing HSX 5-channel and the new TSSM filter sets.

six in the case of the dual-band TSSM system.

A comparison of optimized Pareto fronts of single-band filter sets and TSSM filter sets is presented in Fig. 6.8. Analysis of Fig. 6.8 shows that the TSSM method can increase the measurement range, ΔT_e, of a Thomson scattering diagnostic while reducing systematic error compared to standard single-band filter sets. Another benefit

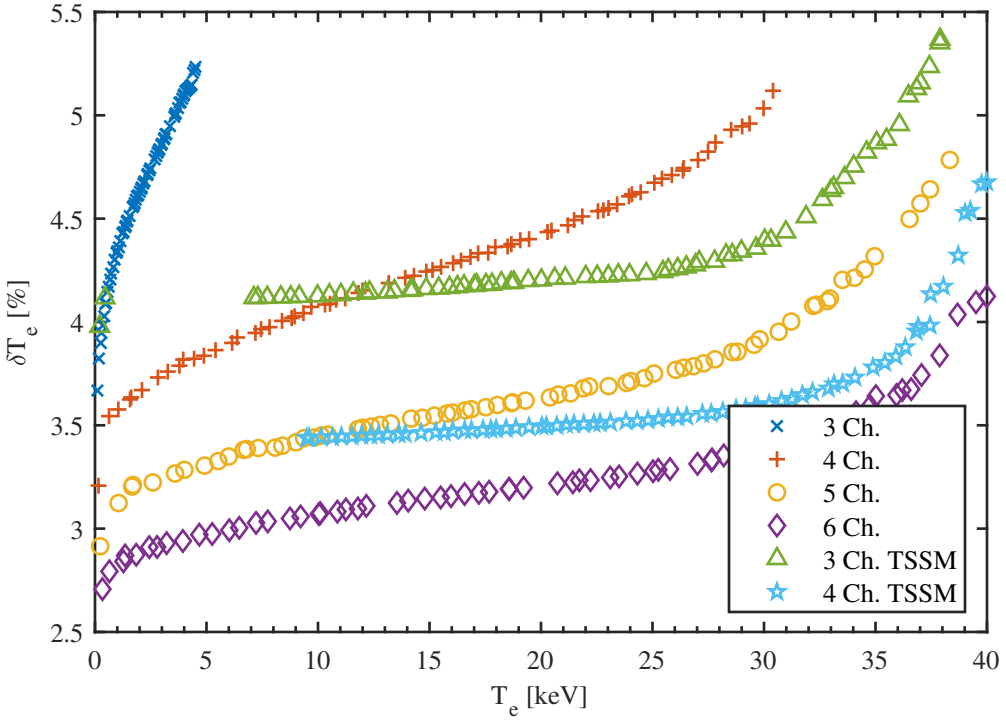

Figure 6.8: Comparison of Pareto fronts for optimized, single-passband filter sets, three to six spectral channels, to Pareto fronts for three and four-channel TSSM optimized filter sets. TSSM filter sets exhibit more stable, flat δT_e behavior over a larger range than single-passband filter sets. The three-channel TSSM filter set (green triangle) has a much wider measurement bandwidth in T_e than both the standard three (blue x) and four (red +) channel sets. At just over a 10 keV measurement range, the three-channel TSSM filter set can achieve a lower average relative error than the standard four-channel filter set. This suggests that, compared to standard Thomson scattering filter sets, the TSSM method can decrease measurement uncertainty and increase measurement bandwidth with fewer polychromator channels.

of the TSSM method is that the standard deviation of the relative error vs. temperature trace is reduced compared to the non-TSSM method. Section 6.6 presents a TSSM filter set optimized for use on HSX and the calibration results of the new filter sets.

6.6 HSX Spectrally Multiplexed Filter Sets

Optimization results for a TSSM filter set designed for HSX are shown in Fig. 6.7. Results from this optimization were used to compile a specification document for custom lenses. Alluxa, a custom filter manufacturer, could manufacture components meeting the specified filter set requirements, see Table 6.4. Manufacturer-supplied measurements of the filters shipped to HSX are included in Appendix A. Referring to Table 6.4, it was found that the 1045 nm to 1054 nm passband was out of specification, but the average transmission was measured as 94.5%, so just below the 95% threshold, and it was decided that this was acceptable.

Table 6.4: Transmission specifications for the optimized TSSM filter set to be tested on the HSX Thomson scattering diagnostic.

	Transmission	λ_{low} (nm)	λ_{high} (nm)	Req. Met?
Filter 1, Passband 1	>95%	858	968	Yes
Filter 1, Passband 2	>95%	1045	1054	No
Filter 2, Passband 1	>95%	819	857	Yes
Filter 2, Passband 2	>95%	1015	1044	Yes
Filter 3, Passband 1	>95%	600	818	Yes
Filter 3, Passband 2	>95%	968	1014	Yes

See Figs. 6.9 and 6.10 for the as-built measurement and error analysis for the two TSSM filter sets installed on HSX. Due to the lack of optical density, or OD, at 1064 nm on the TSSM filter set, see Fig. A.1, it was determined that notch filtering was required at the polychromator input. Off the shelf, 1064 nm notch filters that were purchased had an OD2 down to 1045 nm, explaining why a steep cutoff is seen in the TSSM filter sets plots. Also, the TSSM filter set spectral order on Spatial Channel 2, see Fig. 6.9, was altered to minimize error at higher temperatures. On HSX, spatial channel five is not expected to see T_e greater than 1 keV, so this filter

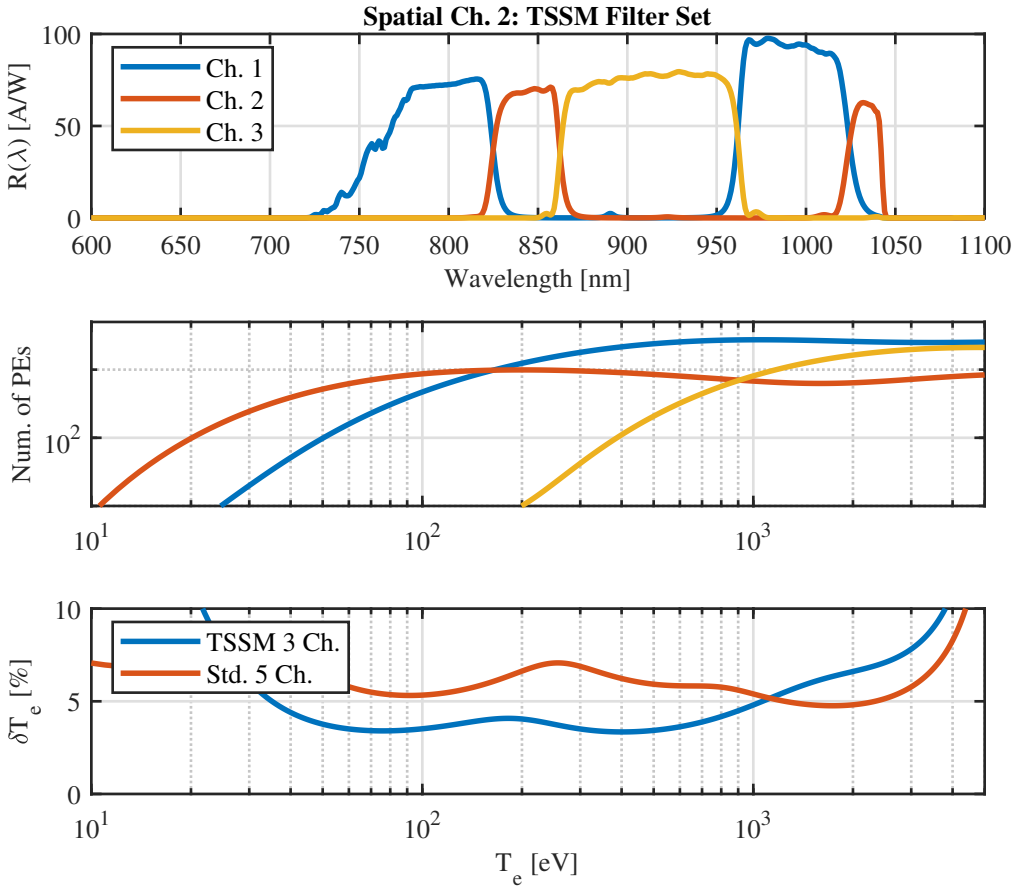

Figure 6.9: Error estimation of the as-built TSSM filter set on spatial channel 2 of the HSX Thomson scattering system. (Top) The calibrated responsivity of each spectral channel in units of $\frac{A}{W}$. (Middle) Number of photoelectrons collected in each spectral channel as a function of T_e. (Bottom) Calculated measurement error as a function of T_e for the TSSM three-channel filter set (blue) and the standard HSX five-channel filter set (orange). Analysis parameters: $E_i = 675\ mJ$, $\theta_s = 1.725\ rad$.

set was arranged to minimize error as lower values of T_e compared to the standard filter set.

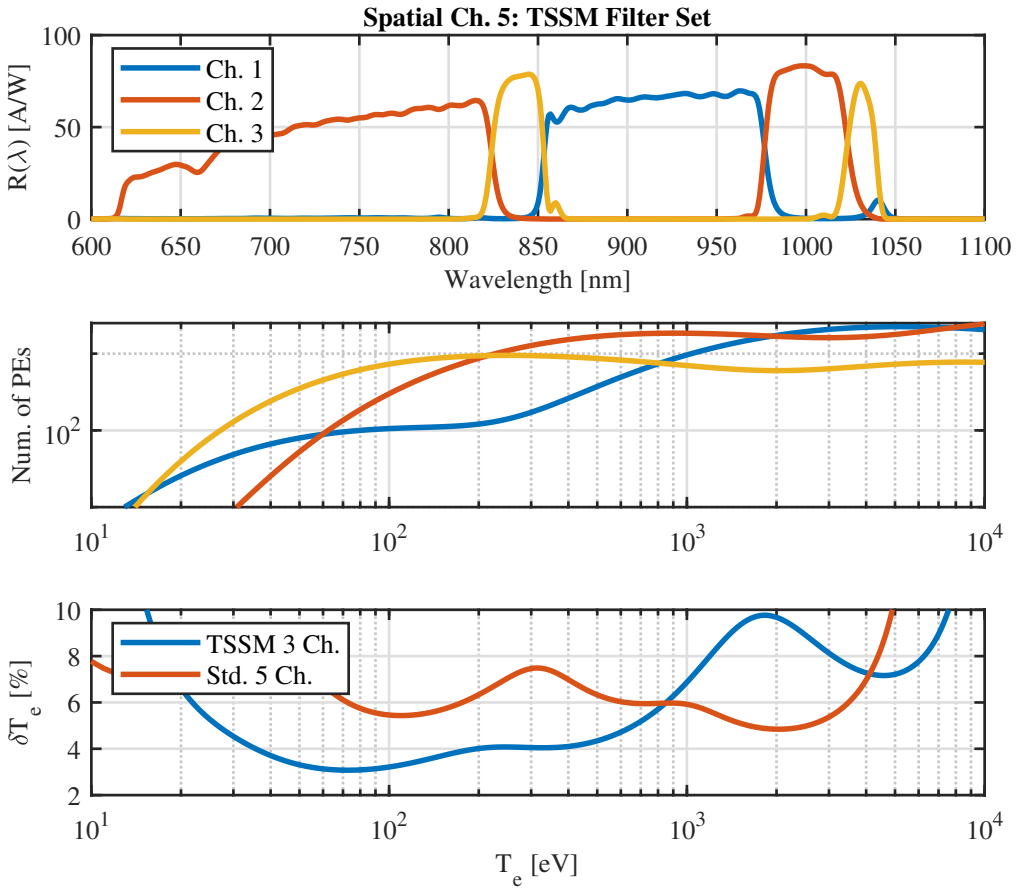

Figure 6.10: Error estimation of the as-built TSSM filter set on spatial channel 5 of the HSX Thomson scattering system. (Top) The calibrated responsivity of each spectral channel in units of $\frac{A}{W}$. (Middle) Number of photoelectrons collected in each spectral channel as a function of T_e. (Bottom) Calculated measurement error as a function of T_e for the TSSM three-channel filter set (blue) and the standard HSX five-channel filter set (orange). Analysis parameters: $E_i = 675\ mJ$, $\theta_s = 1.593\ rad$.

Bibliography

[13]G. S. Kurskiev et al., "A study of core thomson scattering measurements in ITER using a multi-laser approach", Nucl. Fusion **55**, Publisher: IOP Publishing, 053024 (2015).

[37]T. N. Carlstrom et al., "Design and operation of the multipulse thomson scattering diagnostic on DIII-d (invited)", Review of Scientific Instruments **63**, Publisher: American Institute of Physics, 4901–4906 (1992).

[39]O. Naito et al., "How many wavelength channels do we need in thomson scattering diagnostics?", Review of Scientific Instruments **70**, Publisher: American Institute of Physics, 3780–3781 (1999).

[46]P. R. Bevington and D. K. Robinson, *Data reduction and error analysis for the physical sciences*, 3rd ed (McGraw-Hill, Boston, 2003), 158 pp.

[49]R. O'Connell et al., "Optimizing a thomson scattering diagnostic for fast dynamics and high background", Review of Scientific Instruments **79**, Publisher: American Institute of Physics, 10E735 (2008).

[68]L. Martinu and D. Poitras, "Plasma deposition of optical films and coatings: a review", Journal of Vacuum Science & Technology A **18**, Publisher: American Vacuum Society, 2619–2645 (2000).

[69]R. R. Willey, "Estimating the number of layers required and other properties of blocker and dichroic optical thin films", Appl. Opt., AO **35**, Publisher: Optica Publishing Group, 4982–4986 (1996).

[70]M. Bass and O. S. of America, eds., *Handbook of optics*, 2nd ed (McGraw-Hill, New York, 1995), 4 pp.

[71]M. Larsen, *Keysight quotation 2328442-1*, Oct. 29, 2021.

[72]J. Sharp, *Teledyne quotation #11-211104-6-a*.

[73]D. Kalyanmoy, *Multi-objective optimization using evolutionary algorithms*, 1st ed. (John Wiley & Sons, Chichester, England, 2001).

[74] *1047.5-15 OD4 bandpass filter*, Alluxa Optical Filters and Thin-Film Coatings, https://www.alluxa.com/optical-filter-catalog/bandpass/single-band/1047-5-15-od4-bandpass-filter/ (visited on 03/18/2023).

[75] *538-69_695-67 OD6 ULTRA dual-bandpass filter*, Alluxa Optical Filters and Thin-Film Coatings, https://www.alluxa.com/optical-filter-catalog/bandpass/dual-band/538-69-695-67-od6-ultra-dual-bandpass-filter/ (visited on 03/18/2023).

Chapter 7

Results

Following the implementation of the system improvements outlined in Chapter 5 and the installation of two novel TSSM filter sets described in Chapter 6, Thomson scattering data has been collected on HSX. Section 7.1 compares post-upgrade Thomson scattering measurements to historical data obtained using the same filter sets. In order to directly compare these data, measurements performed on the two TSSM-enabled spectral channels are excluded from this analysis. Section 7.2 presents results from a comparative analysis of the TSSM method against the standard method of spectral filtering used in Thomson scattering diagnostics.

7.1 Results of HSX Thomson Scattering Diagnostic Systematic Improvements

The Thomson scattering system on HSX has demonstrated significant improvements in performance following the work outlined in Chapter 5. Shown in Fig. 7.1 is a

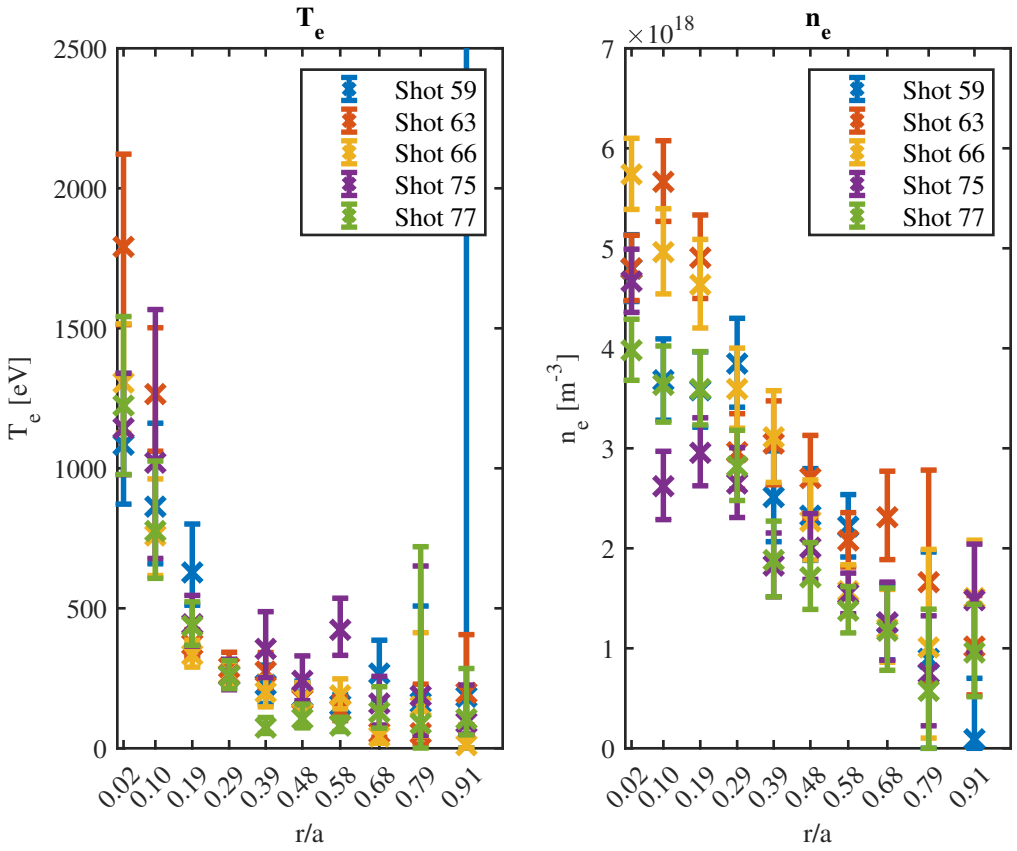

Figure 7.1: Profiles of T_e and n_e profiles before the HSX Thomson scattering upgrade. Data is from 2017-06-27 with operating parameters: 1 Tesla, QHS configuration, 50 kW heating, and helium fuel.

selection of five T_e and n_e profiles measured in HSX before the Thomson scattering diagnostic upgrade. These data were collected on 2017-06-27 during helium plasma discharges in the 1 T, QHS configuration of HSX. Specifically, the five profiles plotted in Fig. 7.1 were chosen as they had the least measurement uncertainty of an initial subset of twenty profiles.

For comparison, five T_e and n_e profiles measured in HSX after the Thomson scattering upgrade are plotted in Fig. 7.2. When comparing old and new HSX data,

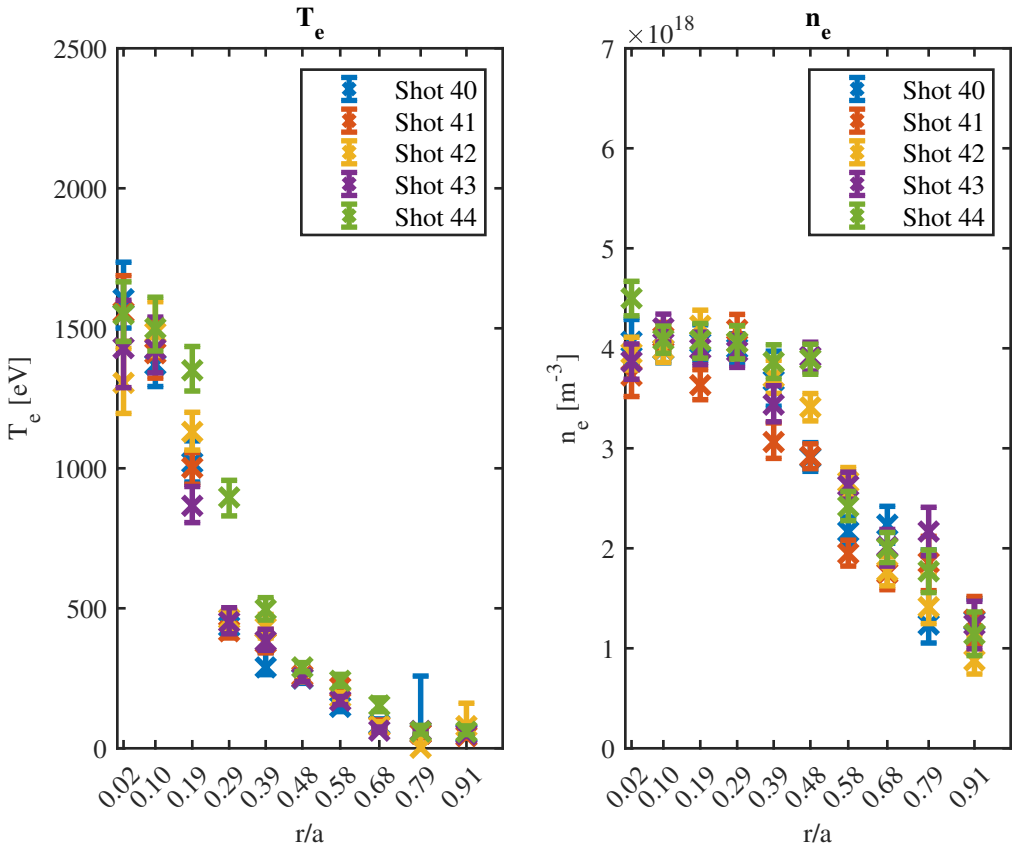

Figure 7.2: Profiles of T_e and n_e profiles after the HSX Thomson scattering upgrade. Data is from 2024-03-29 with operating parameters: 1 Tesla, QHS configuration, 50 kW heating, and helium fuel.

it is notable that both the T_e and n_e profiles exhibit different characteristic shapes. Comparing T_e data from Fig. 7.1 to that of Fig. 7.2, the pre-upgrade electron temperature profile peaks more in the core with a minimal temperature gradient from $\frac{r}{a} \geq 0.19$, whereas the new data have a steeper temperature gradient over a broader range of the plasma. Similarly, post-upgrade data for n_e in Fig. 7.2 show a much more pronounced electron density gradient in the edge channels, $\frac{r}{a} \geq 0.48$. The differences apparent between pre- and post-upgrade profile data are likely due to a

Table 7.1: Exclusion criteria implemented in the historical HSX Thomson scattering data analysis and how many data points were excluded. A total of 11,537 data points were excluded from the analysis. Note: Some data points satisfied multiple criteria.

Exclusion Criteria	Number excluded
$\delta T_e, \delta n_e \geq 100\%$	8,726
$T_e, n_e \leq 0$	695
$\delta T_e, \delta n_e$ undefined	2,494

combination of two factors. First, since the pre-upgrade data was collected, the HSX vessel walls were thoroughly stripped and cleaned, removing sources of impurities that harmed the performance of pre-upgrade plasmas. The second factor arises from the recently discovered alignment and calibration issues discussed in Section 5.6. Since measurements of the in-situ, pre-upgrade misalignment could not be performed, it has not been easy to quantify the effect of the misalignment on HSX data accurately throughout the years.

Another essential difference between pre-upgrade and post-upgrade datasets is the evident reduction in uncertainty for both T_e and n_e. The upgrades discussed in Section 5.4 increased the overall signal level 168%, which, assuming the signal increase is independent of additional noise, equates to an increase in system $\frac{S}{N}$ of 8.56 dB. Since the value of n_e is solely dependent on the total number of photons received, the reduced uncertainty in the post-upgrade n_e data in Fig. 7.2 is primarily due to the increase in total $\frac{S}{N}$. As discussed in Section 4.2 and shown in Eq. (4.9), measurement of T_e will also have reduced uncertainty when system $\frac{S}{N}$ is increased, but other factors can decrease δT_e even further.

In order to quantify the overall effect of the HSX Thomson scattering improvements outlined in Chapter 5, recent Thomson scattering measurements were compared

to available HSX Thomson scattering data collected before the upgrade. Using an automated script designed to crawl through all data currently stored on the HSX file system, from early 2014, Thomson scattering measurement data was extracted and analyzed. This data crawler generated a database containing 78,630 individual Thomson scattering measurements from 7,863 plasma discharges performed before the upgrade. It is essential to ensure the analysis of pre-upgrade Thomson data is not biased by outlier data or that the data is reliable and uncorrupted; therefore, measurements from the pre-upgrade Thomson database that satisfied the exclusion criteria listed in Table 7.1 were excluded from this analysis. The criteria in Table 7.1 cover cases where the analysis routine returns non-physical values for T_e or n_e, such as anything negative. Also covered by the criteria are cases where the analysis

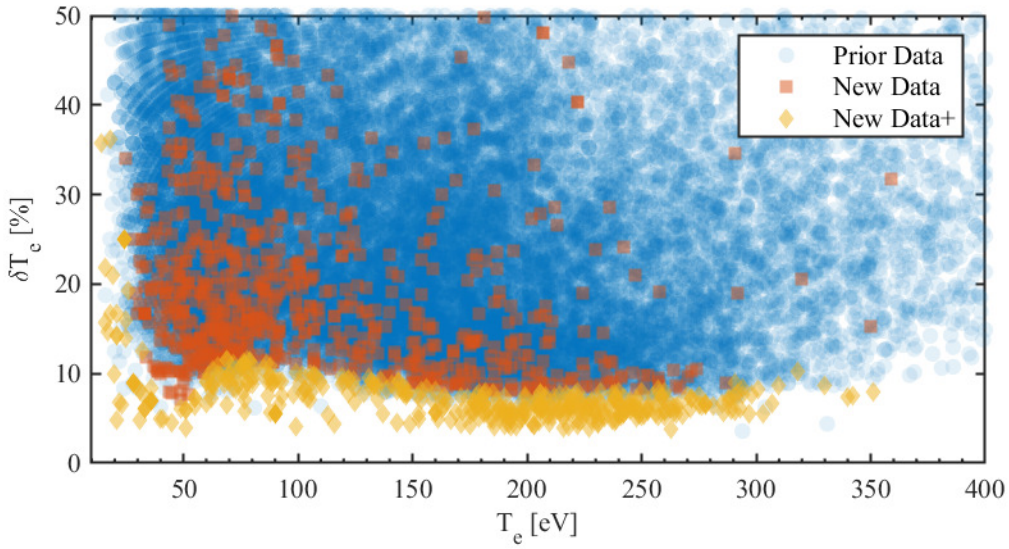

Figure 7.3: Comparison of all three-channel T_e data collected on HSX since 2014. Historical data, 28,609 individual data points, is plotted in blue circles. Data collected after the system upgrade, 1,201 data points, is plotted in orange squares/gold diamonds. Gold diamonds signify measurement uncertainty lower than the pre-upgrade system could achieve.

routine could not converge on a value for T_e, n_e or for $\delta T_e, \delta n_e$. Applying the rules from Table 7.1 resulted in the exclusion of 11,537 data points and a remaining data set of 67,093 data points.

Since HSX has two polychromator configurations with distinctly different error characteristics, see Appendix B, separate comparisons were performed for the three and five-channel polychromators. In order to ensure differences in the data are due to the systematic upgrades from Chapter 5, data collected with the new TSSM filter sets was excluded from this analysis and is discussed in Section 7.2.

A scatter plot of $\delta T_e(T_e)$ for 28,609 historical (blue circles) and 1,201 post-upgrade (orange squareslash gold diamonds) measurements is presented in Fig. 7.3. For the temperature range of 10 to 400 eV on the three-channel polychromators, 36.6% of

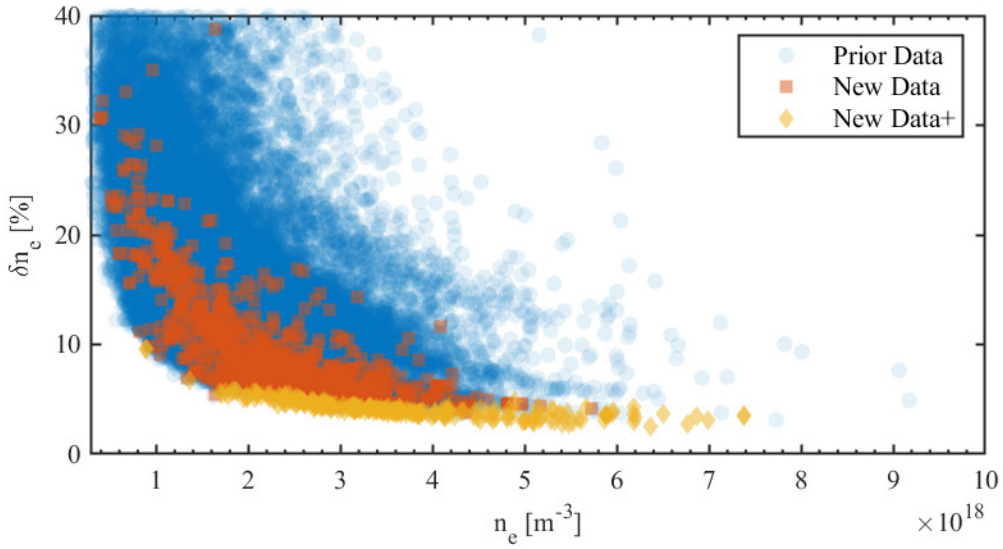

Figure 7.4: Comparison of all three-channel n_e data collected on HSX since 2014. Historical data, 28,609 individual data points, is plotted in blue circles. Data collected after the system upgrade, 1,201 data points, is plotted in orange squares/gold diamonds. Gold diamonds signify measurement uncertainty lower than the pre-upgrade system could achieve.

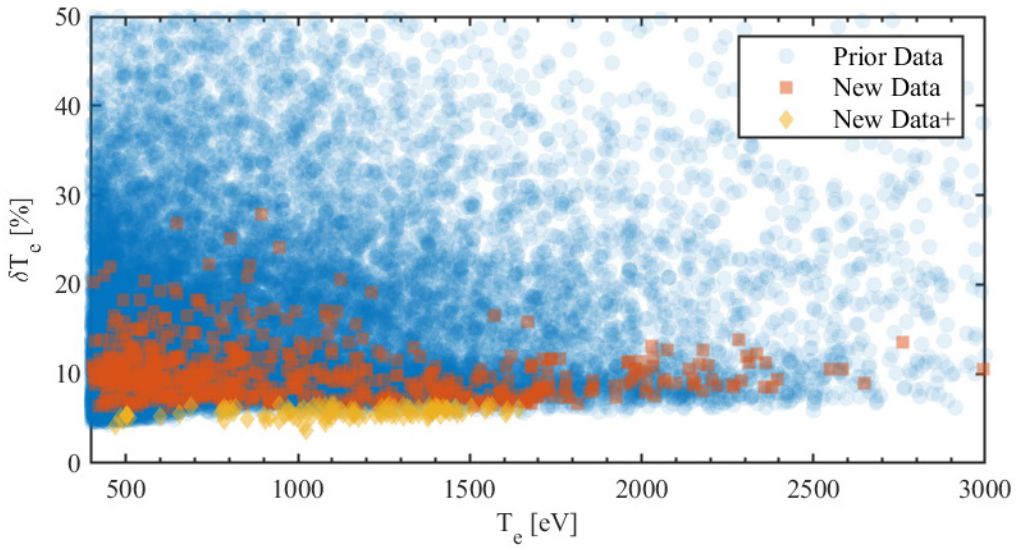

Figure 7.5: Comparison of all five-channel T_e data collected on HSX. Historical data, 38,484 individual data points, is plotted in blue circles. Data collected after the system upgrade, 840 data points, is plotted in orange squares/gold diamonds. Gold diamonds signify measurement uncertainty lower than the pre-upgrade system could achieve.

post-upgrade data has uncertainty lower than that previously achievable on the HSX Thomson scattering diagnostic. Fig. 7.6 plots $\delta N_e(n_e)$ corresponding to the same dataset as that of Fig. 7.5. In Fig. 7.6, the reduction in δn_e is readily apparent by the narrow grouping of the post-upgrade data points on the low end of the region populated by pre-upgrade δn_e. From Fig. 7.6, 20.5% of post-upgrade measurements of n_e on the three-channel polychromators have δn_e lower than previously attainable.

The same analysis of δT_e and δn_e was performed on data from the five-channel polychromators and is presented in Fig. 7.5 and Fig. 7.6, respectively. On the five-channel polychromators, for the measured electron temperature range of 0.4 to 3 keV, δT_e was reduced below previous minimum values for 13.2% of measurements and 3.8% of δn_e are below the pre-upgrade threshold. When comparing the uncer-

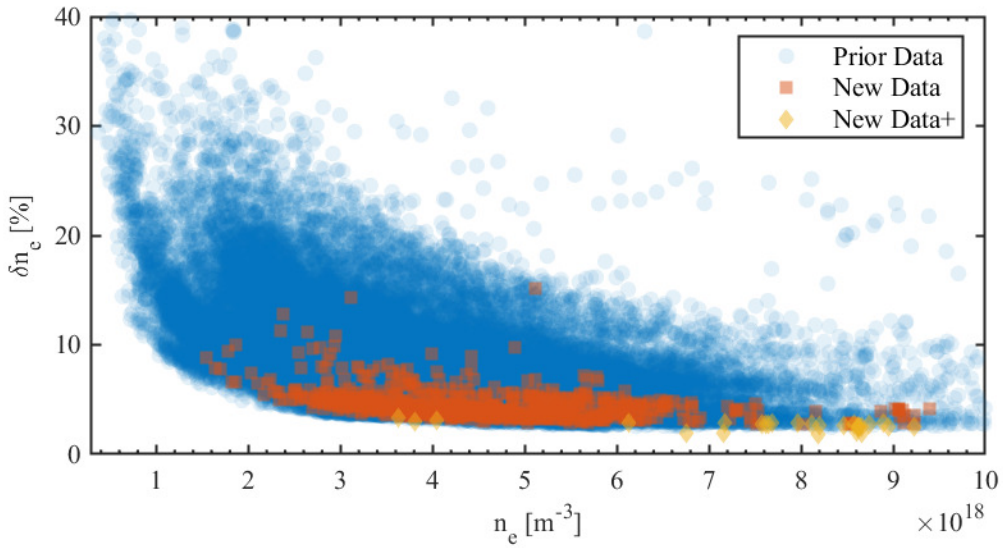

Figure 7.6: Comparison of all five-channel n_e data collected on HSX. Historical data, 38,484 individual data points, is plotted in blue circles. Data collected after the system upgrade, 840 data points, is plotted in orange squares/gold diamonds. Gold diamonds signify measurement uncertainty lower than the pre-upgrade system could achieve.

tainties in Fig. 7.3 and Fig. 7.5, the uncertainty reduction is more significant for the three-channel filter sets than the five-channel filter sets. Generally, the three-channel filter sets measure plasma with n_e less than the five-channel units. Since $N_{j,pe} \propto n_e$ and Poisson statistics state that, at a minimum, $\sigma_j = \sqrt{N_{j,pe}}$, improvements in signal levels will have a greater effect on the uncertainty of three-channel units. A comparison of data from each spatial channel before and after the Thomson scattering diagnostic upgrade is performed in Appendix C.

As discussed in Chapter 4, δT_e is inversely proportional to the plasma electron density, n_e, so measurements carried out in a high-density plasma would have reduced uncertainty when compared to those of a lower-density plasma. It is prudent to rule out the possibility that post-upgrade data has better statistics solely due to being

measured with more optimal plasma parameters, specifically n_e. To evaluate if n_e is biasing the results shown in Fig. 7.3 and Fig. 7.5, the two data sets are binned according to density and compared in Fig. 7.7.

In Fig. 7.7, measurement data for all ten spatial channels was separated into six bins representing a range of densities common to HSX. Starting at $n_e = 1.5{*}10^{18}\ m^{-3}$, each density bin had a width of $1 * 10^{18}\ m^{-3}$, for a maximum density of $n_e = 6.5 * 10^{18}\ m^{-3}$. Each plot in Fig. 7.7 has post-upgrade data with lower uncertainty than previously achievable, especially for the temperature ranges $20\ eV \leq T_e \leq 200\ eV$ and $800\ eV \leq T_e \leq 2\ keV$. Fig. 7.7 shows that when controlling for density, the post-upgrade Thomson scattering system on HSX maintains low uncertainty and narrow error bands throughout the measurement range of T_e compared to data from before the upgrades.

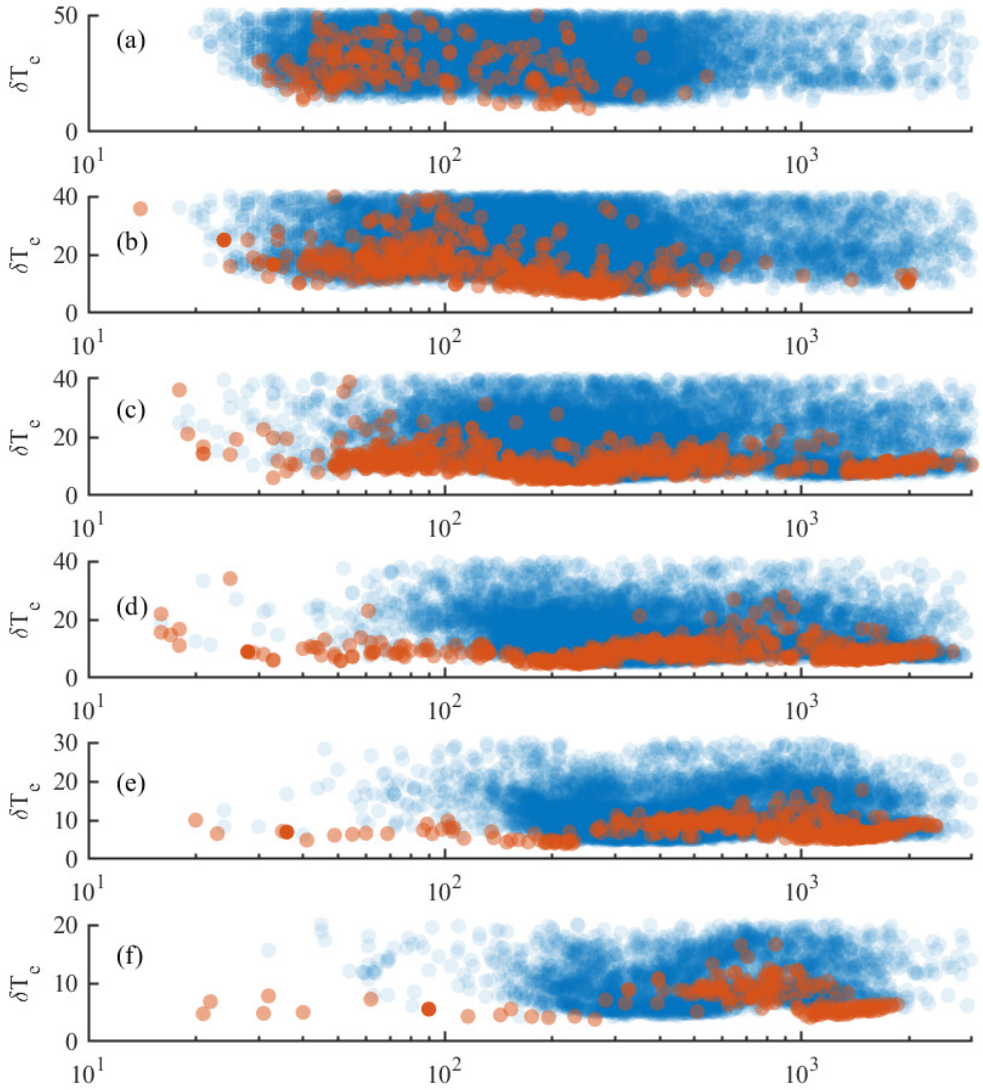

Figure 7.7: Comparison of δ_{T_e} as a function of T_e for pre-upgrade T_e measurements (blue circles) and those collected after the upgrades (orange diamonds). Each row corresponds to a different density level, defined by (a) $0.5 * 10^{18} \leq n_e < 1.5 * 10^{18}$, (b) $1.5{*}10^{18} \leq n_e < 2.5{*}10^{18}$, (c) $2.5{*}10^{18} \leq n_e < 3.5{*}10^{18}$, (d) $3.5{*}10^{18} \leq n_e < 4.5{*}10^{18}$, (e) $4.5 * 10^{18} \leq n_e < 5.5 * 10^{18}$, (f) $5.5 * 10^{18} \leq n_e < 6.5 * 10^{18}$.

7.2 TSSM Filter Set Results

TSSM-optimized filter sets were installed in two spatial channels for standard HSX operation. The first filter set, see Fig. 6.9, was installed at r/a = 0.10, a channel close to the hot plasma core with $T_e > 1\ keV$. For lower temperature measurements, the second filter set, see Fig. 6.10, was installed at r/a = 0.38, where electron temperatures range from 100 eV to 800 eV. In order to evaluate the TSSM method, it is helpful to compare TSSM measurements to data collected by the rest of the HSX Thomson scattering diagnostic. Although the spectral distribution function in Eq. (2.49) is dependent on θ_s and is explicitly different between two adjacent channels, see Fig. B.3 and Fig. B.4 in Appendix B, the error function $\delta T_e(T_e)$ for two adjacent spatial channels is calculated to vary by less than 1%.

Leveraging this fact and the expectation that plasma conditions in HSX are not expected to change drastically for the scale length of a single cm, the new TSSM filter sets can be compared to the existing standard filter sets, given that they are on adjacent channels. Newly designed three-channel TSSM filter sets were installed on HSX Thomson scattering spatial channels two and five, replacing five-channel standard filter sets. In Fig. 7.8, all post-upgrade Thomson scattering data is compared to data measured with the new TSSM filter sets.

In Fig. 7.8, data collected on spatial channel two, the core channel, is the set of yellow diamonds located on the right end of the plot with $T_e > 1\ keV$. When comparing the data from spatial channel two, the uncertainty measured is less than that of similar temperatures measured on adjacent channels. While the TSSM-enabled channel's superior performance to that of its neighboring channels is a promising sign, this result is surprising. Referring to Fig. 6.9 in the previous chapter, the uncertainty in

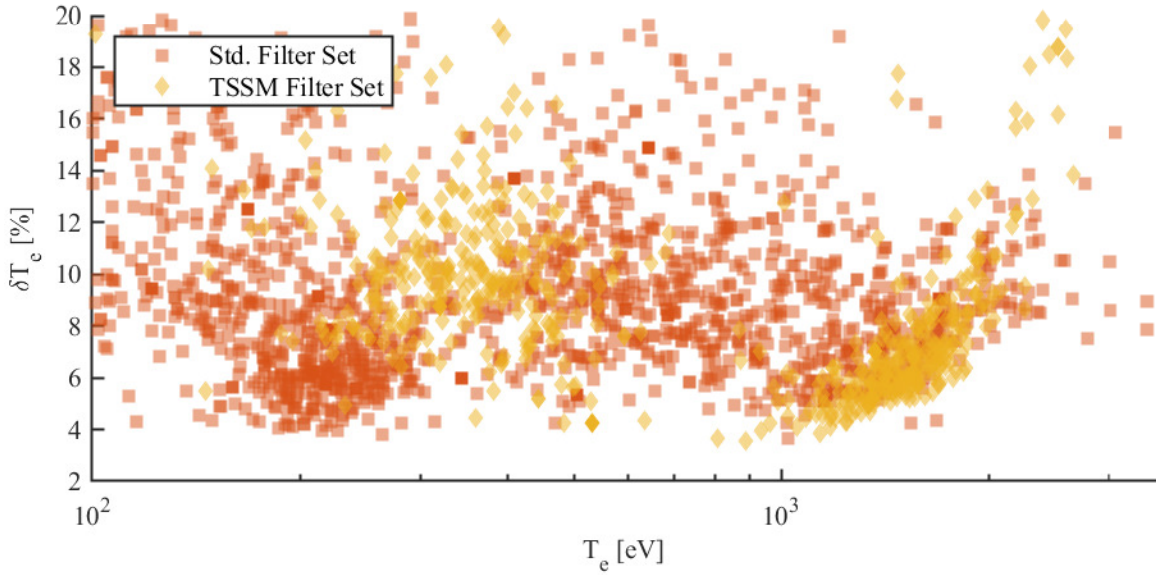

Figure 7.8: Data collected from standard filter sets (orange squares) is compared to data measured by the new TSSM filter sets (yellow diamonds).

the TSSM channel is predicted to be greater than that of the standard five-channel filter set at $T_e > 1\ keV$. This deviation from prediction is most likely because, for a standard filter set at higher temperatures, two of the spectral channels are receiving minimal signal and are therefore contributing a relatively large amount of uncertainty to the χ-squared minimization routine of Eq. (4.5). This deviation from predicted values highlights a significant feature of the TSSM method, wherein all spectral channels receive enough photon bias over the operational range of the diagnostic, which leads to all channels maintaining good photon statistics.

Also denoted by gold diamonds in Fig. 7.8, data from the second TSSM-enabled spatial channel ranges from 200 eV to 600 eV. Unlike the results from spatial channel two, the results from this spatial channel are unexpected as they have significantly increased δT_e compared to the calculated values in Fig. 6.10. The increased error at lower values of T_e on spatial channel five stems from the method of filtering used to

remove the fundamental 1064 nm light discussed in Section 6.6. While the TSSM filter set on spatial channel one uses a notch filter with OD 6 blocking at 1064 nm, spatial channel five is only equipped with a short-pass filter with OD 4 blocking at 1064 nm. Even with OD 4 blocking, some fundamental 1064 nm light can pass through the short-pass filter and interfere with spectral channel one, negatively affecting the ability of χ-squared minimization routine of Eq. (4.5) to resolve T_e accurately.

Although the uncertainty of spatial channel five is higher than predicted, it is still comparable to that of the standard, five-channel HSX filter sets. Taking a qualitative look at the data of fig. 7.8, implementation of the TSSM filter sets has been successful, as the two TSSM-enabled filter sets that only require three spectral channels are performing as well as, if not better than, the existing standard five-channel filter sets in use on HSX.

Chapter 8

Conclusion

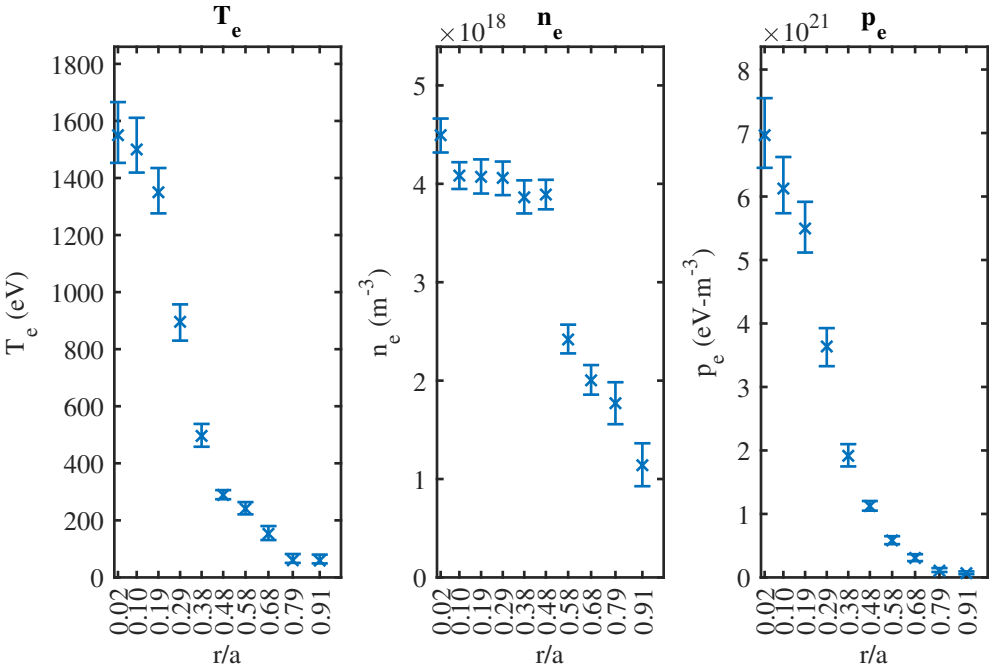

Figure 8.1: Thomson scattering measurements in He plasma. Data was collected during shot 44 on 2024-03-29. (Left) Electron temperature profile. (Middle) Electron density profile. (Right) Electron pressure profile.

8.1 Summary of Key Results

Thomson scattering is a critical diagnostic on HSX used for measuring T_e and n_e with high spatial and temporal resolution. Data from the Thomson scattering diagnostic on HSX is also vital as an input for many of the other diagnostics and computational tools used on HSX. Previously, upwards of ten Thomson scattering measurements would have to be statistically averaged before the data was statistically valuable as input for additional analysis routines or simulations. Referring to the results presented in Chapter 7, it has been shown that the net impact of the Thomson upgrades discussed in Chapter 5 and the implementation of the novel TSSM filtering technique, Chapter 6, is a Thomson scattering diagnostic with significantly increased performance. Measurement uncertainty of the HSX Thomson scattering diagnostic has been reduced to a point where each HSX Thomson scattering measurement will have enough statistical power to be used as an input for simulation and analysis routines.

New Optical Setup

In Section 5.4, modifications to the optical setup were discussed. The output energy of the existing Nd:YAG laser increased total output energy to 767 mJ, just over 90% of the manufacturer-specified value and significantly higher than it has been for at least a decade. By optimizing the physical laser launch position to minimize optical element interactions, the overall beam path was reduced from 10.5 m to 8.5 m, and the number of required dielectric mirrors was reduced from five to just one. Removing the baffled beam tubes eliminated energy loss from interactions with the baffles and significantly decreased vessel transit energy loss from 30% to just 3%. A second

benefit realized by removing the beam tubes was focusing optics with a shorter focal length could be used, increasing the fraction of the beam imaged by the collection optics to increase by 63%. The result of the new optical setup was the increase of collected power per scattering event by 168%, significantly improving the system S/N.

New Preamplifier Electronics

The design, build, and test of ultra-fast, low-noise polychromator preamplifier electronics is presented in Section 5.2. Test results show that the new preamplifier electronics have a maximum gain of 79.5 $dB\Omega$ at 61.5 MHz and RMS noise of only 5 mV_{pk-pk}. Following the upgraded preamplifier electronics installation, HSX now has the highest bandwidth detection electronics on any noncollective Thomson scattering system.

New High-speed Digitizer

A CAEN S.p.A. VX1743 digitizer capable of digitizing signals at a blazing fast 3.2 GSa/s has been commissioned on the HSX Thomson scattering diagnostic. As discussed in Section 5.1, using a sampling digitizer over a charge-integrating digitizer gives the experimentalist significantly more flexibility in signal analysis. With the ultra-fast preamplifiers now on HSX, the VX1743 will ensure no signal pulses are missed due to gate timing errors. Time-resolved digitization of scattered signals allows for pulse fitting routines that reduce uncertainty by mitigating noise contributions in the digitized signal.

New Calibration Routine

A new spectral calibration routine has been implemented on HSX. It has been shown that using a separate calibration fiber that is not the same core sie or NA for spectral calibration, significant errors are introduced into the calibration. Instead of using a separate calibration fiber during the spectral calibration process, the operational Thomson scattering collection fibers are now used. Comparisons of Raman scattered data, which are very sensitive to spectral calibrations, have shown that the new spectral calibration method results in calibration factors that are physically possible. This new spectral calibration method reduces uncertainty related to the calibration and is less likely to over- or under-estimate the signal level on a given spectral channel.

New Filter setup (TSSM)

As shown in Section 7.2, an optimized TSSM filter set has been installed and successfully tested on the HSX Thomson scattering diagnostic. It has been successfully shown that the three-channel TSSM filter set provides accurate measurements for a range of T_e wider than achievable with a standard HSX three-channel filter set. Not only has the TSSM method proven to extend the measurement range of a spatial channel with only three available spectral channels, but the TSSM method has also shown superior performance when compared to a standard five-channel filter set. The TSSM spectral filtering method has been proven to be a practical approach and can potentially improve Thomson scattering measurements for the entire fusion community.

8.2 Future Work

Polychromator Redesign

Constraints related to the existing polychromator enclosures primarily limited the design and implementation of the modifications described in this work. Specifically, the form factor of the polychromator enclosure is bulky, and its design restricts access to individual polychromator channels for maintenance and calibration. Recalling the polychromator schematic in Fig. 3.2, the APD and electronics are housed in a separate enclosure that mounts to the detector mount, with multiple channels of electronics enclosures stacked vertically. When testing or calibration requires access to the polychromator electronics, one must remove the entire electronics housing, voiding the existing spectral calibrations. Another issue with the stacked polychromator electronics is that the current state of the design requires the electronics of each spectral channel to have an isolated reference. When the polychromator enclosure has a stack of spectral channels with isolated references, there is moderate capacitive coupling to the primary polychromator reference, leading to noise and cross-talk issues. Finally, the lack of an active temperature stabilization scheme for the APDs is the most significant issue with the current polychromator enclosure. APD gain and responsivity strongly depend on the device's temperature. The method currently used to stabilize APD temperatures runs cooling water through the body of the polychromator enclosure, which ideally convectively cools the APDs.

The design of an optimized, high-speed Thomson scattering polychromator could further reduce the measurement uncertainty of a spatial channel. Consolidating the disparate polychromator channels into a single, accessible package will reduce system

cross-talk and minimize noise sensitivity. Implementing an active cooling circuit like a TEC would improve Thomson scattering calibration data's reliability and eliminate uncertainty resulting from operational temperature fluctuations.

Time Resolved Thomson Measurements

The upgraded electronics and high-speed digitization capabilities of the HSX Thomson scattering diagnostic allow for a high repetition rate of data collection, up to 70 scattering events at a repetition rate of 80 kHz. A 20 pulse, 900 mJ, 1064 nm, 400 Hz laser with a 2 kHz burst mode has recently been purchased to replace the existing 10 Hz laser. Thomson scattering conducted with this high repetition rate laser will enable the measurements of the temporal evolution of T_e and n_e profiles. This new measurement capability enables direct study of plasma evolution when subjected to perturbative excitations, like those in gas puff density modulation or ECRH power modulation.

Targeted TSSM

It has been shown that using three dual-passband spectral filters can improve the performance of a Thomson scattering diagnostic. Recent calculations have also shown that converting one Thomson scattering spectral channel from a single pass-band to a TSSM-enabled channel can improve system performance with minimal required changes. For experiments with a fully functional Thomson scattering system, a more targeted approach of modifying a single spectral channel will be an inexpensive way to improve the overall diagnostic.

Appendix A

Custom TSSM Filter Data

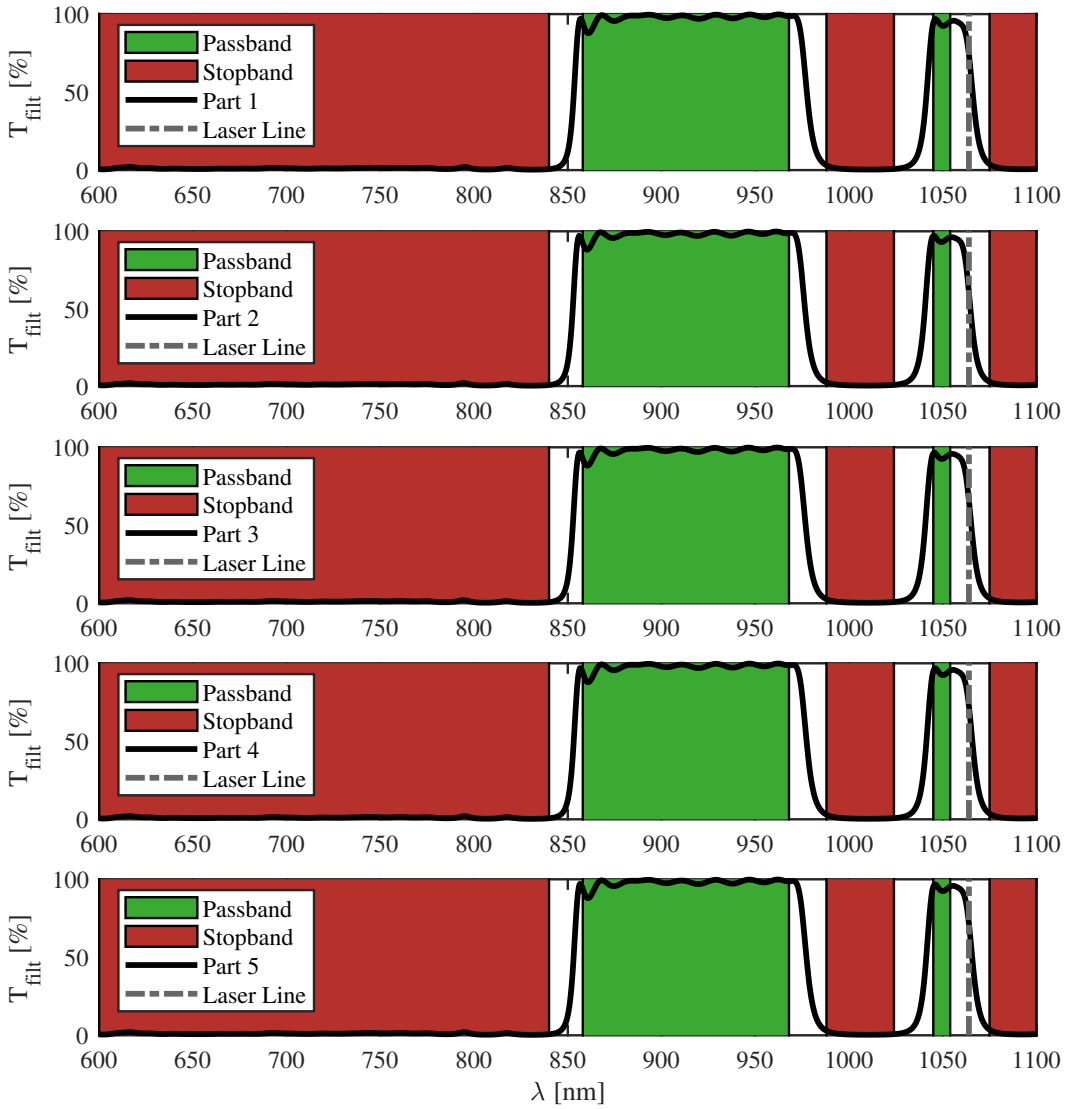

Figure A.1: As built spectral characteristics of Alluxa filter 1, parts 1-5. The color areas of the plot represent the specified transmission characteristics and reflection bands.

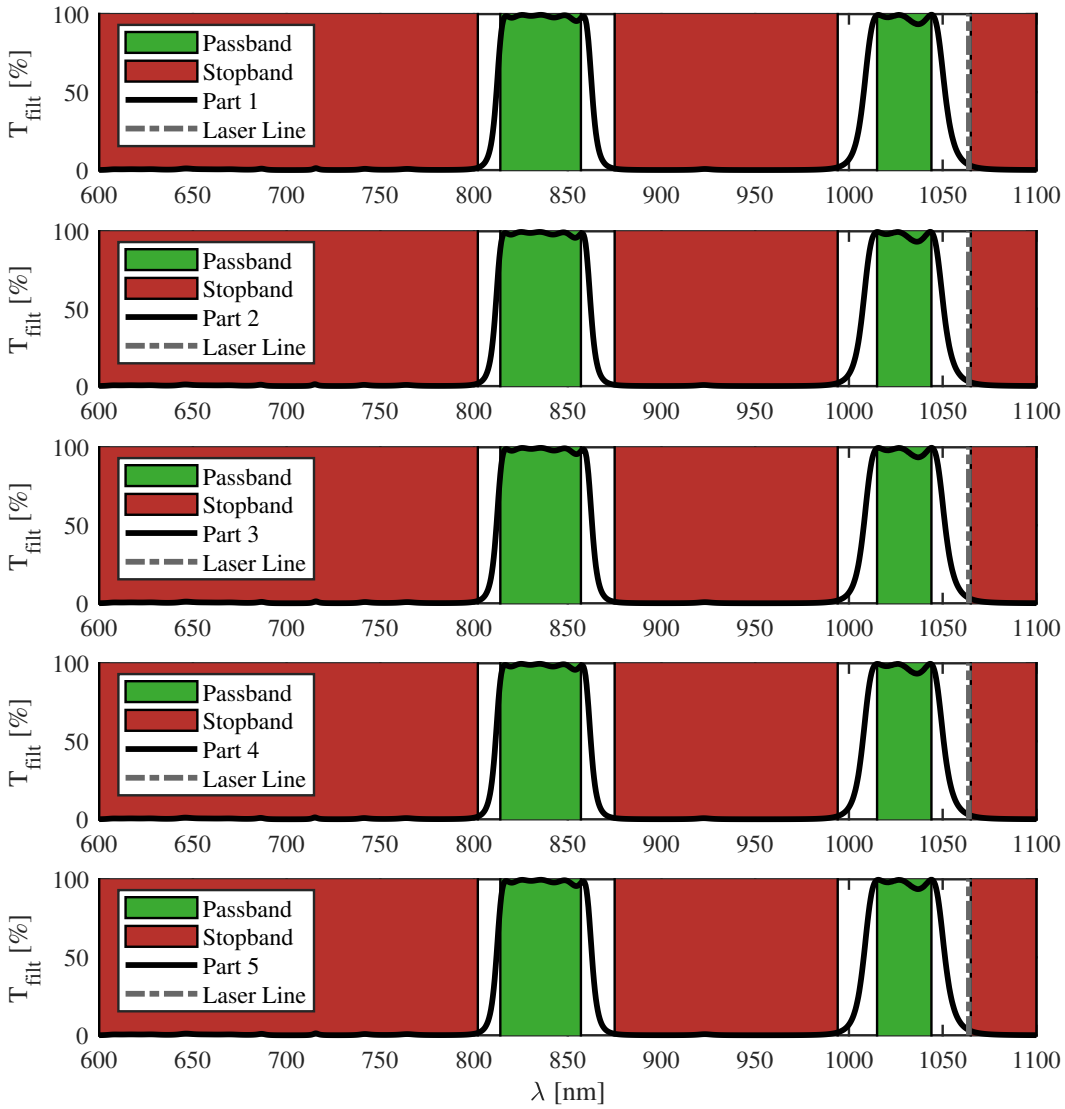

Figure A.2: As built spectral characteristics of Alluxa filter 2, parts 1-5. The color areas of the plot represent the specified transmission characteristics and reflection bands.

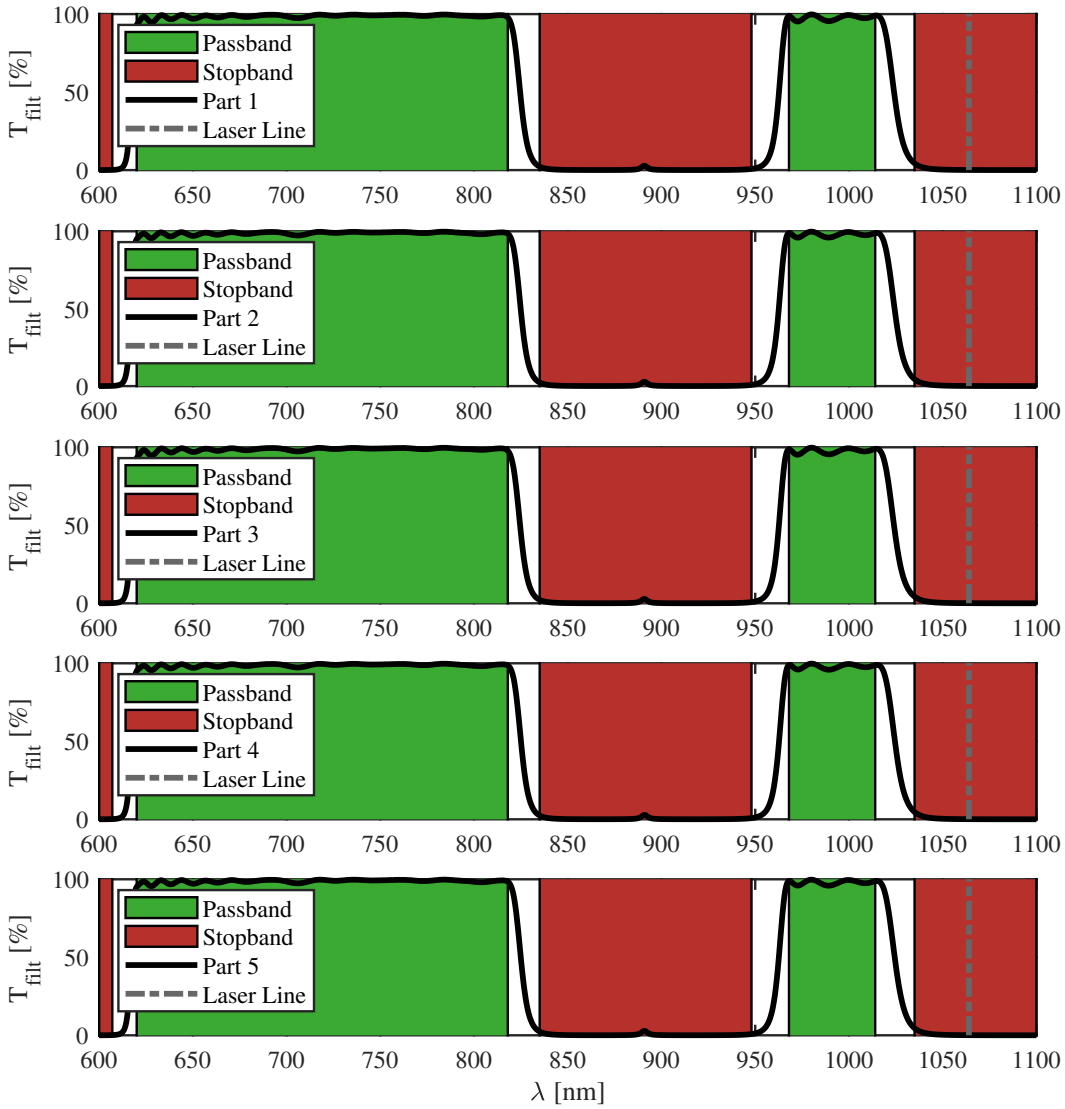

Figure A.3: As built spectral characteristics of Alluxa filter 3, parts 1-5. The color areas of the plot represent the specified transmission characteristics and reflection bands.

Appendix B

Upgraded HSX Filter Set Data

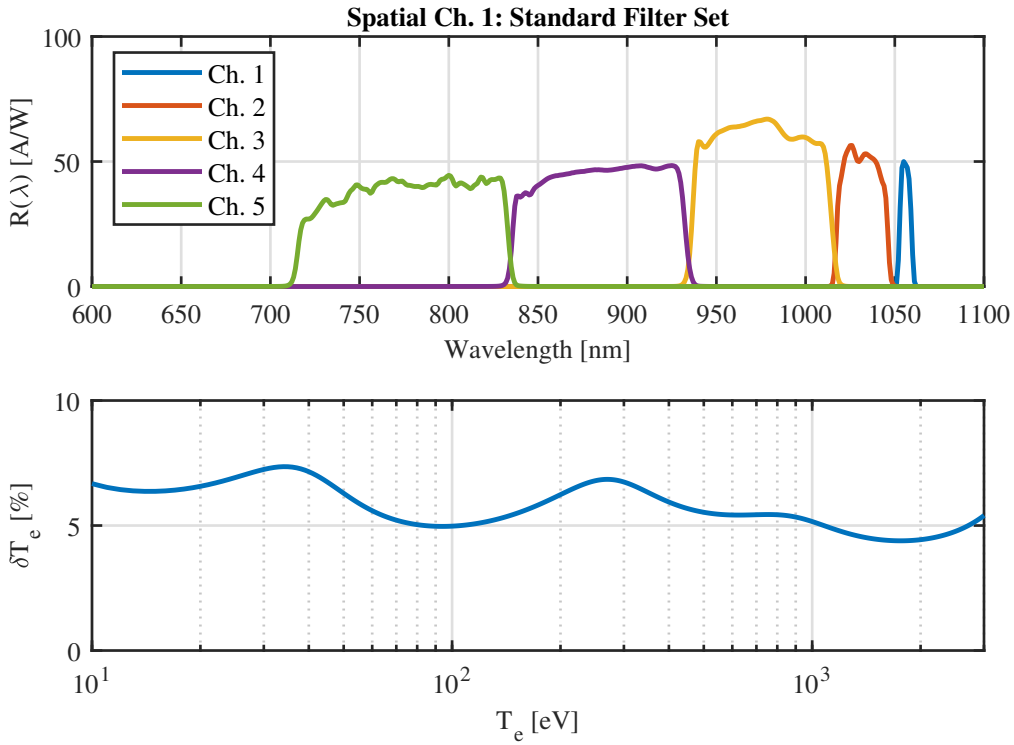

Figure B.1: Measured responsivity of Spatial Ch. 1 (top) and the expected relative error, δ_{T_e}, for the HSX Thomson scattering diagnostic. A plasma density, n_e, of $3 * 10^{18}\ m^{-3}$ was used for this estimation. Spatial channel one is currently equipped with the standard HSX five channel filter set.

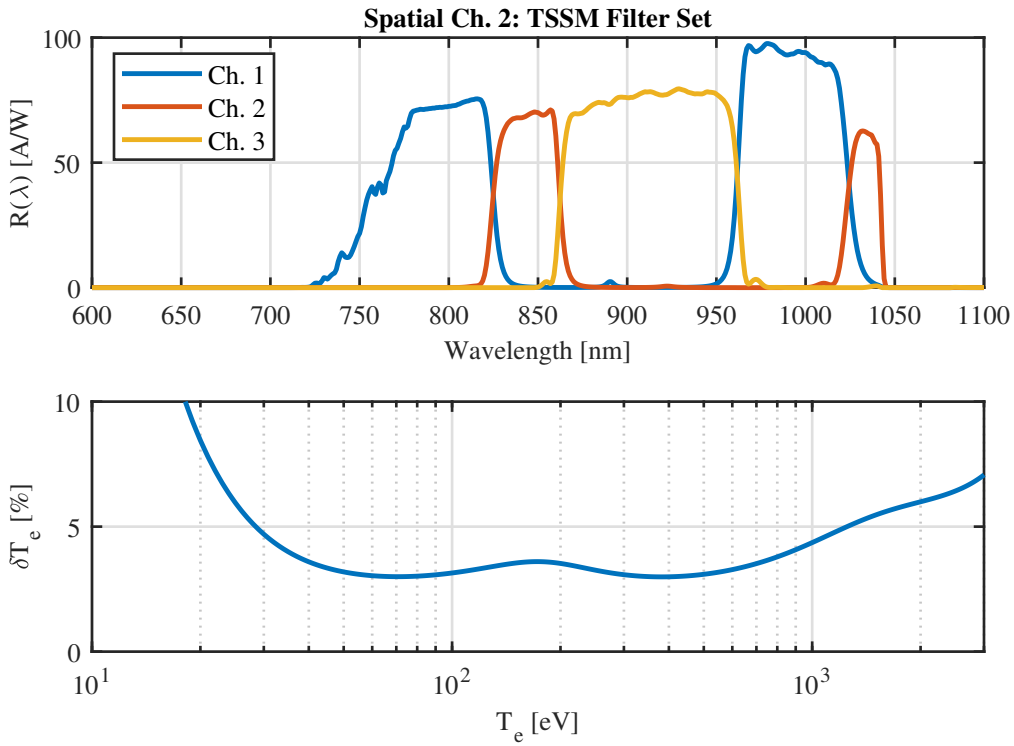

Figure B.2: Measured responsivity of Spatial Ch. 2 (top) and the expected relative error, δ_{T_e}, for the HSX Thomson scattering diagnostic. A plasma density, n_e, of $3 * 10^{18}\ m^{-3}$ was used for this estimation. Spatial channel two is currently equipped with the newly developed TSSM three channel filter set.

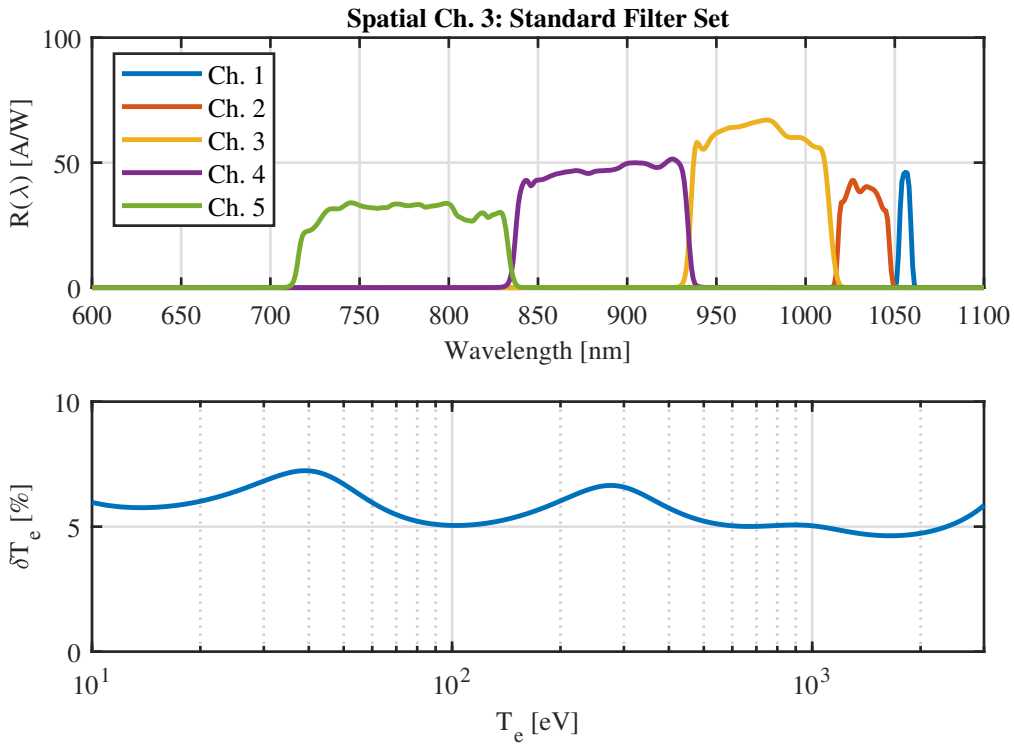

Figure B.3: Measured responsivity of Spatial Ch. 3 (top) and the expected relative error, δ_{T_e}, for the HSX Thomson scattering diagnostic. A plasma density, n_e, of $3 * 10^{18}\ m^{-3}$ was used for this estimation. Spatial channel three is currently equipped with the standard HSX five channel filter set.

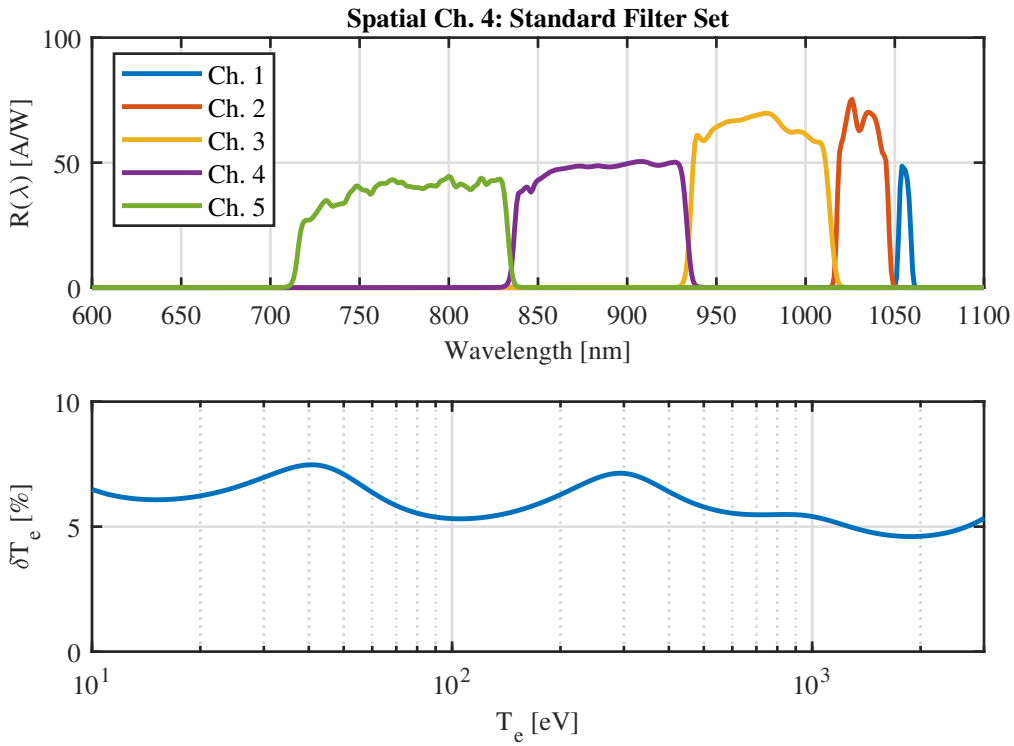

Figure B.4: Measured responsivity of Spatial Ch. 4 (top) and the expected relative error, δ_{T_e}, for the HSX Thomson scattering diagnostic. A plasma density, n_e, of $3 * 10^{18}\ m^{-3}$ was used for this estimation. Spatial channel four is currently equipped with the standard HSX five channel filter set.

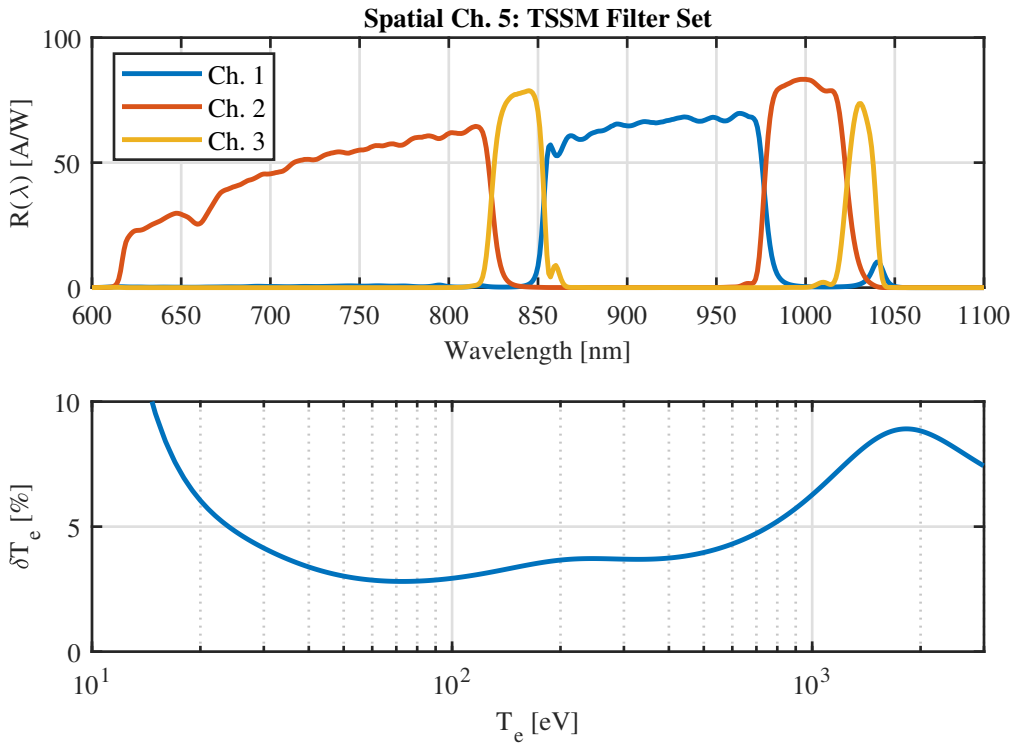

Figure B.5: Measured responsivity of Spatial Ch. 5 (top) and the expected relative error, δ_{T_e}, for the HSX Thomson scattering diagnostic. A plasma density, n_e, of $3 * 10^{18}\ m^{-3}$ was used for this estimation. Spatial channel five is currently equipped with the newly developed TSSM three channel filter set.

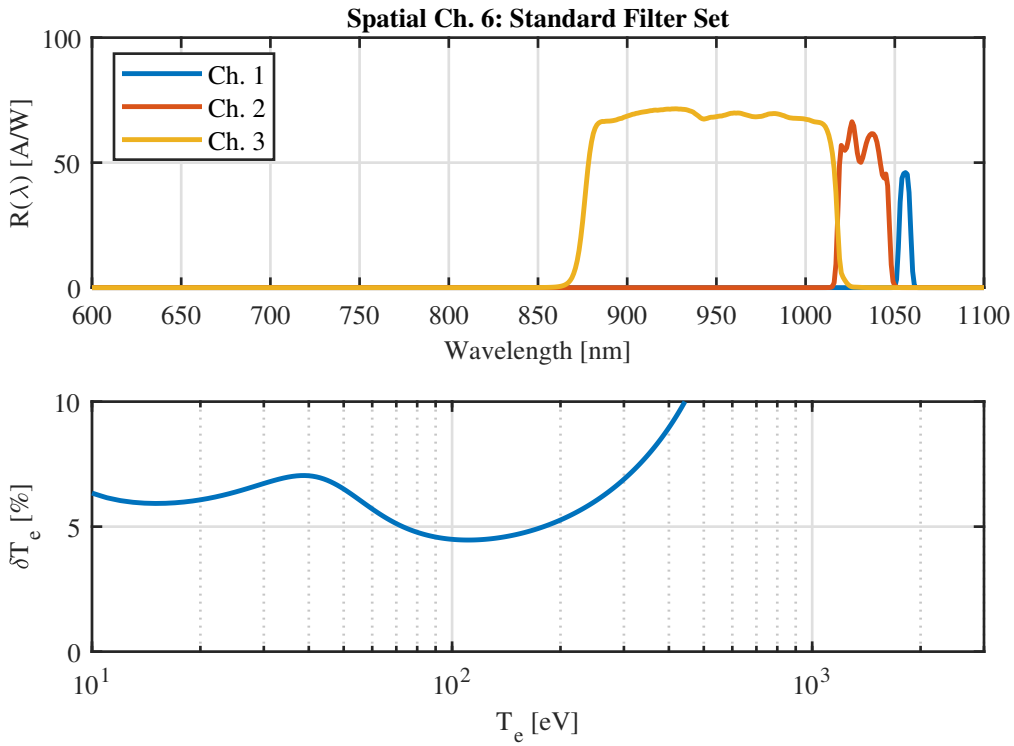

Figure B.6: Measured responsivity of Spatial Ch. 6 (top) and the expected relative error, δ_{T_e}, for the HSX Thomson scattering diagnostic. A plasma density, n_e, of $3 * 10^{18}\ m^{-3}$ was used for this estimation. Spatial channel six is currently equipped with the standard HSX three channel filter set.

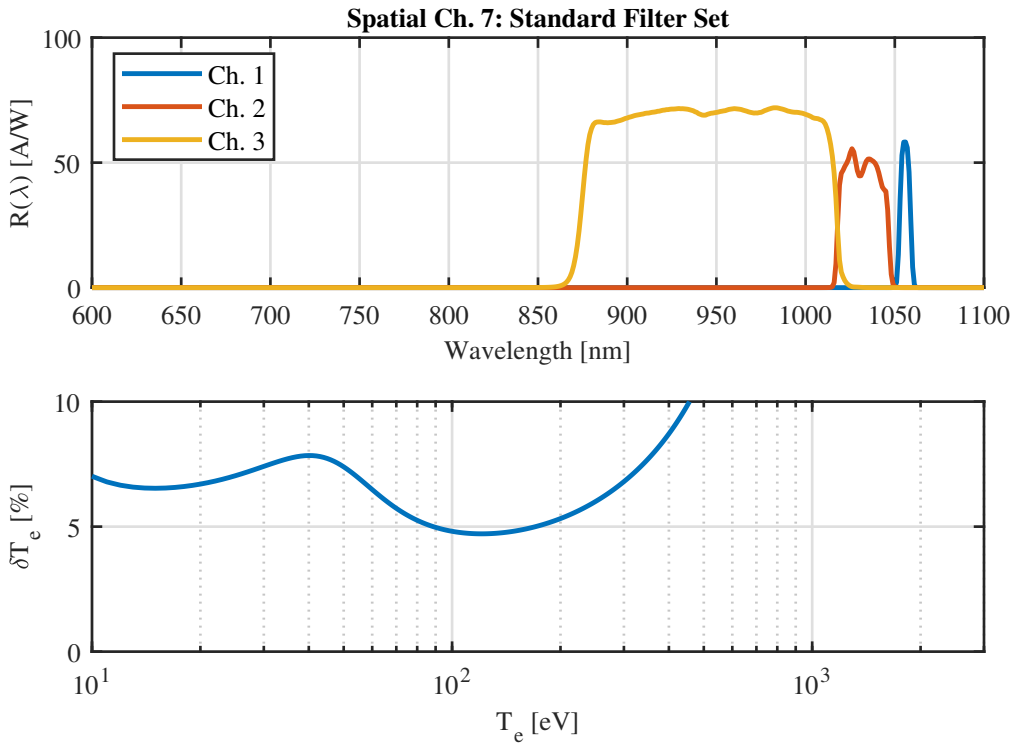

Figure B.7: Measured responsivity of Spatial Ch. 7 (top) and the expected relative error, δ_{T_e}, for the HSX Thomson scattering diagnostic. A plasma density, n_e, of $3 * 10^{18}\ m^{-3}$ was used for this estimation. Spatial channel seven is currently equipped with the standard HSX three channel filter set.

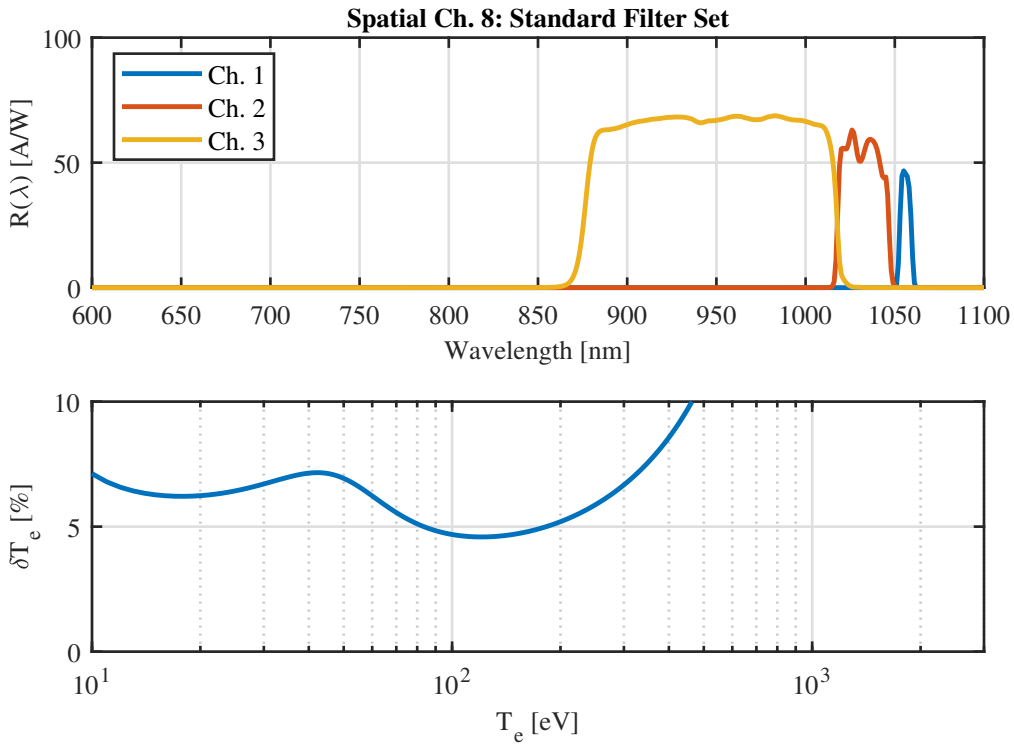

Figure B.8: Measured responsivity of Spatial Ch. 8 (top) and the expected relative error, δ_{T_e}, for the HSX Thomson scattering diagnostic. A plasma density, n_e, of $3 * 10^{18}\ m^{-3}$ was used for this estimation. Spatial channel eight is currently equipped with the standard HSX three channel filter set.

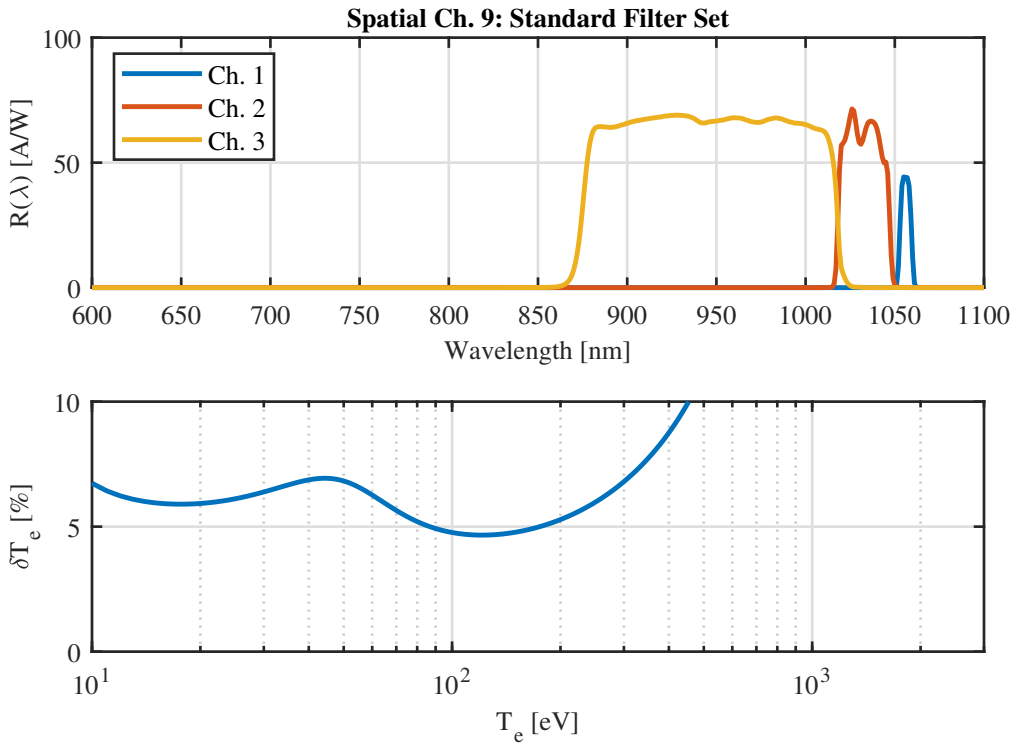

Figure B.9: Measured responsivity of Spatial Ch. 9 (top) and the expected relative error, δ_{T_e}, for the HSX Thomson scattering diagnostic. A plasma density, n_e, of $3 * 10^{18}\ m^{-3}$ was used for this estimation. Spatial channel nine is currently equipped with the standard HSX three channel filter set.

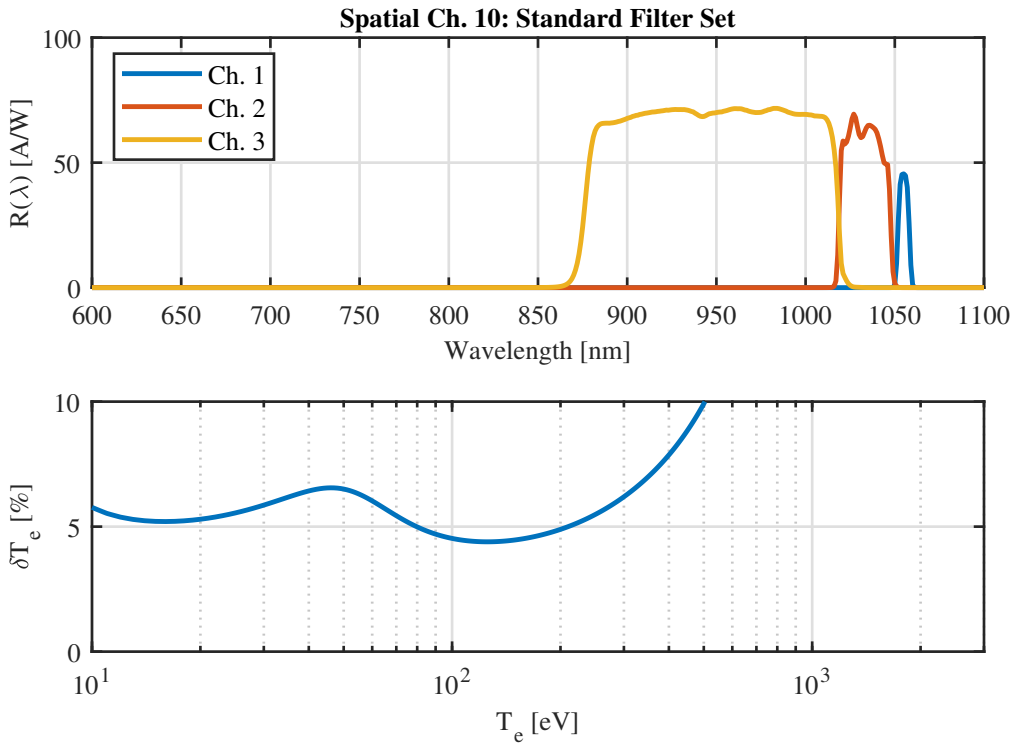

Figure B.10: Measured responsivity of Spatial Ch. 10 (top) and the expected relative error, δ_{T_e}, for the HSX Thomson scattering diagnostic. A plasma density, n_e, of $3 * 10^{18}\ m^{-3}$ was used for this estimation. Spatial channel ten is currently equipped with the standard HSX three channel filter set.

Appendix C

Pre-Upgrade Error vs. Post-Upgrade Error

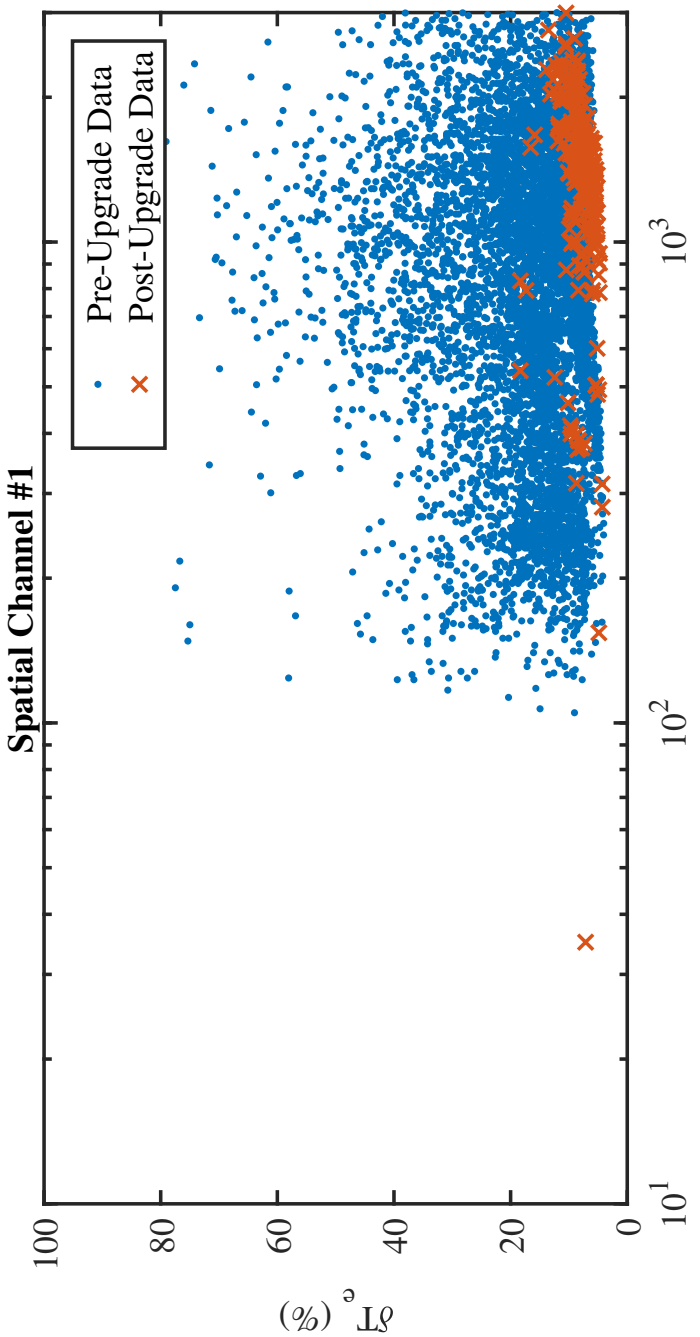

Figure C.1: Comparison of historical HSX data, 7,715 data points, to data collected on HSX after the Thomson upgrade, 281 data points, for all densities on Spatial Channel 1, with the standard five channel filter set.

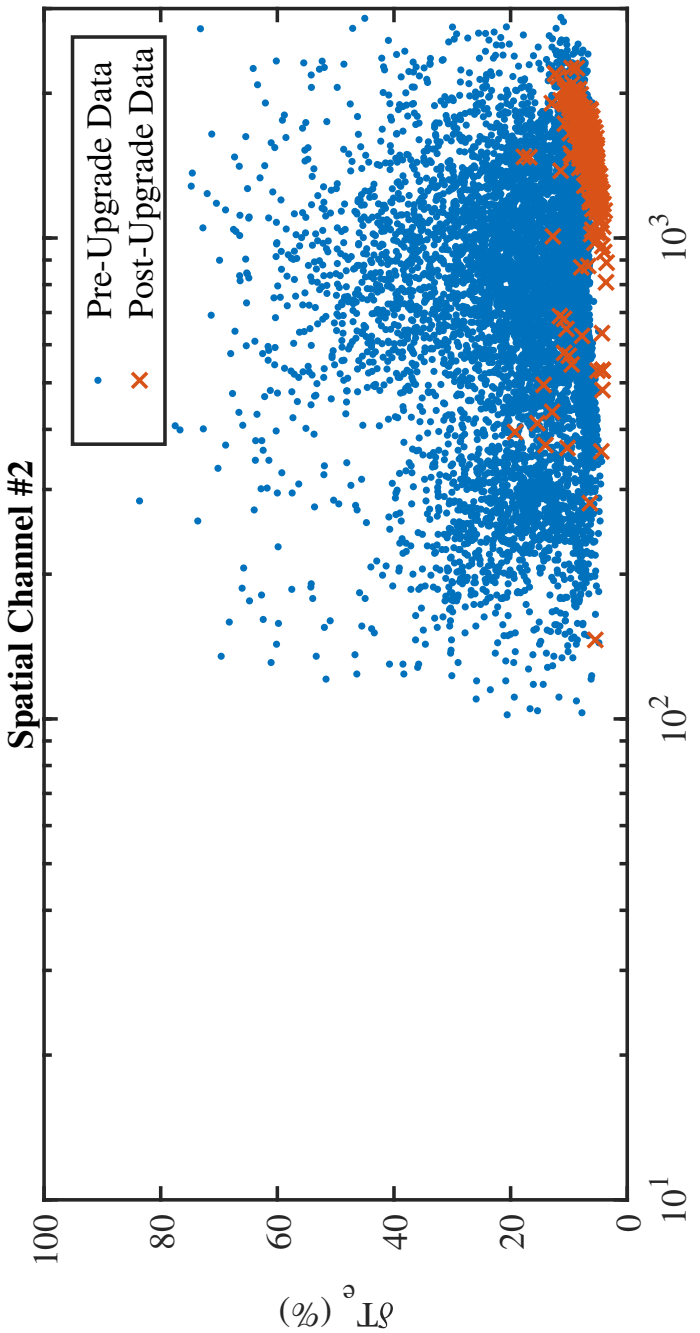

Figure C.2: Comparison of historical HSX data, 7,715 data points, to data collected on HSX after the Thomson upgrade, 280 data points, for all densities on Spatial Channel 2, with the TSSM three channel filter set.

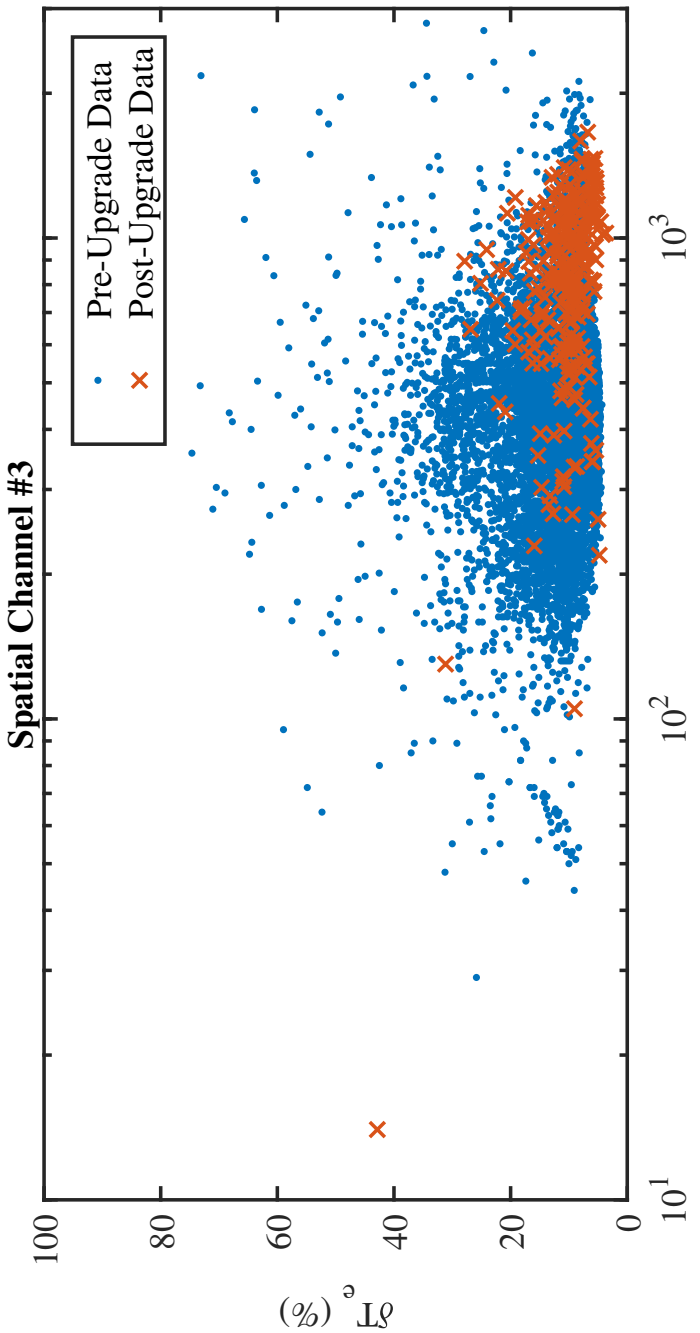

Figure C.3: Comparison of historical HSX data, 7,778 data points, to data collected on HSX after the Thomson upgrade, 281 data points, for all densities on Spatial Channel 3, with the standard five channel filter set.

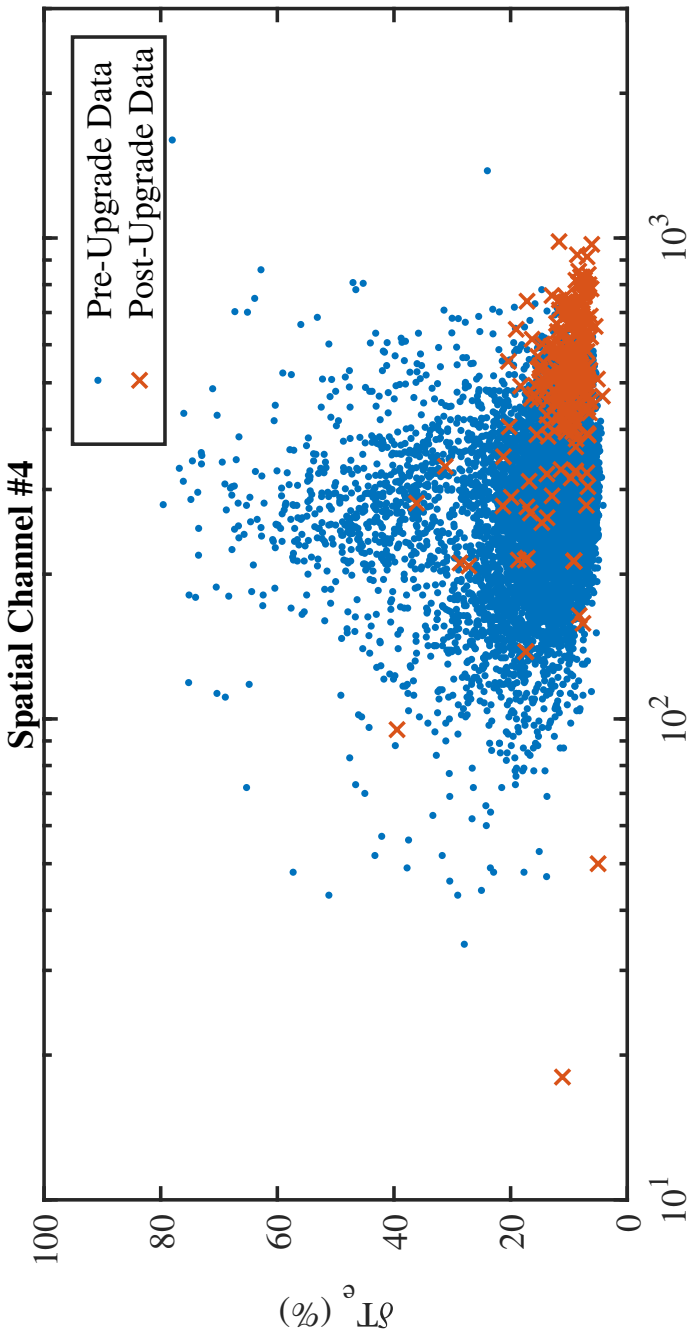

Figure C.4: Comparison of historical HSX data, 7,640 data points, to data collected on HSX after the Thomson upgrade, 281 data points, for all densities on Spatial Channel 4, with the standard five channel filter set.

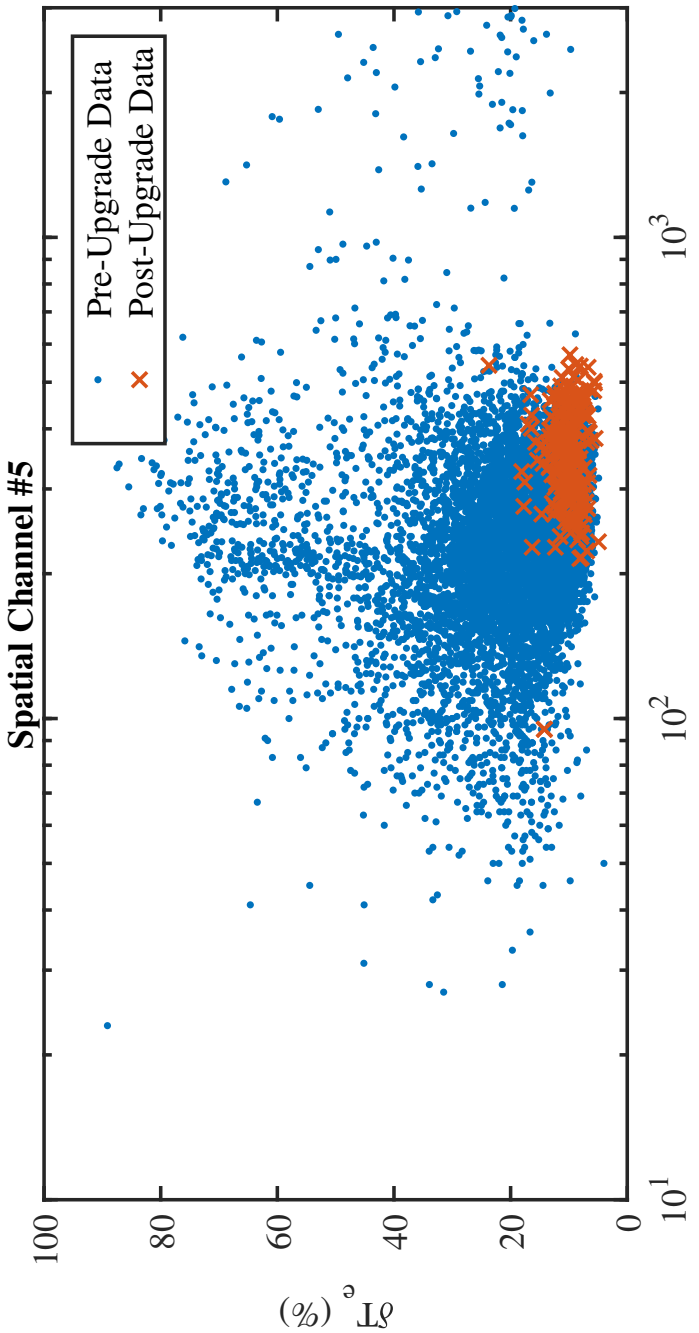

Figure C.5: Comparison of historical HSX data, 7,512 data points, to data collected on HSX after the Thomson upgrade, 215 data points, for all densities on Spatial Channel 5, with the TSSM three channel filter set.

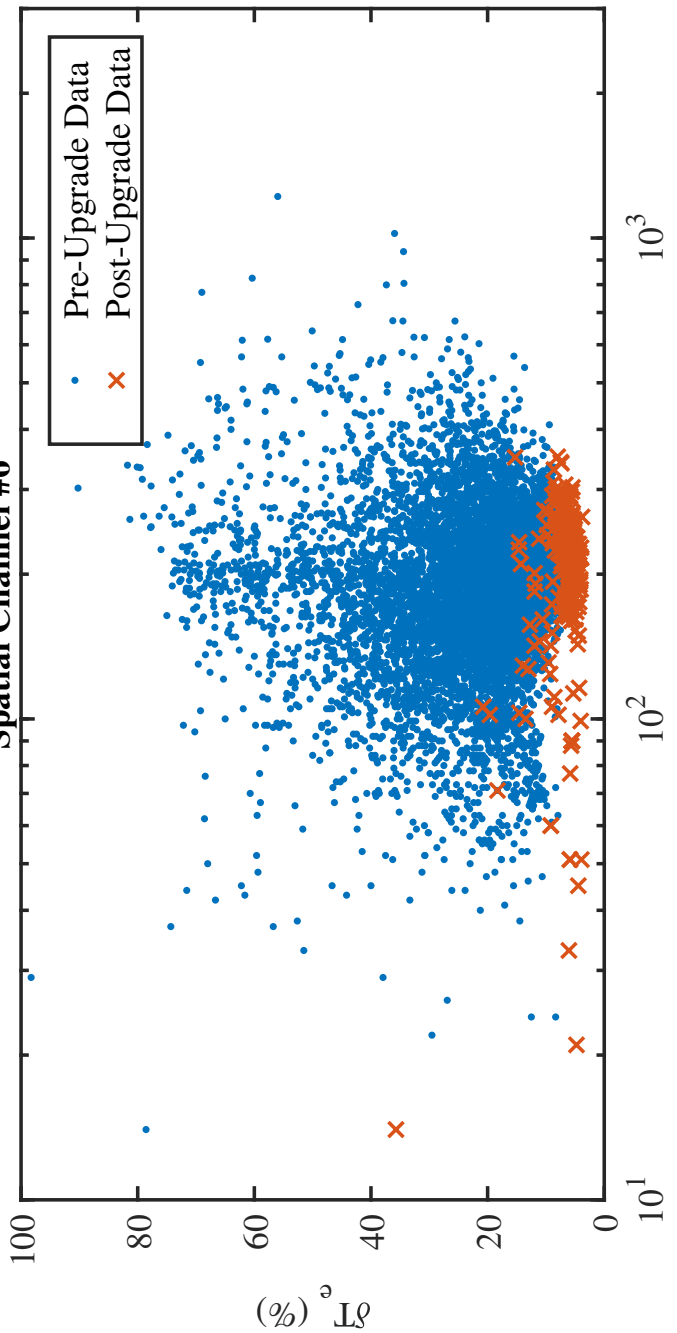

Figure C.6: Comparison of historical HSX data, 7,441 data points, to data collected on HSX after the Thomson upgrade, 277 data points, for all densities on Spatial Channel 6, with the standard three channel filter set.

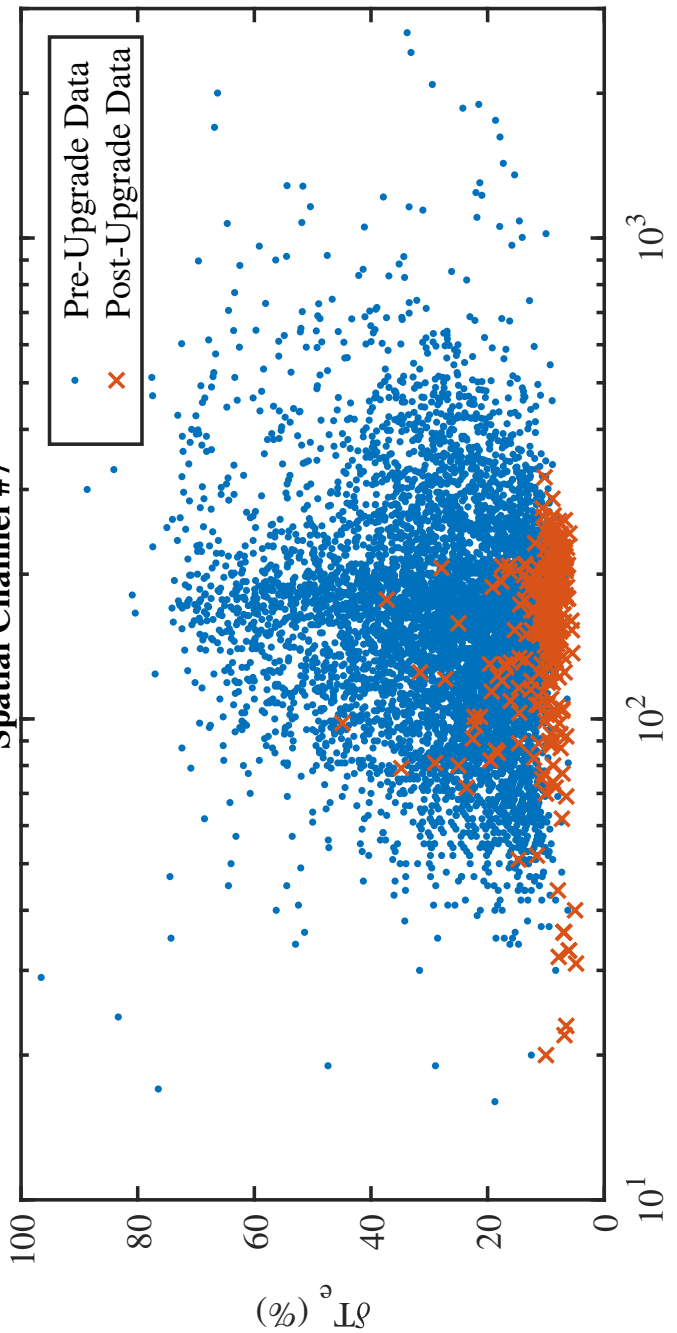

Figure C.7: Comparison of historical HSX data, 7,328 data points, to data collected on HSX after the Thomson upgrade, 276 data points, for all densities on Spatial Channel 7, with the standard three channel filter set.

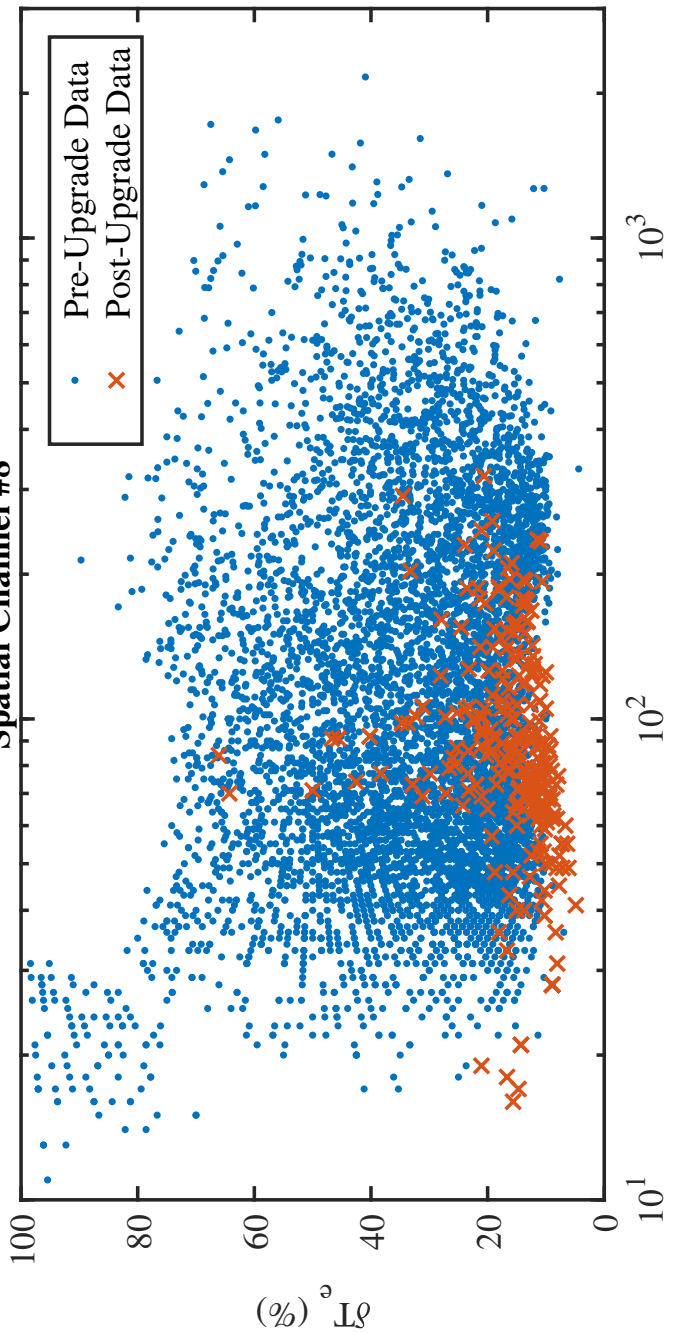

Figure C.8: Comparison of historical HSX data, 6,666 data points, to data collected on HSX after the Thomson upgrade, 265 data points, for all densities on Spatial Channel 8, with the standard three channel filter set.

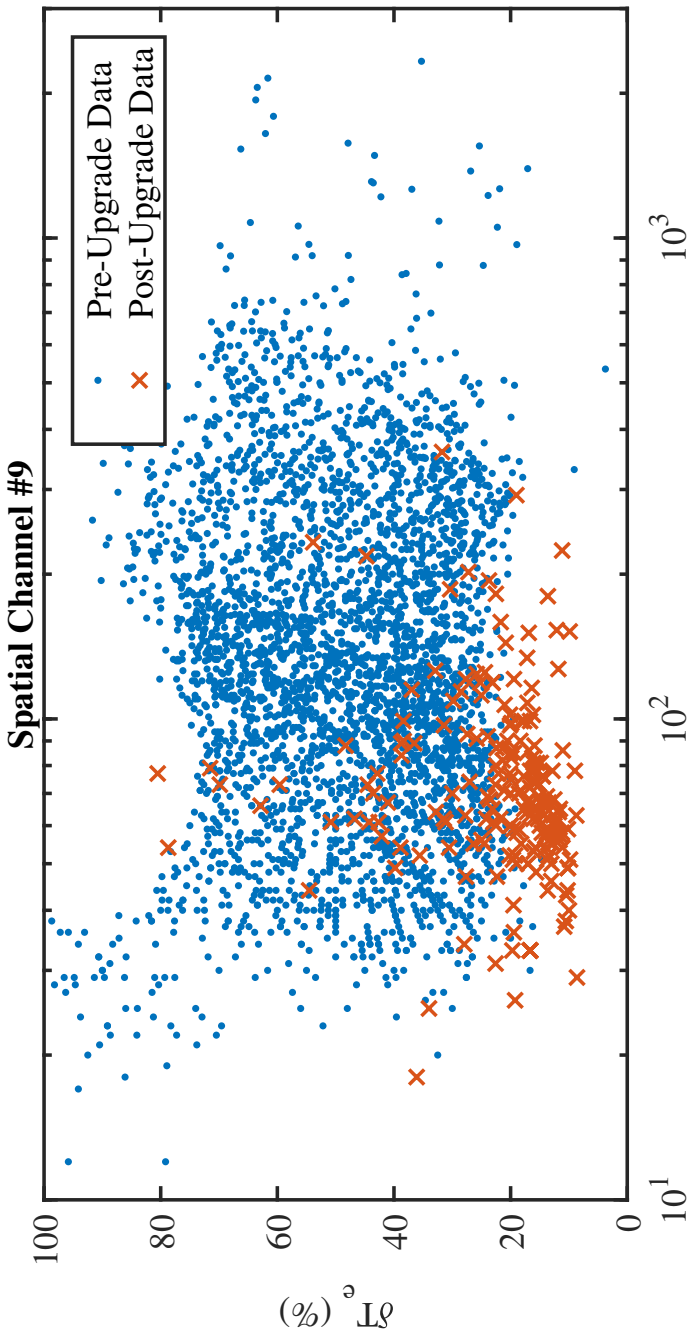

Figure C.9: Comparison of historical HSX data, 3,534 data points, to data collected on HSX after the Thomson upgrade, 223 data points, for all densities on Spatial Channel 9, with the standard three channel filter set.

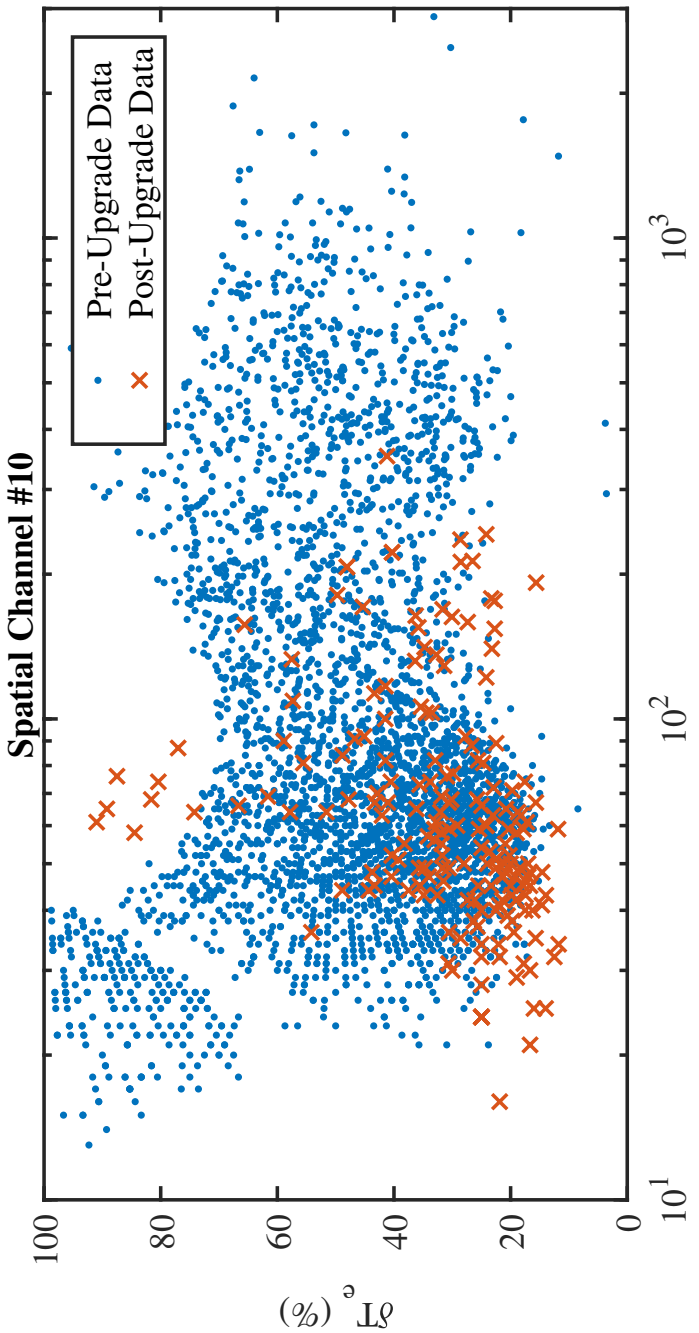

Figure C.10: Comparison of historical HSX data, 3,640 data points, to data collected on HSX after the Thomson upgrade, 211 data points, for all densities on Spatial Channel 10, with the standard three channel filter set.